Antal Kerpely Doctoral School of Materials Science and Technology

Name of the Head of the Doctoral School: Prof. Valeria Mertinger, DSc

Degradation and Rebuilding of Friction Stir Welding Tools

PhD dissertation

PhD candidate

Nour El Imane DissertationDjimaoui , MSc

Supervisors

Prof. Valeria Mertinger, DSc

Prof Yoni Adonyi, PhD

Institute of Physical Metallurgy, Metal-forming and Nanotechnology

University of Miskolc, Miskolc, Hungary

2026

Supervisors Recommendation

I am writing in support of Nour El Imane Djimaoui, PhD Candidate, University of Miskolc (UMI).

I have been her PhD co-advisor since 2022, when she came to Hungary from her native Algiers. She impressed me from the very beginning as an astute and very intelligent student, even though she had limited experience with my area of expertise (welding engineering). Imane started her work on a totally new area for her – Friction Stir Welding – driven by a genuine scientific curiosity and her confidence in what she knew best: metallurgical engineering.

Imane is a fast learner and became familiar with advanced analytical materials characterisation systems at UMI in a very short time. With her good control of the English language and kind demeanour, she quickly won the respect of her student colleagues and professors. Her thorough studying and researching attitudes revealed also her excellent reasoning skills, which brought quick results. Therefore, she was able to publish a few good papers in the first few years of graduate studies.

Because her PhD topic required international cooperation (TWI in Cambridge, the UK), she handled joint research very well, despite early difficulties related to personnel changes on the UK side of the research. Her excellent communication skills were later confirmed by writing a joint paper with two former students at University West, Sweden.

Finally, what sticks to my mind among other graduate students I've advised before is her persuasion and resourcefulness when difficulties arose in her research. She pulled out an excellent dissertation from scarce number of samples or lack of reliable information. Unique to her approach was forensic metallographic analysis of tool wear from the perspective of the friction stir tool itself.

In conclusion, I would fully support her candidacy and think she perfectly deserved a PhD from UMI.

Yoni Adonyi, PhD

Fully agreeing with Professor Adonyi's words, I would add a few additional thoughts to the recommendation. Imane stood out prominently among the international students for the independence with which she organised her research, experiments, and investigations, both inside and outside the institute. She communicated confidently with the institute's technicians, whose command of English was not necessarily advanced. Her consistently cheerful personality carried her through the difficult phases of the research that we had.

Those difficulties were totally independent of her, and she always sought solutions to the difficulties that arose. She proactively arranged mobility programs to broaden her professional horizons. She integrated very well into the institute's community. I fully support the awarding of the PhD degree.

Prof. Dr. Valeria Mertinger

Miskolc, 2026.08.06

Acknowledgement

First and foremost, I would like to express my deepest gratitude to my supervisor, Prof. Valeria Mertinger, DSc, for her continuous guidance, expertise, and unwavering support throughout this doctoral research. Her leadership and guidance within the laboratory provided me with the structure, resources, and scientific environment necessary to carry out this work, and her scientific rigour and critical insight have shaped this dissertation at every stage, from the earliest experiments to the final interpretation of results. I am profoundly grateful for the trust and mentorship she has provided throughout this journey.

I would also like to sincerely thank Prof. Yoni Adonyi, PhD, for his invaluable guidance and support throughout this journey. I am especially grateful for the exceptional effort and dedication he devoted during the first stage of my PhD, when he took me on as a fresh MSc graduate with little prior exposure to the field and worked closely with me to introduce me to friction stir welding, shape the research plan that would form the foundation of this dissertation, and gradually develop me into an independent PhD researcher. His generosity with his time, patience, and knowledge during that critical early period gave me the grounding and confidence I needed to carry this work forward.

I would like to extend my sincere thanks to Dr Jeroen De Backer, who served as an industrial advisor for this research. His extensive support and technical guidance during the first stage of my PhD were of great value, and his industrial perspective helped ground this work in the practical realities of friction stir welding technology from an early stage. I would also like to thank Elizabeth Hoyos, representing TWI Ltd., for her role as an industrial advisor throughout this research. Her support and industrial insight, along with TWI Ltd.'s provision of the FSW tools central to this study, were instrumental in connecting this work to real industrial application and practice. I would also like to thank Jesper Everall and Sadeghi Seyed Sina, who completed their MSc studies at University West, Sweden, for their valuable contribution in providing the necessary information regarding the experimental work on the additively manufactured samples, carried out as part of their studies.

I would like to thank Dr László Kuzsella and the Institute of Materials Science and Technology, University of Miskolc, Hungary, for their support and expertise in carrying out the Gleeble physical simulation work central to Chapter 4 of this dissertation. Their guidance in operating the simulator and interpreting the thermal and mechanical transient data was essential to the successful completion of this part of the research.

I would like to thank Dr Dániel Koncz-Horváth and the 3D Lab, University of Miskolc, for their valuable support with the SEM and EBSD analyses conducted throughout this research. Their technical expertise and the facilities provided were essential to characterising the microstructural features central to the findings of this dissertation. I would like to express my special and heartfelt thanks to Árpád Kovács, who sadly passed away, for all his support with the SEM analyses carried out during this research. His technical expertise and willingness to help are deeply appreciated, and his contribution to this work will always be remembered.

I would like to thank Dr Erzsébet Nagy for reviewing all of my scientific reports throughout this research and for her expertise and support with XRD analysis. I would like to thank Anikó Márkusné for the metallographic preparation of the samples examined throughout this research.I would like to thank Dr Tamás Mikó for carrying out the tensile testing presented in this research.I would like to give my special thanks to Dr Toufik Djimaoui for his invaluable scientific support throughout my entire PhD journey. His guidance, insight, and encouragement at every stage of this work have meant a great deal to me, and I am deeply grateful for his presence throughout this journey.

I would like to dedicate this achievement to :

My father, Mohamed Djimaoui. You passed away, but you have never left my heart, not for a single day of this journey. You were, and remain, my idol and my greatest source of motivation, the quiet voice that kept me going through every difficult moment of this work. I carried you with me in every step of this path, and I hope that this achievement makes you proud.

My mother, Fatima Djimaoui, thank you for your endless effort, your continuous support, and for never once letting me doubt that I could reach this point. You are a great mother; more than that, you are the biggest reason I am where I am today. Every sacrifice you made, every night you stayed up worrying about me, every word of encouragement you gave when I needed it most I carry all of it with me in this achievement. None of this would have been possible without you, and I hope it makes you proud, as your love and strength have made me who I am.

To my husband, Mohamed Noufel Bensalah, thank you for being my constant through every step of this journey. You were the one who listened to every worry, no matter how small, and celebrated every little victory as if it were your own. Your patience never wavered, your support never faltered, and you never once hesitated to give me strength when mine ran low. You have been my safe place through the hardest days of this path, and my biggest cheerleader through the best of them. I love you more than words can capture, and I am endlessly grateful to have you by my side. This achievement carries your love in every page, and I could not have asked for a better partner to share this journey with.

I would also like to thank my brothers, Fouzi, Sami, Toufik, Fadi Djimaoui, and Mohamed Dib, for their constant support and encouragement throughout this journey. Each of you, in your own way, has been a source of strength for me, and I am deeply grateful to have you in my life.

To my sisters, Zakia and Nabila Djimaoui, my two guardian angels, thank you for standing by my side through every step of this journey. You are, without question, the best sisters anyone could ask for, always there, always supportive, always believing in me even in the moments I doubted myself. Your love and encouragement have been a constant source of strength, and I carry your support with me in every part of this achievement. I would also like to thank Zohra Bourhil, who has been just as much a sister to me, for her unwavering support and presence.

To my lovely aunt Dalila Djimaoui.

To my second family, the Bensalah family: Zine El Eddine, Khadija, Atef, and Oumaima, thank you for being a second, loving family to me.

To the little angels of the family, Farah, Nazim, Rassim, Ishak, and Yazen.

to my children not yet here, not yet even imagined in the world, but already loved. One day, you will read these words, and I hope that when you do, you will feel proud of your mother, of the path she walked, the challenges she overcame, and the dream she chased and achieved before you ever came into being. Everything I built, I built so that one day, you would have something to look up to.

I would also like to thank my friends, both in Algeria and in Hungary, for their friendship, encouragement, and support throughout this journey. Whether near or far, you have offered comfort during difficult moments and shared in the joy of every small victory along the way, and I am truly grateful to have you in my life.

Finally, I want to thank myself. I thank myself for taking on this challenge not only the challenge of finishing a PhD, but the challenge of stepping far away from the warmth of the loving people who surrounded me to face, alone, difficulties I had never encountered before. I thank myself for finding the strength to endure these five years, for the nights of doubt I pushed through, and for never allowing distance, hardship, or uncertainty to make me give up on this path. And to the little girl inside me who once dreamed of this moment: we did it. We achieved the dream we always had.

Table of Contents

Chapter 1: Motivation and Scope of the Thesis

Friction Stir Welding (FSW) has established itself as one of the most significant advances in solid-state joining technology since its invention in 1991, offering defect-free, high-integrity welds without the drawbacks associated with conventional fusion welding. Its unique combination of mechanical and thermal advantages has driven its adoption across aerospace, automotive, marine, and rail industries, particularly for joining lightweight alloys and, increasingly, dissimilar and high-melting-point materials. However, this expanding range of applications comes at a cost: the welding tool itself is subjected to extreme, coupled thermo-mechanical loading, and its progressive wear and eventual failure remain a persistent barrier to the wider industrial adoption of FSW, particularly for demanding applications involving steels, titanium alloys, and other high-strength materials [1].

Despite the considerable body of research addressing tool wear in FSW, several important gaps remain. Tool degradation is typically assessed in terms of macroscopic geometry loss or overall service life, while the relationship between surface wear evolution and the underlying microstructural transformations driving that wear has rarely been investigated in a systematic, integrated manner. Furthermore, once a tool reaches the end of its service life, very few studies have explored viable repair and life-extension strategies, despite the significant cost implications of replacing high-performance tool materials such as MP159. Finally, most existing studies focus on steady-state welding conditions, while the transient thermo-mechanical effects occurring during the plunge stage arguably the most severe loading condition experienced by the tool remain comparatively underexplored.

This dissertation is motivated by these gaps, and is structured to address them from three complementary angles: first, through detailed characterization of the wear and failure mechanisms observed in real, in-service MP159 SSFSW probes; second, through the development and evaluation of an additive manufacturing-based repair strategy using Laser Metal Deposition with Stellite 6 powder, aimed at extending tool service life and reducing tooling costs; and third, through controlled physical simulation of the thermal and mechanical transients experienced during the plunge stage, using a Gleeble thermo-mechanical simulator, in order to isolate and understand the specific loading conditions that drive early-stage tool degradation. Together, these three investigations aim to build a more complete picture of how FSW tools fail, how their service life might be extended, and how the most severe stage of the welding process, the plunge contributes to that failure.

Beyond the technical and industrial relevance of this topic, my interest in it is also personal. My MSc research focused on TIG welding of automotive tag components, carried out in close collaboration with industry, an experience that gave me an early appreciation for how research grounded in real industrial problems can lead to meaningful, applicable solutions.

That experience shaped the way I approach research more broadly: I am drawn to understanding the reason behind things, not simply observing that a component has failed, but asking why it failed, under what conditions, and through what sequence of physical events. This dissertation reflects the same drive: rather than treating tool failure as an endpoint, it treats it as a starting point for investigation, using the failed material itself as evidence to reconstruct the conditions that led to its degradation, and using that understanding to propose ways to extend tool life and improve process reliability.

Ultimately, this work is intended to contribute both to the fundamental understanding of tool degradation mechanisms in FSW and to the practical, industrially relevant challenge of extending the service life of high-performance tool materials, thereby supporting the continued expansion of friction stir welding into more demanding structural and industrial applications.

Chapter 2: Overview, Generalities, and Literature Review

This chapter provides the general foundation for the present study by introducing the key concepts related to friction stir welding and wear behaviour. It begins with an overview of the fundamental principles of FSW, including its process characteristics and advantages, followed by a discussion of wear mechanisms relevant to the materials under investigation. In addition, a review of the existing literature is presented to highlight prior research, identify current limitations, and provide context and motivation for this work.

2.1. Friction Stir Welding

Friction Stir Welding is a solid-state joining technique invented and patented in 1991 by The Welding Institute (TWI) in the United Kingdom [2]. Unlike traditional friction welding, where the two workpieces are directly rotated or moved to generate friction, FSW utilises a third component: a non-consumable rotating tool consisting of a pin and shoulder (see Figure 1) [3]. This innovation distinguishes friction stir welding from traditional methods, allowing the production of long, continuous welds in plates and sheets of aluminium, steel, magnesium, and copper [4] [5]. During FSW, the rotating tool is plunged into the joint line between two clamped workpieces and traversed along the seam. Friction between the shoulder and the workpiece surface generates heat, softening the material around the pin. The rotating pin then stirs and transports the plasticised material from the front of the tool to the rear, while the downward forging pressure of the shoulder consolidates the material to form a continuous, defect-free solid-state bond [6].

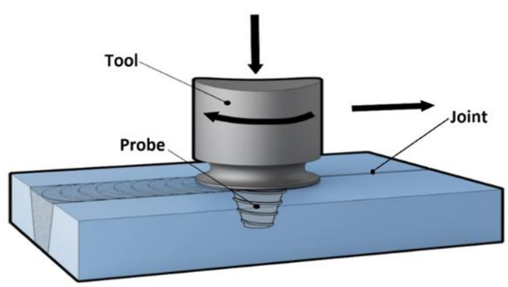

Figure 1. Friction stir welding [7].

The quality and mechanical performance of friction stir welds depend strongly on several interacting process parameters that govern heat generation, plasticised material flow, and forging pressure.

The design of the FSW tool is crucial for producing defect-free joints with superior mechanical properties, as it governs the uniformity of microstructure and mechanical performance and directly influences the process loads during welding [1]. Each geometric characteristic of the tool strongly influences heat generation, plasticised material flow, and the resulting weld integrity. An FSW tool consists of two main components: a shoulder and a pin, as shown in Figure 2 [8]. The shoulder contacts the workpiece surface, producing the majority of frictional heat while forging and confining the softened material, whereas the pin penetrates the joint line to mix and transport the plasticised metal [9].

Figure 2. The FSW tool consists of a pin and a shoulder.

Various pin profiles, such as cylindrical, tapered (frustum), square, hexagonal, cam, threaded cylindrical, and threaded triflute, are used in FSW tools to control material flow and mixing (see Figure 3). Cylindrical and tapered pins mainly move material around the probe, while threaded designs also drive vertical flow, and square, hexagonal, or cam shapes create a pulsating action that enhances mixing and joint strength [10] [11]. However, non-cylindrical profiles tend to wear and gradually become tapered or cylindrical, so the optimal profile balances stirring efficiency with long-term dimensional stability [12].

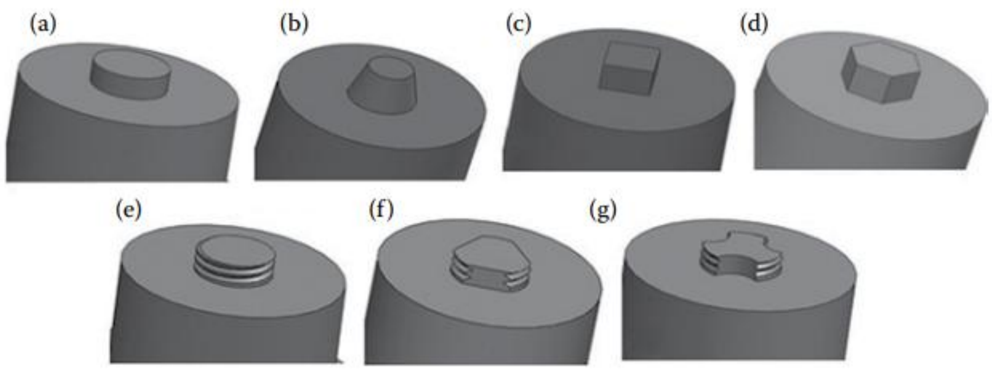

Figure 3. Different FSW tool pin profiles: (a) cylindrical, (b) tapered cylindrical (i.e., frustum of a cone), (c) square, (d) hexagon, (e) threaded cylindrical,(f) threaded cam, and (g) threaded tri flute [13].

Shoulder profiles are also used, designed to suit different materials and conditions as necessary. These shoulder profiles improve the coupling between the tool shoulder and the workpiece by entrapping plasticised material within special re-entrant features. This essentially provides like-to-like frictional contact and improved weld closure by helping prevent plasticised material from being expelled. Examples of different shoulder profiles. Different tool shoulder surface designs used in FSW include flat, concave, scrolled, concentric circle, etc (see Figure 4) [13].

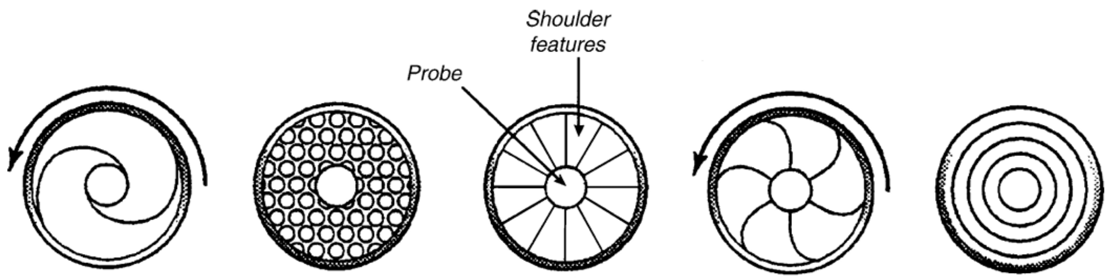

Figure 4. Tool shoulder geometries, viewed from underneath the shoulder [1].

Friction stir welding primarily involves two convenient configurations: butt joints and lap joints. In a simple square butt joint, two plates of equal thickness are clamped to a backing plate to prevent the joint faces from separating during the tool's plunge. Lap joints, on the other hand, consist of two overlapping plates clamped to a backing plate, with a rotating tool plunged through the upper plate into the lower one to join them [1]. Various joint configurations can be created by combining butt and lap joints, and other designs like fillet joints are also possible for specific applications (see Figure 5). Notably, no special surface preparation is needed for FSW, as metal plates can be joined easily without significant concerns about their surface conditions [1].

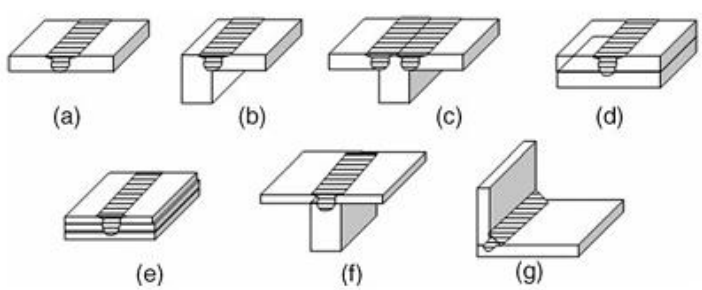

Figure 5. Joint configurations for friction stir welding: (a) square butt, (b) edge butt, (c) T butt joint, (d) lap joint, (e) multiple lap joint, (f) T lap joint, and (g) fillet joint [1].

Friction stir welding is governed by several key process parameters that directly influence heat generation, material flow, and ultimately the quality of the weld. Among these, the most critical parameters include the tool rotational speed, welding (traverse) speed, axial force, tool tilt angle, and plunge depth. The careful control and optimisation of these parameters are essential to ensure proper plasticization of the material, adequate consolidation, and the prevention of defects. Each parameter plays a specific role in the welding process, and their combined effect determines the microstructural evolution and mechanical performance of the joint [1].

The rotational speed of the tool significantly affects frictional heat generation and material softening. If the speed is too low, it can lead to inadequate plasticization and the formation of tunnel defects. Conversely, if the speed is too high, it may result in overheating, grain coarsening, and flash development [14] [15].

It is important to balance the traverse or welding speed with the rotational speed to ensure appropriate heat input and stable material flow. Excessively slow or fast movement can lead to poor consolidation or undesirable microstructural changes [16] [17].

The axial or downward force applied keeps the tool shoulder firmly in contact with the workpiece, promoting the consolidation of the softened material. If the force is insufficient, it may lead to voids or incomplete bonding. On the other hand, excessive force can lead to increased tool wear and reduced weld thickness. The axial force of the tool on the workpiece affects heat generation and, in turn, welding quality. When the axial force is insufficient, heat production is insufficient, which easily causes voids and kissing bond defects at the weld bottom. When the axial force is too large, frictional heat production increases and defects such as flash are more prone to occur [18].

A slight tilt of the tool helps direct the plasticised material from the front to the rear, enhancing consolidation and improving the surface finish [19]. Additionally, the plunge depth, or shoulder penetration, plays a crucial role in controlling the forging action and interfacial heating, both of which are essential for producing a sound, defect-free weld [20] [21].

The Friction Stir Welding process consists of four main stages: the plunge stage, the dwell stage, the welding stage, and the cooling stage, as illustrated in Figure 32 [22]. The process begins with the plunge stage, during which a rotating tool, featuring a shoulder and a pin, is slowly inserted into the edges of the workpieces until the shoulder makes contact with their top surfaces [23]. Next is the dwell stage, where the tool continues to rotate for a period, allowing the material near the tool to soften. Following this is the welding stage, where the rotating tool is moved along the edges of the workpieces, creating a weld joint. Once the desired weld distance is reached, the tool is swiftly removed from the workpiece, leading to a rapid decrease in the temperature of the joint. This final phase is known as the cooling stage [24].

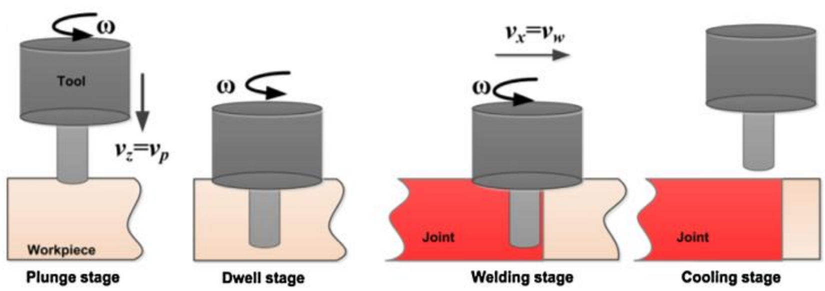

Figure 6. Schematic drawings of different stages in FSW [24].

2.2. Weld microstructure

FSW involves complex interactions between simultaneous thermomechanical processes. These interactions affect the heating and cooling rates, plastic deformation and flow, dynamic recrystallisation phenomena, and the mechanical integrity of the joint [25]. The thermomechanical process involved under the tool results in different microstructural regions (see Figure 7). Some microstructural regions are common to all forms of welding, while others are exclusive to FSW [26]. The stir zone (also called nugget) is a region of deeply deformed material that corresponds approximately to the location of the probe during welding. The grains within the nugget are often an order of magnitude smaller than the grains in the base material. The thermomechanically affected zone (TMAZ) occurs on either side of the stir zone [27]. The strain and temperature levels attained are lower, and the effect of welding on the material microstructure is negligible. The heat-affected zone (HAZ) is common to all welding processes. This region is subjected to a thermal cycle, but it is not deformed during welding [28].

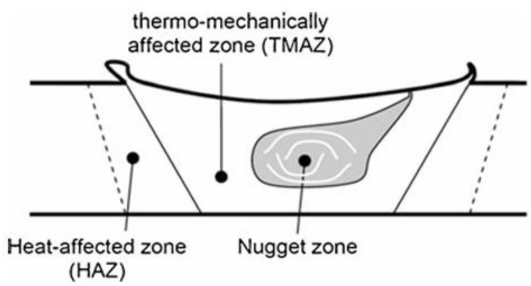

Figure 7. Different microstructural regions in a transverse cross-section of FSW [29].

2.3. Applications, advantages and disadvantages of FSW

Friction Stir Welding offers several significant advantages over traditional fusion welding. Since it is a solid-state process, the metal does not melt, which eliminates common fusion-related defects such as porosity, hot cracking, and solidification shrinkage. The lower heat input reduces distortion, residual stresses, and minimal joint shrinkage, while also producing fine, dynamically recrystallised grains with excellent mechanical properties, including high tensile strength, good fatigue resistance, and improved ductility [30]. Additionally, FSW does not require filler metals, fluxes, or shielding gases, making it a cleaner and more cost-effective process. It is well-suited for automation and robotic applications, ensuring high production consistency. The technique can also join alloys and dissimilar materials that are difficult or impossible to weld using fusion methods, while consuming less energy and generating no fumes or spatter, thus providing environmental and safety benefits. Furthermore, FSW is considered a green technology because it is energy-efficient, produces minimal waste and emissions, and supports sustainable manufacturing practices [31] [32].

Friction Stir Welding has gained widespread industrial application due to its ability to create high-quality, defect-free joints in lightweight and dissimilar materials. In the aerospace and space sectors, it is extensively used for joining fuselage panels, wing skins, cryogenic and propellant tanks, and spacecraft modules, where minimising distortion and ensuring high joint integrity are critical [33]. In the automotive industry, FSW is used on structural panels, chassis components, and battery trays for electric vehicles, thereby reducing weight and enhancing crash performance. The shipbuilding and marine sector utilises FSW for large aluminium hull panels, decks, and offshore structures, thanks to its excellent corrosion resistance and ability to produce long, continuous welds [34]. Additionally, the rail and transportation industries employ FSW to fabricate roof assemblies, sidewalls, and structural sections for railway and metro coaches [35]. Beyond transportation, FSW is increasingly utilised in electronics and thermal management, particularly in the manufacturing of heat exchangers and enclosures that demand superior thermal contact and minimal distortion. FSW also plays a crucial role in general fabrication and structural engineering, including pressure vessels, architectural facades, and large extruded assemblies. Moreover, it is highly effective for joining dissimilar materials, such as aluminium to steel, copper, or magnesium; applications that can be challenging or impossible with traditional fusion welding techniques [36].

Despite its many benefits, Friction Stir Welding has several limitations. It is a solid-state process that requires a non-melting tool to traverse the joint, which limits its use mainly to linear or slightly curved seams and makes welding complex 3-D geometries challenging [1]. Because high forging forces are required, workpieces must be rigidly clamped and supported by a robust fixture or backing plate, which increases setup costs and limits portability [37]. FSW is best suited for non-ferrous and relatively soft metals (e.g., Al, Mg, Cu); welding high-melting or hard materials such as steels, titanium, or thick sections requires special tool materials and high forces, making it more expensive and sometimes impractical. The process can also leave keyhole exit defects where the tool is retracted, and thickness changes or start/stop points need special handling [4]. In addition, tool wear and design complexity can increase costs, particularly when joining abrasive or dissimilar materials [25].

2.4. FSW tool materials

The following characteristics have to be considered for material choice: strength at ambient and elevated temperatures, Elevated-temperature stability to maintain geometry, wear resistance to withstand abrasive material flow, Low chemical reactivity with the base metal, Fracture toughness to avoid breakage, Low and stable coefficient of thermal expansion, and Good machinability to form complex tool profiles [38]. Table 1 summarises the typical tools and base materials.

Table 1.FSW Tool Materials: Properties and Typical Base-Metal Applications [39].

Tool Material	Typical Base Materials	Key Features
Hot-work tool steels (e.g., H13)	Aluminium, copper, and similar low-melting alloys.	Most common, readily available, good machinability, excellent thermal-fatigue, and wear resistance.
Nickel- and cobalt-base alloys	High-strength aluminum or copper alloys	High strength, ductility, and hardness stability; creep-resistant; strength derived from precipitates, so the operating temperature must stay below 600–800 °C to prevent over-ageing.
Refractory metals (W, Mo)	Steel, titanium, nickel-based alloys	Very high strength between 1000–1500 °C; suitable for welding high melting-point materials; expensive; complex to machine; relatively brittle (due to powder metallurgy processing).
Tungsten-base alloys (e.g., W–Re)	(W–Re) Steel, Ni/Ti alloys	Excellent high-temperature strength and wear resistance; capable of sustained use at elevated temperatures; high cost.
Carbide-particle reinforced metal composites (WC, WC–Co, TiC)	Hard or abrasive alloys	Superior wear resistance and reasonable fracture toughness; used when a very long tool life is needed.
Steels with polycrystalline cubic boron nitride (PCBN) coating	Steel, nickel, and titanium alloys	Very high operational temperature capability and outstanding wear resistance; low fracture toughness; expensive tools, but enable joining of very high-melting materials.

H13 tool steel is widely used for friction stir welding tools due to its excellent combination of high-temperature strength, wear resistance, and toughness. As a hot-work tool steel, H13 can retain its hardness at elevated temperatures generated during the FSW process, while also resisting thermal fatigue and softening [40]. These properties make it particularly suitable for welding low to medium-strength materials such as aluminium and magnesium alloys [41]. Additionally, its good toughness helps prevent tool fracture during the plunging and stirring stages of welding. However, H13 has limitations when used with high-melting-point materials such as steel or titanium, where severe wear can occur. Overall, H13 provides a balanced performance and cost-effective solution for many FSW applications, especially in the processing of lightweight alloys [41].

MP159 alloy is a high-performance cobalt–nickel-based superalloy widely used as a probe material in stationary shoulder friction stir welding due to its exceptional mechanical and thermal properties. It possesses a stable face-centred cubic (FCC) austenitic crystal structure, which is maintained even at the elevated temperatures generated during the welding process [42]. This FCC matrix, primarily composed of cobalt, nickel, chromium, and molybdenum, provides excellent ductility and toughness [43]. MP159 superalloy, developed from MP35N in the 1960s–1970s [44], was designed to overcome the relatively low service-strength limitations of earlier MP-series alloys while retaining excellent corrosion resistance [45]. Owing to its high strength, good ductility, and superior corrosion resistance, MP159 is widely used in aerospace applications, particularly for load-bearing components in advanced aero-engines [46]. These characteristics, combined with its outstanding high-temperature strength, corrosion resistance, and durability, make MP159 particularly suitable for the severe thermo-mechanical conditions of SSFSW, especially when welding high-strength or high-melting-point materials such as steels and titanium alloys, despite its higher cost and machining difficulty compared to conventional tool steels like H13.

2.5. Stationary Shoulder Friction Stir Welding (SSFSW)

Stationary shoulder friction stir welding is an advanced solid-state joining technique derived from conventional friction stir welding. In conventional FSW, the rotating shoulder provides most of the frictional heat. In contrast, SSFSW employs a fixed (non-rotating) shoulder, and heat generation comes almost entirely from the rotating probe (pin) [47] [48]. The concept, first proposed by Russell et al. to improve the welding of low-thermal-conductivity titanium alloys, uses a probe rotating within a bearing assembly, with the shoulder remaining static [49]. Because only the probe rotates, SSFSW delivers a more uniform, linear heat input across the joint thickness. This produces a narrower heat-affected zone and thermo-mechanical affected zone, lower distortion, and better weld surface finish (no cross-section reduction), and it facilitates the welding of butt joints of different thicknesses and corner joints [50] [51]. The process can be applied not only to titanium alloys but also to high-conductivity materials like aluminium, where it provides a more parallel thermal field and improved microstructural uniformity. [48] . Compared with conventional FSW, SSFSW offers benefits such as improved appearance, reduced thermal gradients, and minimised residual stresses [52].

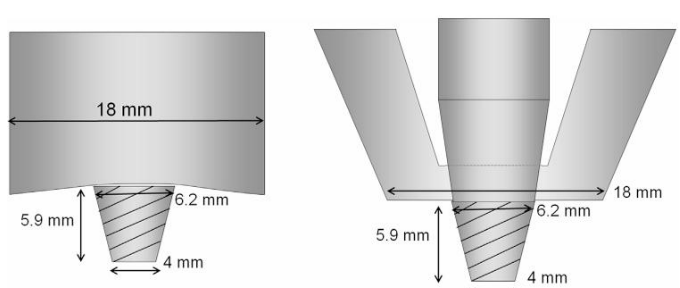

Figure 8. Schematic diagrams of (a) the FSW and (b) the SSFSW tools used in this investigation with their dimensions [48].

2.6. FSW degradation and failure

Understanding and characterising the mechanical forces exerted on the welding tool during Friction Stir Welding is essential for optimising tool design, developing robust clamping configurations, and fundamentally diagnosing tool degradation and failure modes. Precise quantification of these tool forces enables reductions in machine complexity, structural size, and power consumption, thereby lowering operational costs while simultaneously enhancing process productivity [53]. When studying tool life and structural integrity, force characterisation is critical because the tool operates under extreme, coupled thermomechanical loads where mechanical stresses directly drive structural failure [54].

During the FSW process, the tool experiences a complex, three-dimensional state of loading. As shown schematically in Figure 9, these loads can be resolved into three primary orthogonal force components and a rotational torque acting on the tool pin and shoulder [55], [56]:

Vertical Axial Force: Acts normal to the workpiece surface. This force keeps the tool shoulder firmly in contact with the workpiece surface, promoting the consolidation of the softened material. Insufficient axial force leads to incomplete bonding and voids, while excessive force accelerates tool wear.

Longitudinal Force (welding force): Acts parallel to the welding direction. As the FSW tool moves along the joint line, it encounters mechanical resistance from the workpiece, generating longitudinal forces. As the temperature of the material near the tool increases, this resistance and thus the longitudinal force tend to diminish.

Torque force: Represents the rotational resistance opposed by the material against the spinning tool pin and shoulder. The simultaneous rotation and linear motion of the tool create an asymmetric material flow field around the probe, resulting in a lateral (tangential) force component acting in the horizontal plane.

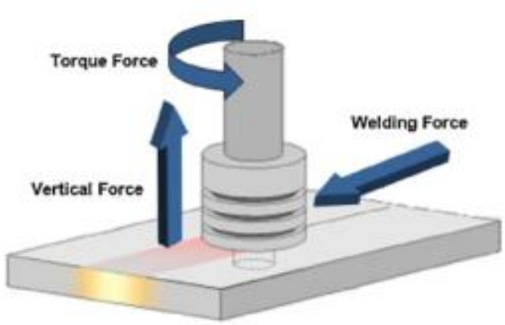

Figure 9. Forces acting on the tool and workpiece during FSW [57].

During friction stir welding of high-melting-point alloys, the welding tool is subjected to severe thermal and mechanical loads, which can lead to multiple degradation and failure modes.

Tool failure occurs mainly through tool wear and plastic deformation [58]. Tool wear can result from mechanical damage or chemical affinity between the tool and the workpiece, while plastic deformation is linked to variations in stress, strain rate, and temperature during welding [59] [60]. Under the high frictional and resultant forces acting on the pin during the initial plunge stage, the tool may undergo degradation mechanisms including plastic deformation, shear-stress-induced cracking, mechanical fracture, diffusion-related damage, tool weight loss, and micro-macro-crack propagation, all of which compromise tool life and weld quality [59]. To better understand these failures, each form is defined as follows :

Abrasive wear: Abrasive wear is a mechanism in which tool or surface material is removed by the mechanical action of hard particles or protuberances at the contact interface. These particles, originating from hard constituents in the workpiece, tool material fragments, or strain-hardened debris, are forced against and move along the surface, producing material loss through cutting, scratching, or ploughing [61].

Adhesive wear: The progressive loss of material that occurs when two solid surfaces slide against each other, with material transferred or detached due to localised bonding and fracture at asperity contacts. During sliding, the asperities of the surfaces come into close contact, and under pressure, they may form localised adhesive junctions or microwelds. As motion continues, these junctions rupture, causing fragments of material to be pulled away from one surface and either adhere to the opposing surface or detach as wear debris. This mechanism removes material from one or both surfaces, a defining feature of adhesive wear [62]. The adhesive wear failure process can be summarised as [63]: 1. Formation of adhesive microjunctions 2. Deformation of contacting asperities 3. Removal of protective oxide surface films 4. Crack initiation and propagation 5. Failure of junctions by shearing and tearing, and by material transfer.

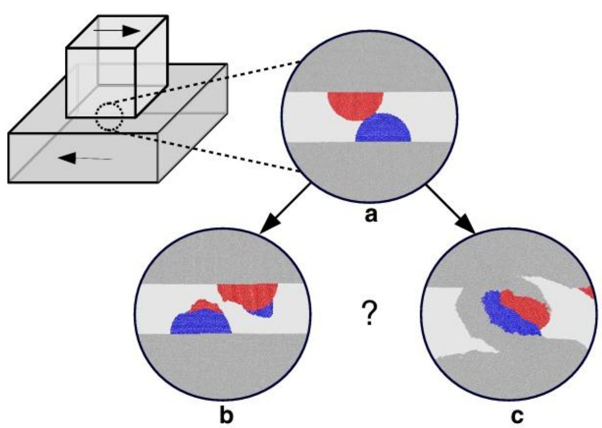

Figure 10. Schematic representation of two possible asperity-level adhesive wear mechanisms [62].

Diffusion wear: A smooth, undamaged surface with no plastic deformation. The material transfer towards the chip eventually forms a crater on the tool rake face [64].

Fatigue and Wear (Fatigue wear): Wear is essentially a fracture process that occurs on sliding surfaces due to repeated mechanical loading. Although hardness influences how much a surface resists deformation, it does not explain how wear particles form and detach. The key factor is the material's fatigue resistance, its ability to withstand cyclic stresses without cracking. During sliding, normal and frictional forces repeatedly act on the same regions, causing localised stress cycles that initiate and grow subsurface cracks, which eventually reach the surface and release small fragments as wear debris. Fatigue in materials occurs in two main forms: high-cycle fatigue, caused by repeated stresses below the yield limit where deformation remains elastic, and low-cycle fatigue, caused by repeated plastic deformation under higher loads. Low-cycle fatigue is especially relevant in adhesive and delamination wear, where surface layers undergo repeated plastic straining with each sliding cycle. Therefore, wear can be understood as a fatigue-driven process in which the rate of wear depends on the rate at which fatigue cracks form and propagate within the material [65].

Delamination wear: When two solid surfaces slide against each other, the load is carried by tiny surface peaks called asperities, which interact through adhesive bonding and plowing. At first, these asperities on the softer surface deform, fracture, and break off, producing small wear particles and gradually smoothing the surface. As sliding continues, most asperities are either flattened or removed, creating smoother contact where the harder surface's asperities slide over a relatively flat plane on the softer material. This changes the contact condition from asperity-to-asperity to asperity-to-plane. Under these conditions, each spot on the softer surface is repeatedly stressed by the harder surface, leading to cyclic subsurface shear stresses. Over time, these stresses cause fatigue cracks to form below the surface and grow parallel to it. When these cracks reach the surface, thin layers of material peel off, a process known as delamination wear [66].

When comparing fatigue wear, delamination wear, and adhesive wear, we can observe that fatigue wear occurs when a material is subjected to repeated loading during sliding or rolling contact. This leads to cyclic stresses that cause cracks to form and grow, either on the surface or beneath it. Over time, these cracks propagate, and small fragments of material break away, resulting in wear [65]. Delamination wear is a specific type of fatigue wear that occurs primarily under sliding conditions, in which subsurface cracks grow parallel to the surface due to repeated shear stresses. These cracks eventually reach the surface, causing thin layers of material to peel off or delaminate, producing flake-like debris [66]. In contrast, adhesive wear occurs when two surfaces slide against each other, and microscopic contact points (asperities) form local adhesive junctions, or microwelds, due to high pressure and temperature. As sliding continues, these junctions break, pulling material from one surface and transferring it to the other or detaching it as debris. In summary, adhesive wear is driven by surface bonding and tearing, while fatigue and delamination wear are driven by cyclic stresses and subsurface crack growth, with delamination wear being the fatigue wear form that causes layer-like peeling of material.

Other important types of wear include corrosive (oxidative), erosive, and fretting wear. Corrosive wear occurs due to chemical reactions, such as oxidation, that weaken the surface of materials. This weakening allows layers to be removed through motion. Specifically, oxidative wear happens when the sliding surfaces are exposed to atmospheric oxygen, leading to corrosion. The corroded layer on the contact surfaces is then gradually worn away during movement [67]. Erosive wear occurs when fast-moving particles or fluid droplets strike a surface, removing material from the surface by an impinging stream of solid particles [68] [69]. Fretting wear develops through small, repetitive vibrations or micro-sliding between contacting surfaces, occurring where the contacting surfaces are not supposed to move relative to each other [70].

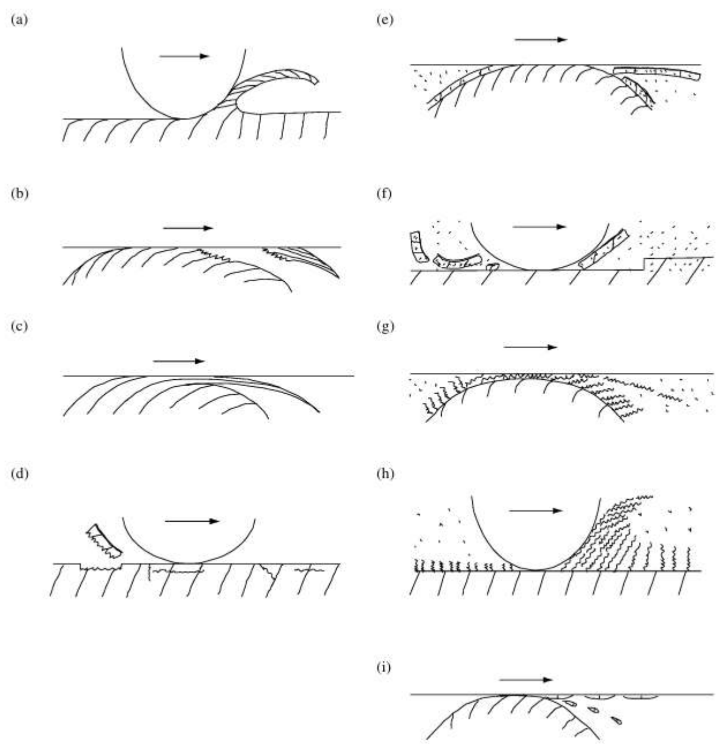

Figure 11. Schematic wear modes: (a) abrasive wear by microcutting of ductile bulk surface; (b) adhesive wear by adhesive shear and transfer; (c) flow wear by accumulated plastic shear flow; (d) fatigue wear by crack initiation and propagation; (e) corrosive wear by shear fracture of ductile tribofilm; (f) corrosive wear by delamination of brittle tribofilm; (g) corrosive wear by accumulated plastic shear flow of soft tribofilm; (h) corrosive wear by shaving of soft tribofilm; and (i) melt wear by local melting and transfer or scattering [71].

This section presents a comprehensive review of the published literature on tool wear in friction stir welding. As tool degradation significantly influences weld quality, process efficiency, and tool life, understanding the mechanisms and factors governing wear is essential for advancing the reliability of the FSW process. The scope of this review is limited to studies focusing on FSW tool wear that depend on tool material, welding parameters, and tool geometry, while the fundamental aspects of friction stir welding were discussed in the previous chapter. The literature is organised thematically to facilitate the critical comparison of findings across studies. Based on this review, existing limitations and research gaps are identified, providing a clear justification for the present research.

A large body of research has shown that tool wear in FSW is governed by complex thermomechanical and tribological interactions at the tool–workpiece interface, where multiple mechanisms, such as abrasion, adhesion, diffusion, oxidation, and plastic deformation, often act simultaneously. For instance, Wang et al. demonstrated that during FSW of Ti-6Al-4V, wear behaviour strongly depends on tool material: W–La_2O_3 tools primarily undergo plastic deformation, whereas WC–Co tools suffer fracture-related wear, with additional adhesive and diffusion wear induced by severe interfacial chemical interactions [59]. Similarly, Farias et al. reported that WC tools used in the friction stir processing of Ti-6Al-4V experience significant hot adhesion and plastic deformation due to elevated temperature and axial pressure, accompanied by material transfer and diffusion that degrade surface quality [72]. These findings highlight that titanium alloys impose extreme conditions that accelerate tool degradation.

In nickel- and cobalt-based systems, wear mechanisms become even more sensitive to thermal loading and material interactions. Du et al. observed that Co-based tools used for FSW of TA5 titanium alloy exhibit a transition in wear mechanisms from abrasion at lower heat input to adhesion and diffusion at higher heat input, with the formation of a W- and Cr-rich interlayer partially mitigating severe wear [73]. In contrast, Hanke et al. reported that pcBN tools used for Ni-based alloy 625 suffer from diffusion-driven grain degradation, binder softening, and grain pull-out, ultimately leading to catastrophic failure, emphasising the limited stability of ceramic-based tools under extreme thermo-mechanical conditions [74]. Ragu Nathan et al. further confirmed that tool composition is critical, showing that W–La_2O_3 tools exhibit superior structural stability compared to lower tungsten-content tools, which fail due to phase instability and matrix decohesion [60].

For steel and high-strength alloys, diffusion and oxidation mechanisms become dominant. Vicharapu et al. showed that WC–Ni tools used in high-carbon steel FSW transition from abrasion-dominated wear at low heat input to adhesion- and oxidation-controlled wear at higher rotational speeds, significantly affecting tool life [75]. Tarasov et al. also emphasised diffusion-controlled degradation in steel tools, in which Fe–Al intermetallic compounds such as $FeAl_3$ form along grain boundaries, leading to embrittlement and fragmentation of the tool material [76]. These studies collectively confirm that diffusion-induced chemical interactions are a key limitation in high-temperature welding environments.

In aluminium alloys and their composites, abrasive wear caused by reinforcement particles and adhesion at elevated temperatures are the dominant mechanisms. Zuo et al. reported severe tool degradation in SiCp/Al composites due to micro-cutting and ploughing by hard SiC particles, while AlCrN coatings initially reduce wear but lose effectiveness upon degradation [77]. Bist et al. similarly highlighted that in aluminium matrix composites, tool wear increases with rotational speed and welding distance, while optimised traverse speed and tool geometry can mitigate wear severity [78]. Netto et al. identified distinct wear stages in H13 tools during FSW of 6061-T6 aluminium, including rapid initial degradation due to thread fracture followed by a quasi-stable wear regime, strongly influenced by insufficient tool hardness [89]. Fritsche et al. and de Castro et al. further showed that in refill friction stir spot welding of aluminium alloys, shoulder wear is particularly critical, with plastic deformation, ridge fracture, and intermetallic formation significantly reducing joint strength and weld quality [79] [80].

Process parameters have also been widely recognised as key factors controlling wear evolution. Sahlot et al. demonstrated that higher rotational speeds increase wear rates in H13 tools used for CuCrZr welding, while higher traverse speeds reduce tool–workpiece interaction time and thus reduce wear [81]. Hasieber et al. further quantified a maximum tolerable wear threshold and showed that tool wear is strongly temperature-dependent, with excessive degradation occurring near the secondary hardness peak of the tool material; reducing the rotational speed was found to significantly extend tool life [82]. These findings emphasise the direct coupling between thermal conditions and tool degradation.

From a modelling and monitoring perspective, significant progress has been made in predicting and detecting the evolution of tool wear. Wang et al. proposed a vibration-based monitoring approach using a CNN-BiLSTM-Attention model, demonstrating that time–frequency features can effectively classify wear states during FSW lap welding [82]. In parallel, Das et al. developed a thermomechanical model incorporating tool wear effects, demonstrating that reductions in pin length and material adhesion significantly influence defect formation, such as tunnel defects, in dissimilar welding [83]. Sahlot and Arora further advanced this area by developing a 3D numerical model based on Archard's wear law, successfully predicting worn pin profiles and demonstrating progressive self-optimisation of tool geometry during welding [84].

Surface engineering and lubrication approaches have also been explored to mitigate wear. Liu et al. showed that tungsten boride coatings exhibit excellent hardness and oxidation resistance at elevated temperatures, with wear mechanisms transitioning depending on environmental conditions, suggesting strong potential for tool protection [84]. Sarmadi et al. demonstrated that incorporating graphite in copper–graphite composites significantly reduces friction and wear by forming lubricating tribolayers and shifting wear from adhesive to delamination modes [85].

Finally, studies on tool failure behaviour underline the importance of material selection and metallurgical stability. Mahto et al. reported that WC tools with higher cobalt content undergo plastic deformation and oxidation, while low-cobalt tools fail in a brittle manner without prior deformation, highlighting the role of binder composition in tool reliability [86]. Wang et al. [59], Ragu Nathan et al. [60], and others collectively confirm that tool material selection remains one of the most critical factors in determining wear resistance and process stability in FSW.

Overall, the literature clearly indicates that tool wear in friction stir welding is a multifaceted phenomenon governed by coupled thermal, mechanical, and chemical effects. Despite extensive research, gaps remain in accurately predicting wear evolution under varying process conditions and in developing universally durable tool materials that resist combined abrasion, adhesion, and diffusion mechanisms. These gaps motivate the present study.

2.7. Knowledge Gaps

Although extensive research has been conducted on tool wear in friction stir welding, several important aspects remain insufficiently understood. Most existing studies focus on steady-state welding conditions, while transient thermo-mechanical effects during the plunge stage have received limited attention, despite this stage being characterised by severe thermal gradients, rapid changes in material flow, and high mechanical loading that may significantly influence early-stage tool degradation. Furthermore, tool wear has predominantly been evaluated in terms of macroscopic geometry loss or overall tool life. In contrast, the relationship between surface wear evolution, microstructural changes within the tool material, and associated alterations in material integrity has not been systematically investigated. The interaction between wear-induced surface modification, microstructural transformation, and local material degradation, therefore, remains unclear.

In addition, research on tool repair and life-extension strategies for friction stir welding remains limited. Only a small number of studies have explored the repair of worn tools, primarily focusing on H13 tool steel reference, and the feasibility of restoring tool functionality through additive manufacturing techniques remains largely unexplored. In particular, the application of additive repair using high-performance alloys such as MP159 has not been comprehensively investigated, despite its potential advantages in terms of high-temperature strength and wear resistance. These limitations highlight the need for a systematic investigation of transient wear behaviour during the plunge stage, the relationship between surface degradation and microstructural evolution, and the feasibility of advanced repair strategies to extend tool service life, which constitute the primary objectives of the present study.

Chapter 3: Experimental results: Characterisation of MP159 probe wear and failure

This chapter presents a detailed characterisation of the wear and failure mechanisms observed in a worn MP159 probe used in Stationary Shoulder Friction Stir Welding. Characterisation was carried out using the worn surface and subsurface microstructures as primary evidence to reconstruct the sequence of events leading to failure. The investigation combines macroscopic and scanning electron microscopy of the worn surface to identify the dominant wear and fracture mechanisms, with longitudinal cross-sectional metallographic and hardness analysis to examine how the microstructure evolves with increasing distance from the worn surface. Together, these observations are used to build a coherent picture of how the probe degraded in service, linking the surface-level damage to the underlying microstructural changes responsible for it.

3.1. Experimental and testing methods

The sample investigated in this study consisted of an in-service-worn/failed MP159 probe used in stationary shoulder friction stir welding. The material properties and metallurgical background of MP159 were detailed in Chapter 2:, its nominal chemical composition is shown in Table 2. The probe examined in this chapter and the substrates used for the additive repair trials described in Chapter 04 originate from the same in-service MP159 SSFSW probes. Following removal from service, the failed tip region of each probe, the section exhibiting visible wear and surface damage (see Figure 12), was sectioned off and retained for the wear and failure characterisation presented in this chapter. In contrast, the remaining, undamaged shank section of the same probe body was preserved and subsequently used as the substrate for the Laser Metal Deposition rebuilding trials reported in Chapter 04. Consequently, the chemical composition reported in Table 2 applies equally to the substrate material used in the rebuilding study.

Figure 12. As-received, out-of-service MP159 SSFSW probe showing the failed tip region. The affected (failed) section was subsequently sectioned from the remainder of the probe for detailed characterisation.

Table 2.Composition of elements of MP159 alloy [87].

Element	Co	Ni	Cr	Fe	Mo	Ti	Nb	Al
Wt %	35.7	25.5	19.0	9.0	7	3	0.6	0.2

Both probes were known to have been used for SSFSW of aluminium plates over long weld lengths; however, no further service history (e.g., number of welds performed, specific process parameters, or exact cause of removal from service) was available for either probe. Consequently, characterisation was performed retrospectively, using surface wear morphology and subsurface microstructural features as the primary evidence for reconstructing the probes' failure history and correlating it with the observed failure mode.

The as-received worn surface of the probe was first examined using a Zeiss SteREO Discovery.V12 stereomicroscope to obtain low-magnification overview images documenting the macroscopic wear morphology, geometric asymmetry, and surface discolouration (heat tinting) of the probe tip. Subsequently, the worn surface was examined using a scanning electron microscope (Zeiss EVOMA 10) in secondary electron (SE) mode to characterise surface topography, wear features, and surface damage in greater detail.

Following surface characterisation, the probe was longitudinally sectioned to expose its internal microstructure along its central axis (see Figure 13). The sectioned sample was hot-mounted and prepared using standard metallographic grinding and polishing procedures to achieve a mirror-like surface finish suitable for microstructural examination. The polished sample was then chemically etched using aqua regia, prepared from 60 mL hydrochloric acid (HCl) and 20 mL nitric acid (HNO_3), applied for 45 seconds to reveal the grain structure and microstructural features of the MP159 alloy.

Figure 13. Sectioned MP159 probe sample after metallographic preparation (grinding and polishing), showing the exposed longitudinal cross-section prior to etching.

Vickers microhardness testing was performed along the longitudinal section of the probe using a Wilson Instrument (Instron) hardness tester, applying a load of 3 kgf (HV3).

Indentations were spaced at 0.3 mm along the traverse direction, yielding a hardness profile across the examined region.

3.2. Results and discussion

Figure 14 presents a macroscopic (stereomicroscope) image of the worn surface of the failed MP159 probe. The surface exhibits pronounced concentric circular wear features, consistent with material removal under rotational sliding contact. Multiple concentric grooves and bands are visible, radiating outward from the tip's centre toward its outer edge, indicating a systematic, repeated wear pattern rather than isolated or random damage.

A distinct radial variation in surface colouration is observed, transitioning from a reddish-orange/gold tone at the tip centre to bluish-purple interference bands in the mid-radius region, and finally to darker, more oxidised regions toward the periphery. This progressive colour gradation is typically associated with variations in the localised surface temperature reached during service.

In addition to the concentric wear grooves, several irregular dark patches are visible, particularly toward the outer edge of the worn region, where the surface appears rougher and less reflective than the smoother, lighter-toned bands closer to the centre. These regions are consistent with localised material delamination and surface fragmentation, superimposed on the underlying circular wear pattern. Fine parallel scratch marks are also visible within several of the concentric bands, indicating additional abrasive sliding contact superimposed on the dominant circular adhesive wear morphology.

Overall, the surface displays a combination of concentric wear grooves, a radial thermal discolouration gradient, delamination in several sub-regions, and superimposed fine scratching, indicating a complex, multi-mechanism surface degradation process.

Figure 15 presents a scanning electron microscope image of the same worn surface, acquired in backscattered electron (BSE) mode at small magnification. At this magnification, the macroscopically observed concentric wear pattern is confirmed and resolved in greater detail, revealing a series of curved, overlapping wear bands that spiral outward from the tip's centre toward its periphery. The bright, smooth regions correspond to areas of relatively continuous surface material. In contrast, the darker, irregular patches, concentrated mainly in the upper-left and lower-central regions of the image, are consistent with localised material loss, fragmentation, or debris accumulation within the wear grooves. A fine radial and circumferential scratch pattern is also visible superimposed on the wear bands, most clearly in the outer periphery of the imaged area, indicating repeated abrasive contact consistent with the macroscopic scratching noted previously. Overall, the SEM image corroborates the multi-mechanism surface degradation identified at lower magnification and additionally reveals finer-scale fragmentation and debris within the dark regions that were not resolvable in the stereomicroscope image.

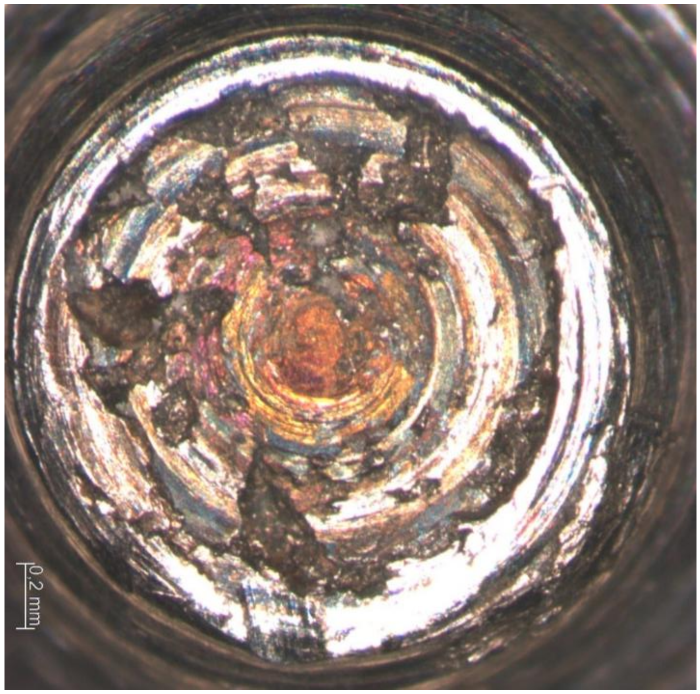

Figure 14. Stereomicroscope image of the failed MP159 probe surface showing concentric wear and thermal discolouration.

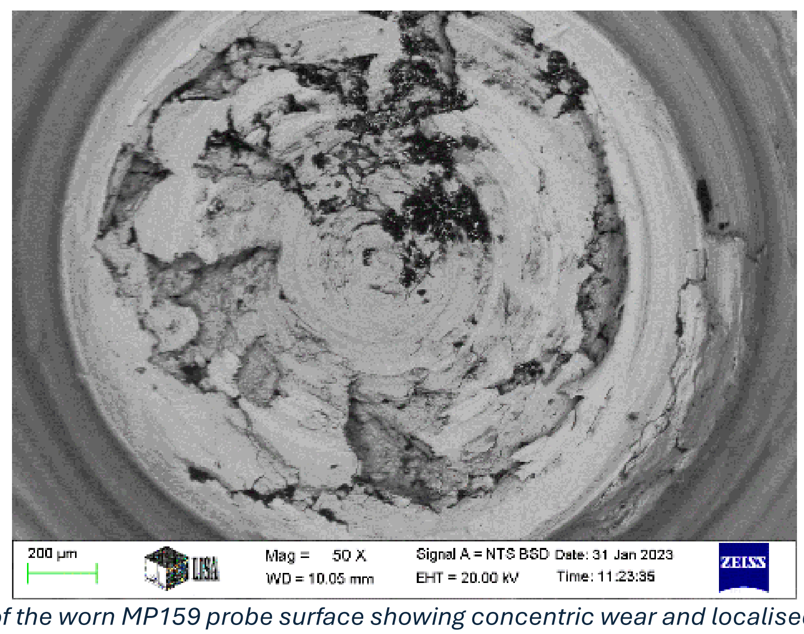

Figure 15.SEM of the worn MP159 probe surface showing concentric wear and localised fragmentation.

Beyond the general fragmentation and debris identified at lower magnification, closer examination of the failed surface reveals several distinct forms of localised failure, each pointing to a different underlying mechanism. In one region, the surface has separated along a sharply defined, jagged front, leaving a partially detached fragment still attached to the surrounding material, a signature of a crack that has propagated beneath the surface before breaking through (see Figure 16a). Elsewhere, rather than a single fracture front, entire surface layers appear to have lifted away from the bulk material: in one area an outer layer has torn free to expose a rougher stratum beneath, with fragmented debris still clinging to the edges of the separation (see Figure 16b), while in an adjacent area the surface instead shows a stepped, ledge-like transition marking a discrete delamination front between an intact upper layer and the exposed layer beneath it (see Figure 16c). A markedly different morphology is seen in a further region, where the surface is smooth and gently undulating, with no sharp edges or torn material, indicating that this area deformed plastically under localised stress and temperature rather than fracturing outright (see Figure 16d). Finally, two additional regions display closely spaced parallel striations and grooves alongside smeared, torn material, consistent with repeated micro-welding and tearing between the probe and the counter-surface during sliding contact the classic signature of severe adhesive wear (see Figure 16 e, f).

Taken together, these observations show that the failed surface does not reflect a single wear process, but rather several coexisting forms of damage, cracking, delamination, plastic deformation, and adhesive wear, each visible in a different region of the same surface.

This coexistence of adhesive wear, plastic deformation, cracking, and delamination on a single surface is unlikely to reflect four independent processes acting by chance; rather, it points to a coupled, sequential degradation sequence. The severe adhesive wear observed in Figure 16e and Figure 16 f most plausibly represents the dominant, ongoing wear process throughout service, driven by repeated intimate contact and localised adhesion between the probe and workpiece under the high contact pressures and interfacial temperatures characteristic of friction stir welding. This sustained frictional interaction would also be expected to promote the localised plastic deformation seen in Figure 16d, as near-surface material is repeatedly pushed and smeared under high stress and temperature without immediately fracturing. With continued cyclic loading, this plastically deformed layer becomes a favourable site for crack initiation, consistent with the propagating crack front captured in Figure 16a. As such, subsurface cracks extend toward the surface, or link with one another, they would be expected to detach discrete surface layers precisely the delamination fronts documented in Figure 16b and Figure 16c. Read this way, the four features are not separate failure modes but successive stages of a single degradation pathway: adhesive wear and the associated frictional heating drive plastic deformation, which promotes crack initiation and propagation, culminating in delamination as the final stage of material loss. This proposed sequence will be examined further alongside the microstructural and hardness data presented next.

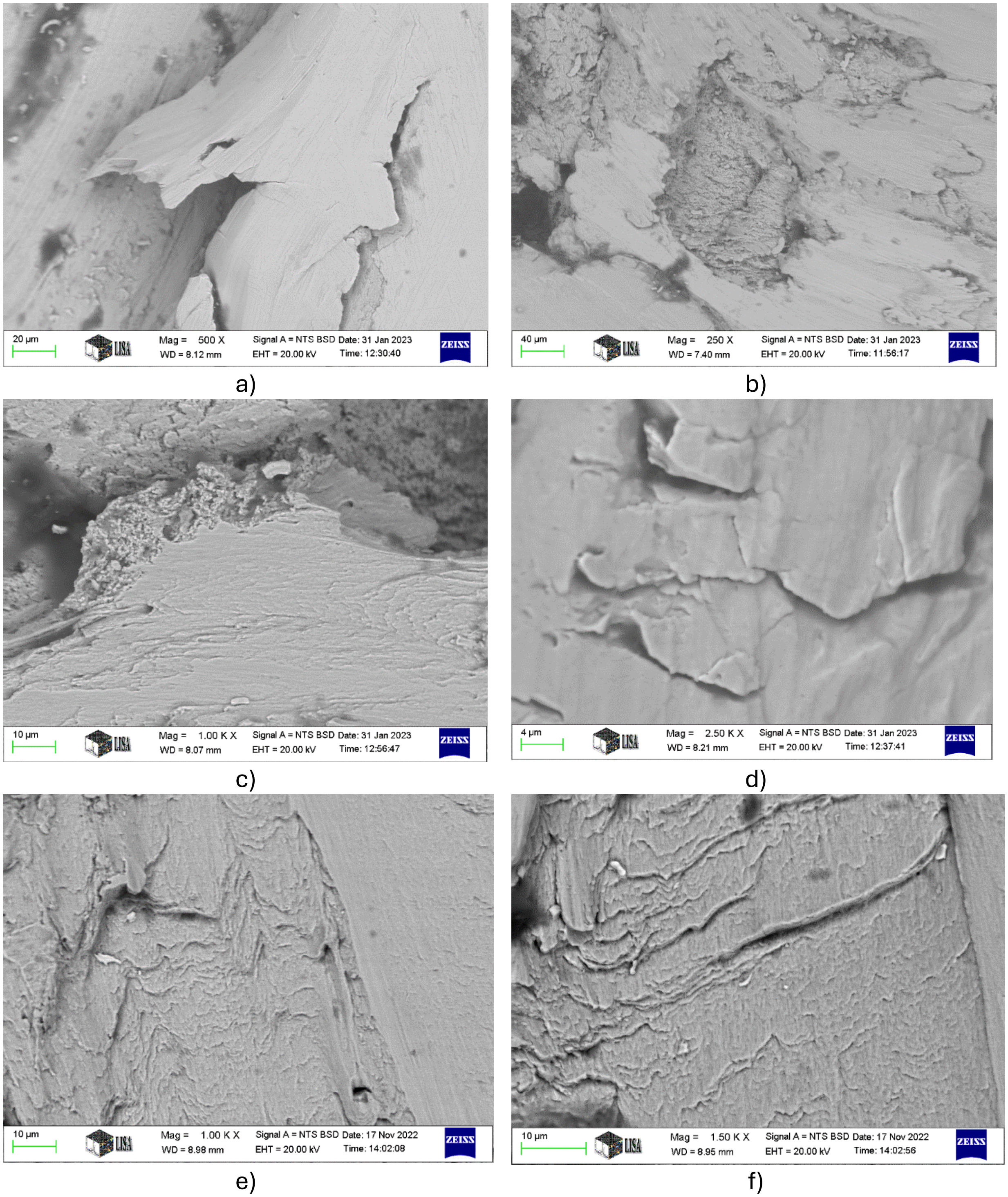

Figure 16.SEM images of the failed MP159 probe surface illustrating distinct wear/failure mechanisms: (a) crack propagation, (b, c) delamination, (d) plastic deformation, (e, f) severe adhesive wear.

A further region of the failed surface reveals a well-defined delamination site, examined at increasing magnification to characterise both its overall morphology and the underlying microstructure exposed by material loss (see Figure 17). At lower magnification, the delaminated zone appears as a triangular, crater-like depression bounded by a sharply defined, irregular edge, consistent with the boundary along which a discrete surface layer has detached from the surrounding material (see Figure 17a). The exposed floor of the depression displays a granular, mottled texture distinct from the smoother surrounding surface, indicating that delamination in this region extended to a structurally distinct sub-layer rather than merely removing a thin superficial film.

Examination of this exposed floor at higher magnification reveals a fine, equiaxed granular morphology, composed of closely packed, rounded units of relatively uniform size, densely and homogeneously distributed across the exposed surface (see Figure 17b). At the highest magnification, this granular structure is resolved further into discrete, well-delineated grains with clearly visible boundaries between adjacent units (Figure 17 c). The fracture path traces predominantly along these grain boundaries rather than through the grain interiors, giving the surface a characteristic rounded, "cobblestone"-like appearance. This morphology is consistent with intergranular fracture, distinct from the flat, faceted planes expected of transgranular cleavage and from the cup-like dimples characteristic of ductile microvoid coalescence. The fine grain size and homogeneous distribution observed within the delaminated region contrast with the coarser, banded morphology noted in the surrounding wear-affected surface, suggesting that the material exposed by delamination corresponds to a microstructurally distinct subsurface layer.

The second delamination site was examined to verify whether the intergranular fracture morphology identified previously was a localised occurrence or a more general feature of the probe surface (Figure 18). As before, the exposed fracture surface is bordered by a distinct delamination front separating it from the adjacent intact surface (Figure 18a). It resolves at higher magnification into a dense population of fine, rounded grains with fracture paths tracing along grain boundaries rather than through grain interiors (Figure 18b, c). No cleavage facets or ductile dimples are observed, confirming the same intergranular fracture morphology identified at the first site (Figure 17).

The recurrence of this granular, intergranular morphology across two independent delamination sites indicates that this is a systematic rather than incidental fracture characteristic of the probe surface.

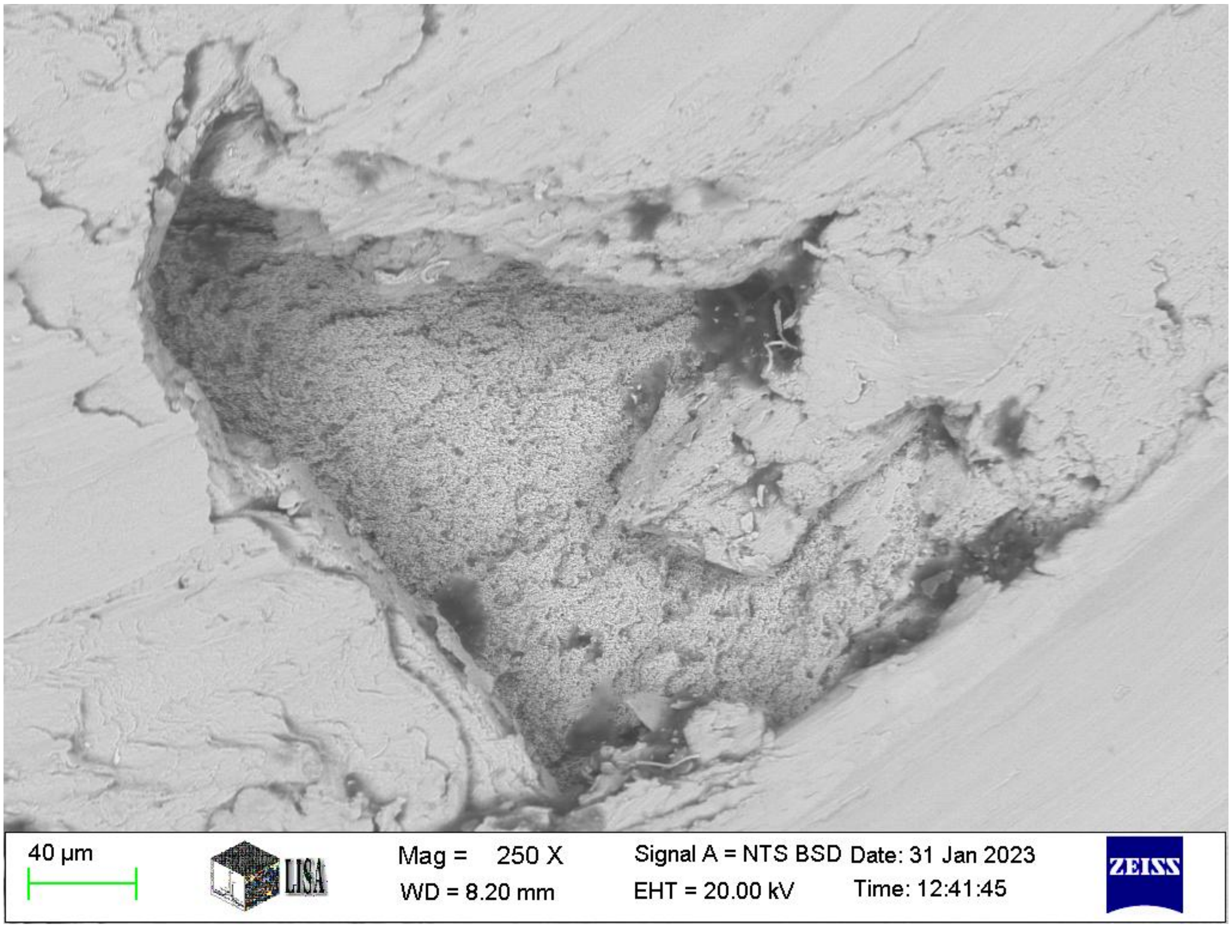

a)

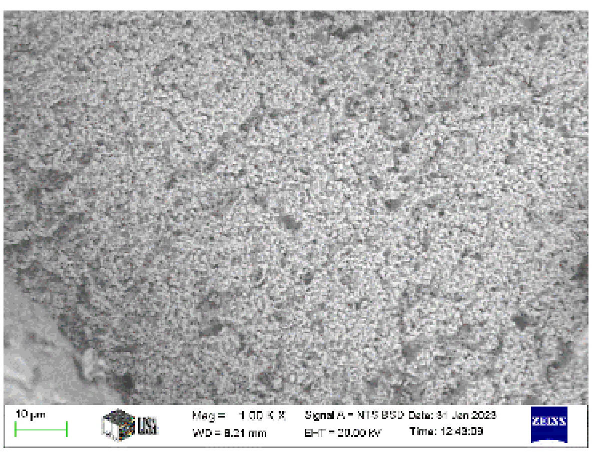

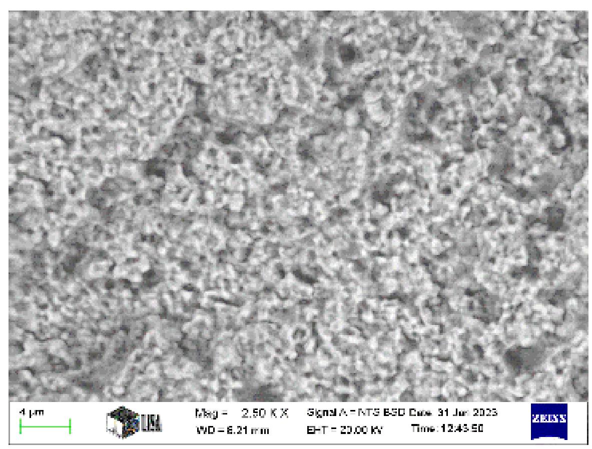

b) c)

Figure 17.SEM (BSE mode) micrographs of the first delaminated region on the failed MP159 probe surface at increasing magnification: (a) 250×, (b) 1.00 K×, (c) 2.50 K×, showing the granular fracture surface exposed beneath the detached layer.

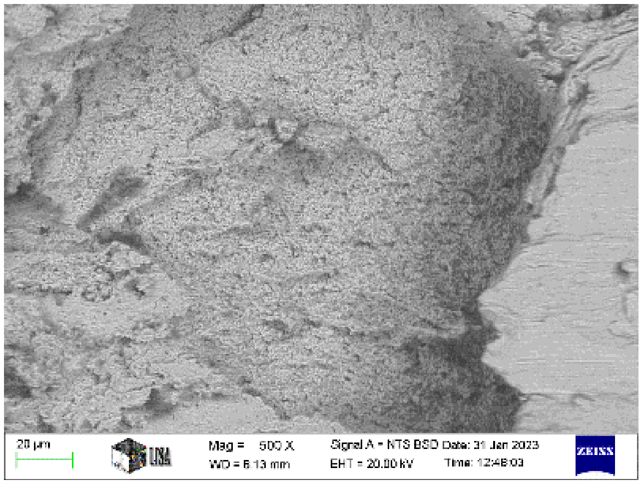

a)

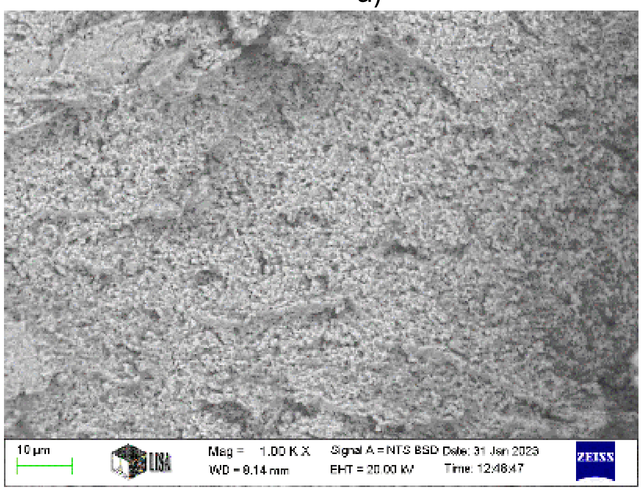

b)

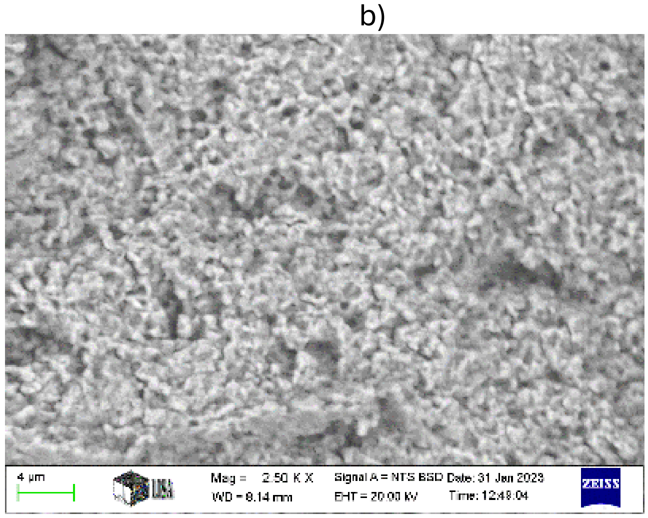

c)

Figure 18. SEM micrographs of a second delaminated region on the failed MP159 probe surface at increasing magnification: (a) 500×, (b) 1.00 K×, (c) 2.50 K×, showing the granular fracture surface exposed beneath the detached layer

The two delaminated regions examined on the failed probe surface (Figure 17 and Figure 18) reveal a consistent intergranular fracture morphology, characterised by fine, rounded grains with fracture paths tracing predominantly along grain boundaries rather than through grain interiors. The reproducibility of this morphology across two independent sites indicates that grain boundary weakening was not confined to an isolated defect or localised inclusion, but rather reflects a broader, systematically distributed condition within the near-surface material of the probe.

Such consistent intergranular separation is generally associated with mechanisms that locally reduce grain boundary cohesion relative to the surrounding matrix, including precipitation of brittle phases along boundaries, boundary oxidation, or grain boundary sliding under sustained thermal exposure. Given the elevated interfacial temperatures generated during friction stir welding, sustained frictional heating at the probe surface is a plausible driver of progressive grain boundary embrittlement across this near-surface layer, providing a consistent explanation for the recurrence of this fracture mode at multiple, unrelated locations.

The cyclic nature of the mechanical loading associated with repeated welding passes, together with the fatigue-consistent striations and crack propagation features identified elsewhere on the same surface, suggests that mechanical fatigue may have contributed to crack initiation and growth along these pre-weakened boundaries. However, neither delaminated region examined here shows striations or other fatigue-specific markers within the fracture surface itself, and the intergranular morphology observed is equally consistent with a thermally-driven weakening mechanism operating independently of cyclic loading. On this basis, the delamination observed across both regions is best interpreted as resulting from a combination of thermally-induced grain boundary embrittlement and cyclic mechanical stress, rather than being attributed to a single, confirmed mechanism at this stage. This interpretation will be examined further in relation to the cross-sectional microstructural and hardness data presented in the following sections, which should help clarify whether the near-surface grain boundary condition responsible for this recurring intergranular fracture is thermally driven, mechanically driven, or a combined effect of both.

Figure 19a presents a low-magnification cross-sectional overview of the failed MP159 probe, showing the transition from the worn surface into the underlying material. Three distinct microstructural zones are identified across this section, labelled (a), (b), and (c). Zone (c), located furthest from the worn surface, corresponds to the original, unaffected base microstructure of the probe. Zone (a), located immediately adjacent to the failed/worn surface, represents the region of material most directly affected by service conditions, while zone (b) represents an intermediate transition region situated between the near-surface affected zone (a) and the unaffected bulk material (c).

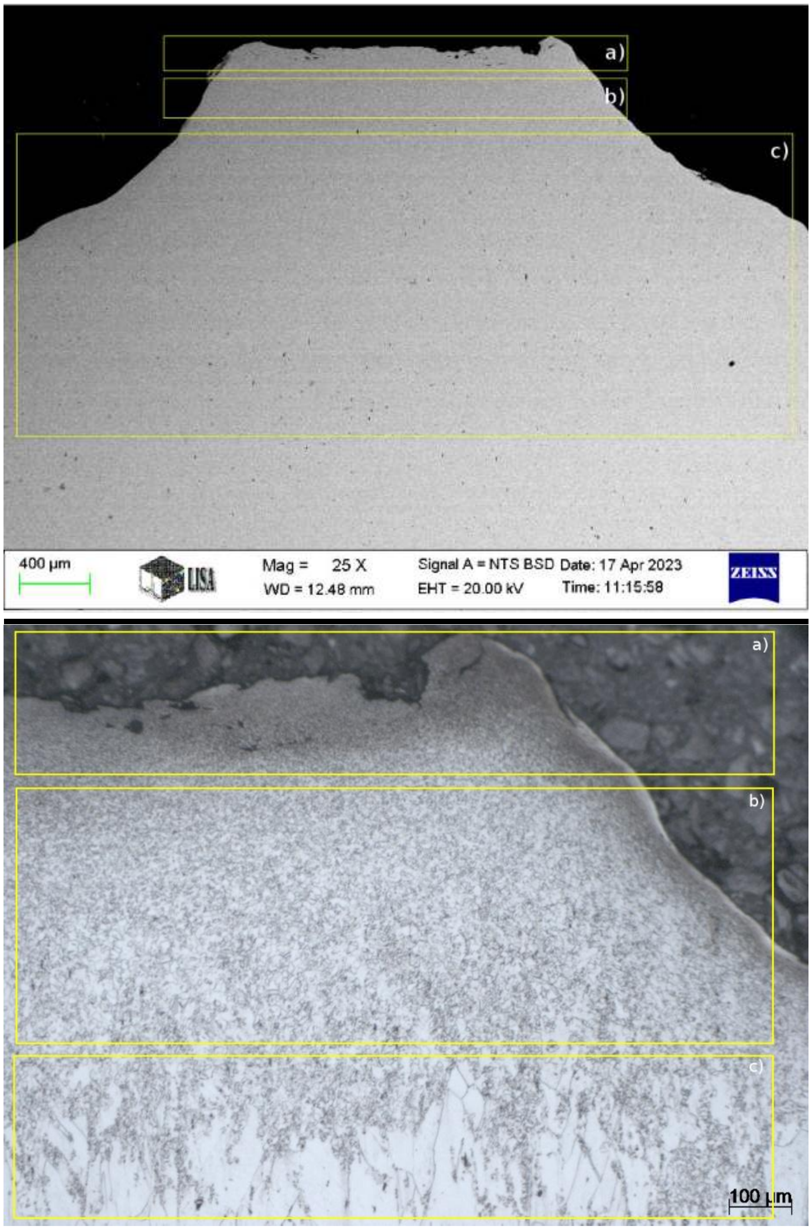

a)

b)

Figure 19.SEM cross-sectional micrographs of the failed MP159 probe showing the three identified microstructural zones: (a) near-surface zone immediately below the worn/failed surface, (b) intermediate transition zone, and (c) original/unaffected base microstructure.

Figure 19b presents a higher-magnification view of zones (b) and (b), allowing closer examination of the transition between the near-surface affected region and the underlying material. At this magnification, zone (a) displays a visibly different microstructural texture compared to zone (b), with the boundary between the two regions appearing as a relatively continuous, wavy interface running roughly parallel to the original worn surface, rather than a sharp, discrete line. This gradational transition suggests that the microstructural alteration associated with the near-surface zone (a) diminishes progressively with increasing distance from the worn surface, rather than terminating abruptly at a fixed depth. Figure 20 presents a micrograph of zone (c), corresponding to the original, unaffected base microstructure of the MP159 probe, located away from the influence of the worn/failed surface. The microstructure consists of relatively coarse, equiaxed grains, with clearly defined grain boundaries. Numerous straight, parallel-sided annealing twin boundaries are visible within several grains, consistent with the face-centred cubic crystal structure characteristic of Co-Ni-based superalloys such as MP159.

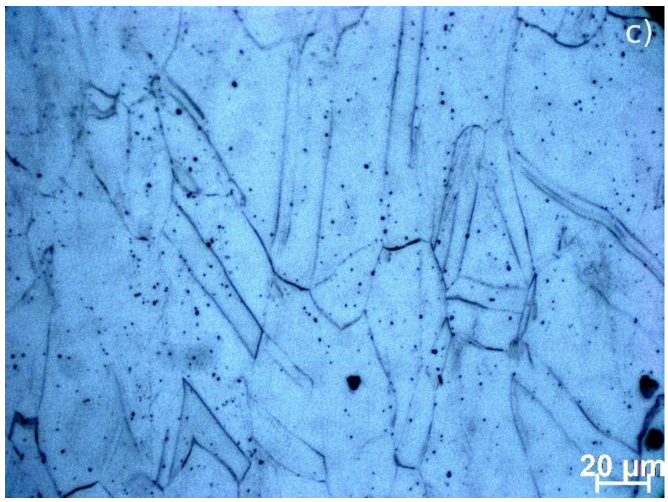

Figure 20. Optical micrograph of zone (c), showing the original/unaffected base microstructure of the MP159 probe, with coarse equiaxed grains, annealing twin boundaries, and fine secondary-phase particles.

Figure 21 presents the microstructure of zone (b), the intermediate transition region situated between the near-surface affected zone (a) and the unaffected base material (c). In contrast to the coarse, equiaxed grain structure observed in zone (c), zone (b) displays a markedly finer, densely packed, equiaxed grain structure, with a substantially higher density of grain boundaries per unit area. The coarse annealing twin boundaries characteristic of zone (c) are notably absent in this region. This fine, uniformly equiaxed grain morphology, together with the absence of the original twin structure, is consistent with dynamic recrystallisation having occurred within this zone . The microstructural comparison between zones (b) and (c) provides direct evidence that recrystallisation occurred in zone (b). The base material (zone c) retains coarse grains containing well-defined annealing twins, a feature characteristic of the original, as-processed condition of the alloy. In zone (b), however, these annealing twins are no longer present, and the grain structure instead consists of fine, uniformly equiaxed grains. The disappearance of the original twin structure, together with the substantial reduction in grain size, indicates that the original coarse-grained structure in this region was replaced by a new population of strain-free grains the defining signature of recrystallisation. This confirms that the near-surface region of the probe was subjected to a combination of temperature and strain sufficient to satisfy the conditions required for recrystallisation during service, consistent with the frictional heating and cyclic mechanical loading generated at the worn surface during friction stir welding.

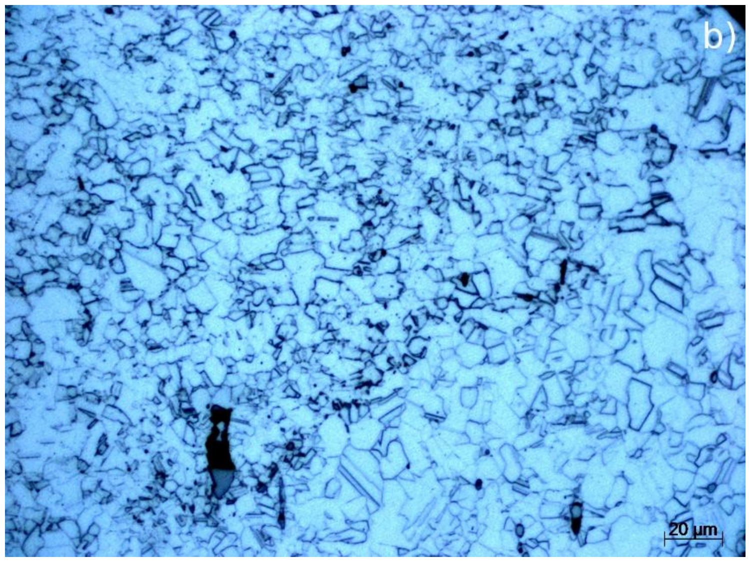

Figure 21.Optical micrograph of zone (b), showing a fine, equiaxed grain structure consistent with dynamic recrystallisation.

Figure 22 presents SEM micrographs of zone (a), the region located immediately below the failed/worn surface, examined at two magnifications from the same location to characterize the near-surface microstructure in detail. In Figure 22a, the microstructure consists of an extremely fine, densely packed equiaxed grain structure with irregular, faceted boundaries, together with numerous small dark pores or voids distributed throughout the imaged area. The grain size in this region is dramatically reduced compared to both the intermediate transition zone (b) and the coarse-grained base material of zone (c), indicating a substantially more severe degree of microstructural refinement in this near-surface layer. Notably, the coarse annealing twin boundaries characteristic of the base material (zone c, Figure 20) are entirely absent from this region.

At higher magnification, taken from the same location, Figure 22b reveals that several of these fine grains display a degree of elongation, giving a locally lath-like or acicular appearance rather than a fully equiaxed one

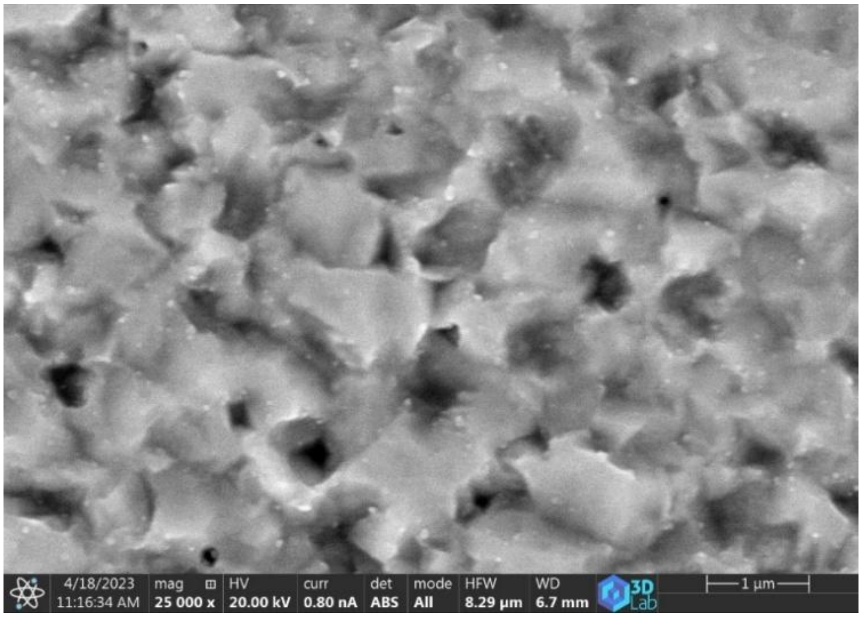

a)

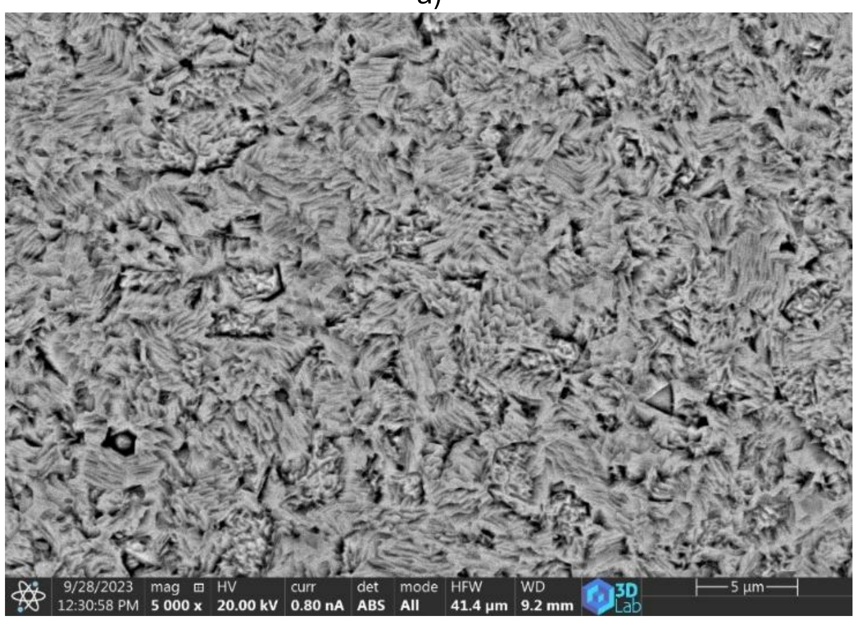

b)

Figure 22.SEM micrographs of zone (a), the near-surface region immediately below the failed/worn surface: (a) 25,000× magnification showing an extremely fine-grained microstructure, and (b) 5,000× magnification showing an acicular, lath-like morphology, both consistent with a severely plastically deformed microstructure.

Figure 23 presents the Vickers microhardness (HV3) profile measured along the longitudinal cross-section of the probe, from the worn surface into the underlying material at 0.3 mm intervals. The hardness profile can be correlated with the three microstructural zones identified in Figure 19. Point 1 (0–0.3 mm from the worn surface), corresponding to zone (a), records the lowest hardness on the profile at 355 HV. Hardness then rises progressively across points 2–6 (~0.3–1.8 mm), a region corresponding to the intermediate transition zone (b), reaching approximately 510 HV by point 6. Beyond point 6 (from ~1.8 mm onward), hardness plateaus, fluctuating narrowly between 495 and 540 HV through to the final measurement point (point 14), corresponding to the unaffected base material of zone (c).

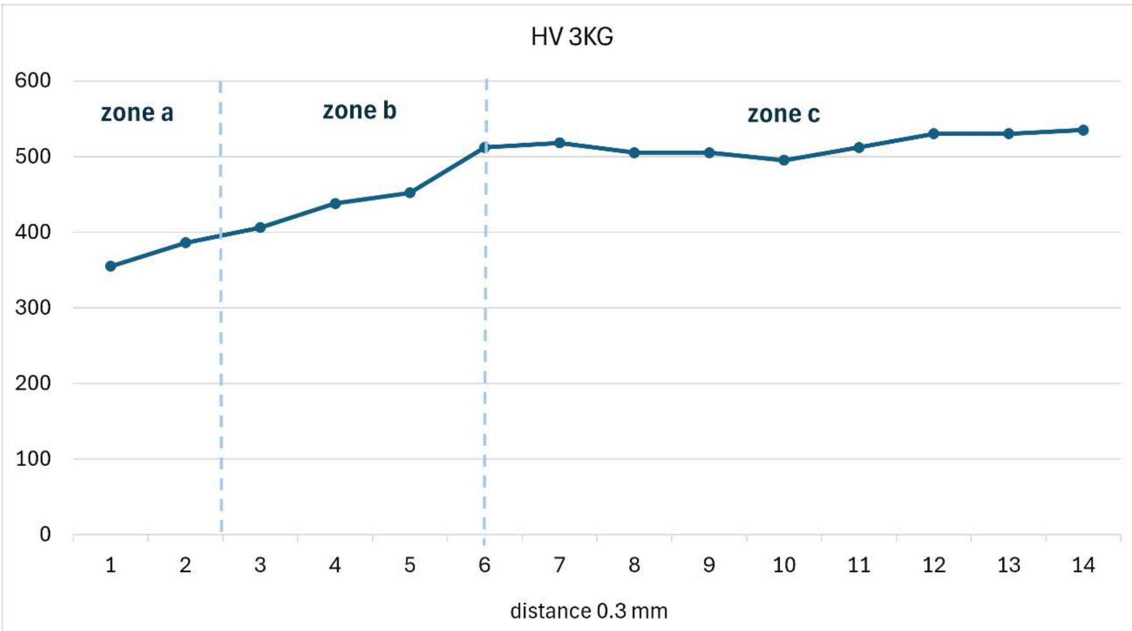

Figure 23.Vickers microhardness (HV3) profile measured along the longitudinal cross-section of the failed MP159 probe, from the worn surface (point 1) into the underlying material, at 0.3 mm intervals.

The extremely fine, densely packed equiaxed grains observed in zone (a) (Figure 22a) are consistent with dynamic recrystallisation behaviour directly documented in MP159. Cai, Xiang et al [88] demonstrated that discontinuous dynamic recrystallisation is the dominant recrystallisation mechanism operating in MP159 during hot deformation, and that deformation twins act as preferential nucleation sites for new recrystallised grains, accelerating the process. This is directly consistent with the necklace-type structure inferred in zone (a): new, strain-free grains nucleating at the original grain and twin boundaries and progressively consuming the parent, twinned microstructure. The same study further found that the volume fraction and resulting grain size of the recrystallised material scale with the local deformation temperature and strain rate; higher temperatures and faster straining produce more extensive recrystallisation. Given that zone (a) sits at the sliding contact interface, where interfacial temperature and local strain rate reach their most severe values anywhere in the probe, it follows directly from this established behavior that zone (a) should undergo the most extensive recrystallization of the three zones identified consuming the original twinned structure most completely, and considerably more so than the partially recrystallized transition zone (b) further from the surface. The complete absence of relict annealing twin boundaries in zone (a), together with its markedly finer grain size relative to zone (b), is consistent with this being the most advanced stage of twin-boundary-nucleated dynamic recrystallisation present in the probe.

The elongation superimposed on some of these recrystallised grains (Figure 22b) suggests that this near-surface layer was not a static, fully consolidated microstructure once formed, but continued to experience shear straining under ongoing sliding contact even after new grains had nucleated, consistent with the sustained, cyclic nature of the contact conditions at this interface.

This progressively more complete recrystallisation with proximity to the worn surface directly explains the hardness profile presented in Figure 23. Rather than representing a contradiction of Hall-Petch strengthening, the lowest hardness values recorded at zone (a) are the expected mechanical signature of recrystallisation itself: the process is fundamentally driven by the elimination of stored dislocation energy, and it is the loss of the dislocation- and twin-boundary substructure (not the resulting grain size) that governs the mechanical response. Since recrystallisation is most complete in zone (a), consistent with the temperature/strain-rate dependence established for this alloy [88], the loss of this strengthening substructure is greatest there, producing the lowest hardness on the probe despite its finest grain size. Zone (b), being only partially recrystallised, retains more of the original substructure and consequently records an intermediate hardness, while zone (c), where the coarse, twinned, dislocation-dense base structure remains fully intact, records the highest and most stable hardness values. The hardness gradient across the three zones therefore tracks the degree of recrystallisation completeness with depth, rather than the grain-size gradient itself.

This microstructural and mechanical gradient also provides a direct explanation for the intergranular delamination morphology documented earlier in this chapter (Figure 17 and Figure 18). Both delamination sites exposed a fine, equiaxed, granular fracture surface, with crack paths tracing predominantly along grain boundaries rather than through grain interiors, reproduced independently at two separate locations. This systematic fracture behaviour is precisely what would be expected of the necklace-recrystallised zone (a): the near-complete consumption of the original twinned structure leaves behind a layer that is not only mechanically softened but also densely populated with newly formed, structurally immature grain boundaries lacking the dislocation and twin-related character that would otherwise resist crack propagation. A layer that is simultaneously the softest region on the probe and the site of the highest density of fresh, weakly consolidated boundaries is mechanically primed to fail preferentially along those boundaries once subjected to further cyclic stress, exactly the intergranular fracture path recorded at both delamination sites.

Taken together, the hardness profile, the MP159-specific recrystallization behavior established in the literature, and the delamination fractography converge on a single, internally consistent picture of near-surface degradation. Sustained frictional heating and cyclic shear strain at the worn surface drove discontinuous dynamic recrystallization most extensively in zone (a), progressively less so through the transition zone (b), leaving the bulk material of zone (c) unaffected. This recrystallization produced a softened, structurally weakened near-surface layer, whose abundant fresh grain boundaries offered a low-resistance path for intergranular crack propagation, ultimately manifesting as the surface delamination documented in Figure 17 and Figure 18 . This closes the causal loop proposed throughout this chapter: adhesive wear and frictional heating initiate near-surface recrystallization and softening, and it is this softened, recrystallized layer, rather than the bulk probe material, that is preferentially responsible for the intergranular cracking and delamination that ultimately define the probe's failure.

3.3. Chapter-related claim

Claim No. 1. – On the failure mechanisms in MP 159 probe used in Stationary Shoulder Friction Stir Welding (SS-FSW)

Through in-depth microstructural examination and hardness measurement, I establish the following findings regarding the failure process of an MP159-grade welding probe. The probe was used in the SS-FSW welding of an aluminium alloy under normal operating conditions and failed after reaching its average service life:

The failure of the MP159 SS-FSW probe is not a set of independent surface phenomena but the outcome of a single causal sequence: frictional wear at the sliding interface drives depth-dependent dynamic recrystallisation of the near-surface material, forming a softened, structurally weakened layer whose intergranular cracking and delamination ultimately end the service life of the probe.

This conclusion is supported by the following observations, which together trace the failure from its thermomechanical origin to the terminal loss of material. The intensity of dynamic recrystallisation beneath the worn surface is set directly by the severity of local thermomechanical exposure. Because both temperature and strain rate peak at the sliding contact and decay with depth, the microstructure grades continuously from fully recrystallised at the interface to unaffected in the bulk: an extremely fine, twin-free layer at the surface, a partially transformed region beneath it, and the coarse, twinned parent alloy further still. Discontinuous dynamic recrystallisation nucleates preferentially at original grain and twin boundaries, a mechanism independently confirmed for MP159 under hot deformation. The microstructure, therefore, records the thermomechanical severity experienced at each depth during service. Where this recrystallisation is most complete, the alloy is measurably weakest, because the transformation destroys the dislocation and twin-boundary substructure responsible for the parent material's strength. This loss outweighs any Hall–Petch gain from the accompanying grain refinement. This softened, recrystallised layer is not a passive byproduct of service but the active origin of failure. Its abundance of fresh, immature grain boundaries offers little resistance to intergranular cracking, and the delamination that follows, not the preceding wear, deformation, or cracking, is what removes material and ends the service life. Every other form of surface damage, adhesive wear, plastic smearing, subsurface cracking, alters or weakens the surface but leaves it attached; only delamination detaches material from the probe. The evidence therefore converges on one conclusion: the probe fails not because its surface is worn, but because sustained wear and friction-induced recrystallisation strip the near-surface material of the internal structure needed to resist fracture, and it is this loss, expressed as delamination, that constitutes the true failure event.

Chapter 4: Experimental results: Rebuilding of Stationary Shoulder Friction Stir Welding MP 159 probes by Laser Metal Deposition using Stellite 6 powder

This chapter details the experimental methodology, processing parameters, and metallurgical outcomes of Laser Metal Deposition with Powder for remanufacturing a worn cobalt-nickel-based (MP159) Stationary Shoulder Friction Stir Welding probe. To mitigate high tooling costs and establish a sustainable structural lifecycle, additive manufacturing techniques present a viable path for dimensional restoration.

4.1. Experimental and testing methods

This study focuses on rebuilding the MP159 stationary shoulder Friction Stir Welding probe using the Laser Metal Deposition with Powder process. Both substrates used in this study (Sample 01 and Sample 02) were obtained from the same in-service MP159 probe, which was characterised in Chapter 03. Following removal from service, the failed tip region of the probe, the section exhibiting visible wear and surface damage (Chapter 03, Figure 12) was sectioned off and retained separately for the wear and failure characterisation presented in Chapter 03. The remaining shank material from this same probe was then divided into two separate substrates, used respectively for the two LMDp rebuilding trials (Sample 01 and Sample 02) reported in this chapter. Consequently, the chemical composition of both substrates, presented in Table 3, is identical to that reported for the failed probe in Chapter 03 (Table 2), as both substrates were sectioned from the same parent material. The successful remanufacturing of the SS-FSW tool depends heavily on the effectiveness of the rebuilding phase, which restores degraded areas to their original dimensions. A schematic of the overall remanufacturing process, including the rebuilding stage, is shown in Figure 24. The worn sections of both probes were removed to expose the substrate, after which Stellite 6 powder, a cobalt-based alloy known for its wear resistance, high-temperature strength, and corrosion resistance, was deposited. The chemical composition of Stellite 6 powder is presented in Table 4.

Two distinct LMDp deposition strategies were employed for the experiments. In Sample 1, four layers of Stellite 6 were deposited consecutively on the first substrate, with no cooling intervals between layers. This method allowed for rapid buildup and could lead to increased heat accumulation. In contrast, Sample 2 involved the deposition of six layers of Stellite 6 on the second substrate, with a 10-second cooling interval between each layer. This specific cooling duration was determined from a pre-experiment and is sufficient to cool the material before new deposition while minimising thermal distortion.

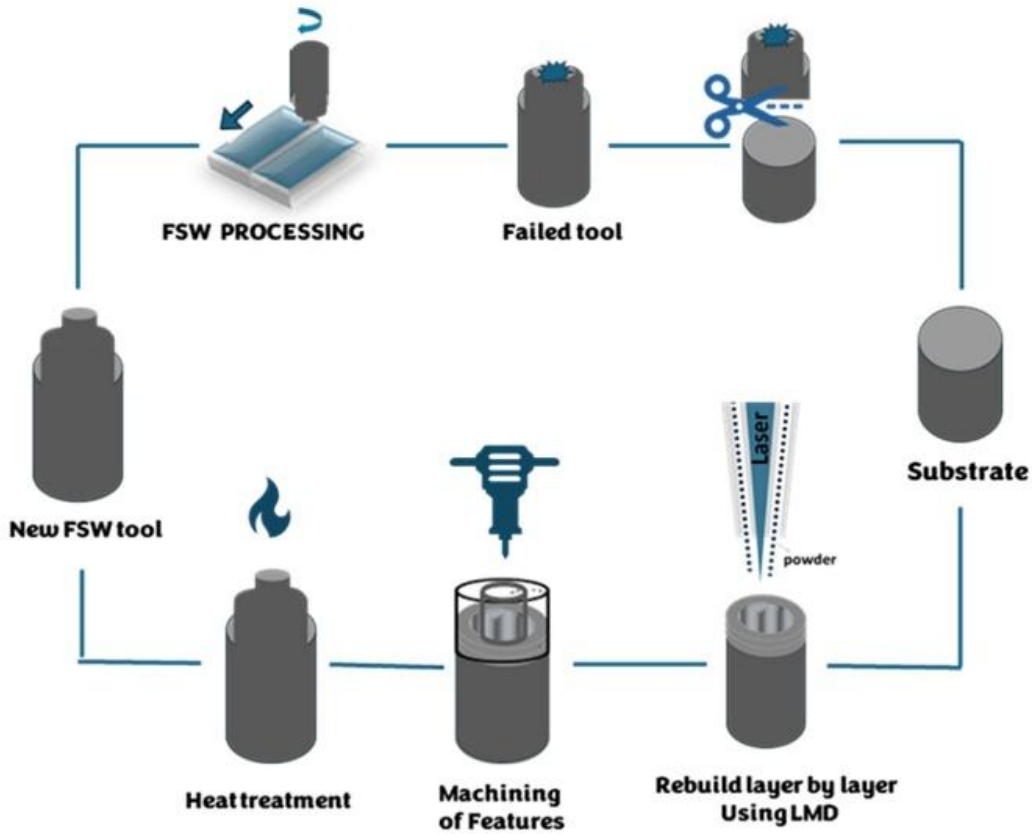

Figure 24. A schematic illustrating the overall remanufacturing process, including the rebuilding stage.

Table 3. Composition of elements of the substrate [87].

Element	Co	Ni	Cr	Fe	Mo	Ti	Nb	Al
Wt %	35.7	25.5	19.0	9.0	7	3	0.6	0.2

Table 4.Composition of elements for Stellite-6 powder [89].

Element	Co	Cr	W	C	Si	Fe	Ni
Wt %	Bal.	28.5	4.4	1.1	1.0	1.5	1.5

Deposition patterns for both samples were designed using AutoCAD and configured in Simplify3D to ensure precise control over layer geometry and thickness, as presented in Figure 25. The samples were fixed in a cooling system, monitored by K Type thermocouple to track temperature variations during the LMDp process, as shown in Figure 26. This setup enabled a comparative assessment of both strategies, focusing on determining which approach was more effective for successfully rebuilding the SS-FSW tool and enhancing its microstructural and mechanical properties. Table 5 presents the parameters utilised in the LMDp deposition technique. Figure 27 visually depicts the LMDp rebuilding on the MP159 substrate.

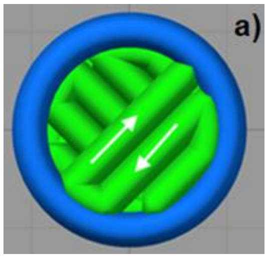

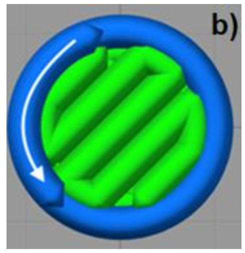

Figure 25. The Deposition patterns are bidirectional with filler: a) inner deposition with 90º rotation for each layer, b) the outer filler.

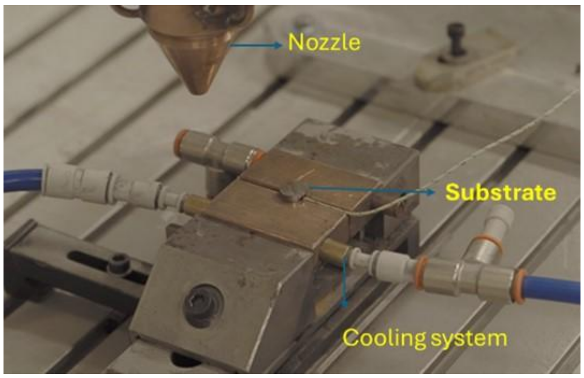

Figure 26. A K-type thermocouple controls the substrate with the cooling stage.

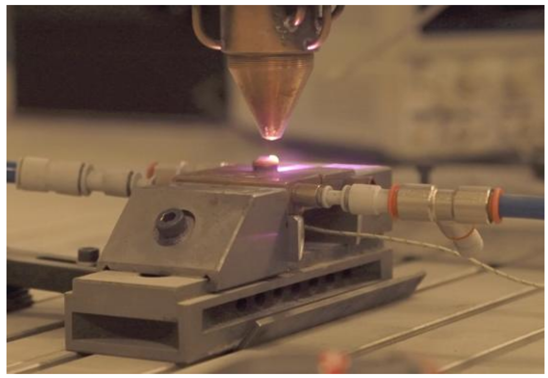

Figure 27. Deposition stage using the LMDp process.

Table 5.LMDp Process parameters.

Laser output (KW)	1.05
Powder size (µm)	20-53
Powder flow rate (g/min	6.9
Carrier gas flow rate (l/min)	5
Shielding gas flow rate (l/min)	10
Focus spot diameter (mm)	2
Deposition Efficiency	>95 %
Standoff distance (mm)	8
Travel speed(mm/s)	15.7

A longitudinal section of the rebuilt substrates was analysed, as illustrated in Figure 28a, both samples were prepared for metallographic examination following standard grinding and polishing procedures. They were then etched using a mixture of 20 ml of nitric acid (HNO3) and 60 ml of hydrochloric acid (HCl) for 5 to 8 seconds. Microscopic examinations were conducted with the Thermo Scientific™ Helios™ G4 PFIB CXe DualBeam™ FIB/SEM scanning electron microscope . Imaging in the SEM was performed utilising both secondary electron and backscattered electron signals, along with energy-dispersive X-ray spectroscopy (EDS) to identify the elemental composition. Additionally, imaging was carried out using the ZEISS SteREO Discovery.V12 microscope. Hardness testing was performed longitudinally using the Wilson Instrument Instron machine with a 3 kg load, and the hardness indentation can be seen in Figure 28b.

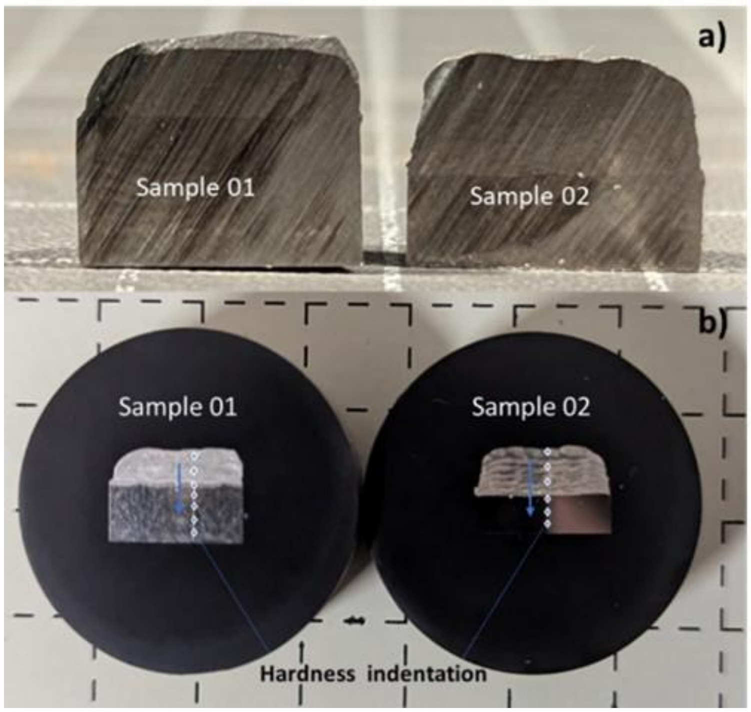

Figure 28. Metallographic preparation of the rebuilt substrates: a) Longitudinal section of rebuilt substrates (Sample 1 and Sample 2), b) the results of the preparation and hardness indentation measurements.

4.2. Results and Discussion

Figure 29 and Figure 30 illustrate the macroscopic images of Samples 1 and 2, respectively. It can be concluded that four layers were successfully deposited on the MP159 substrates of the Stellite 6 alloy for Sample 1, while six layers were deposited for Sample 2. Notably, the deposition in Sample 2 is significantly more homogeneous and geometrically precise compared to Sample 1, despite having a higher number of layers.

The enhanced deposition quality of Sample 2 can be attributed to the cooling applied between each layer during the LMDp process. This controlled cooling helps manage the heat input, resulting in a uniform and successful buildup of each layer.

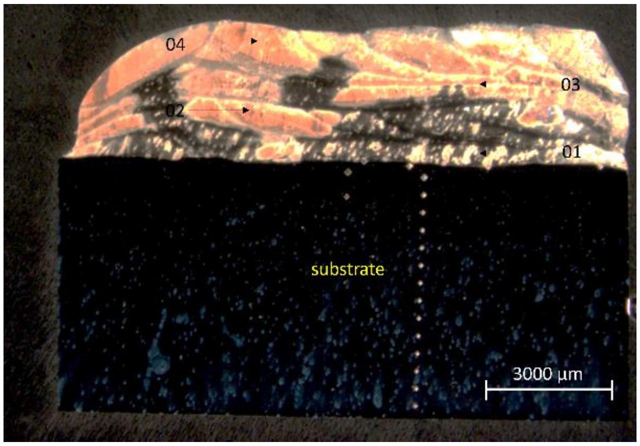

Figure 29. The metallographic preparation results of Sample 1 show the four deposited layers of Stellite 6 on the MP159 substrate.

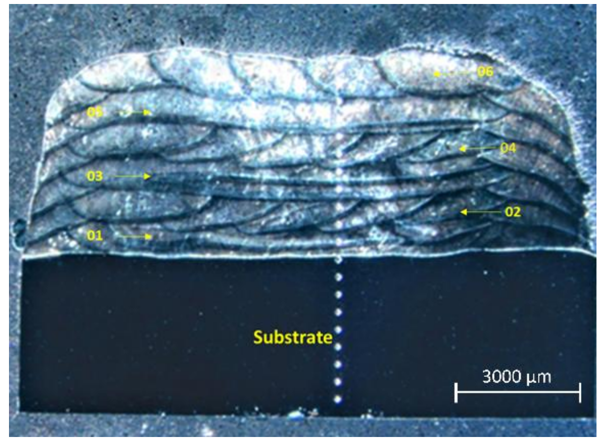

Figure 30. The metallographic preparation results of Sample 2 show the six deposited layers of Stellite 6 on the MP159 substrate.

Figure 31 shows the SEM image of the longitudinal section of the MP159 substrate, which is typical of both samples. It displays an elongated morphology with long twins, suggesting a certain degree of plastic deformation during manufacturing or prior use.

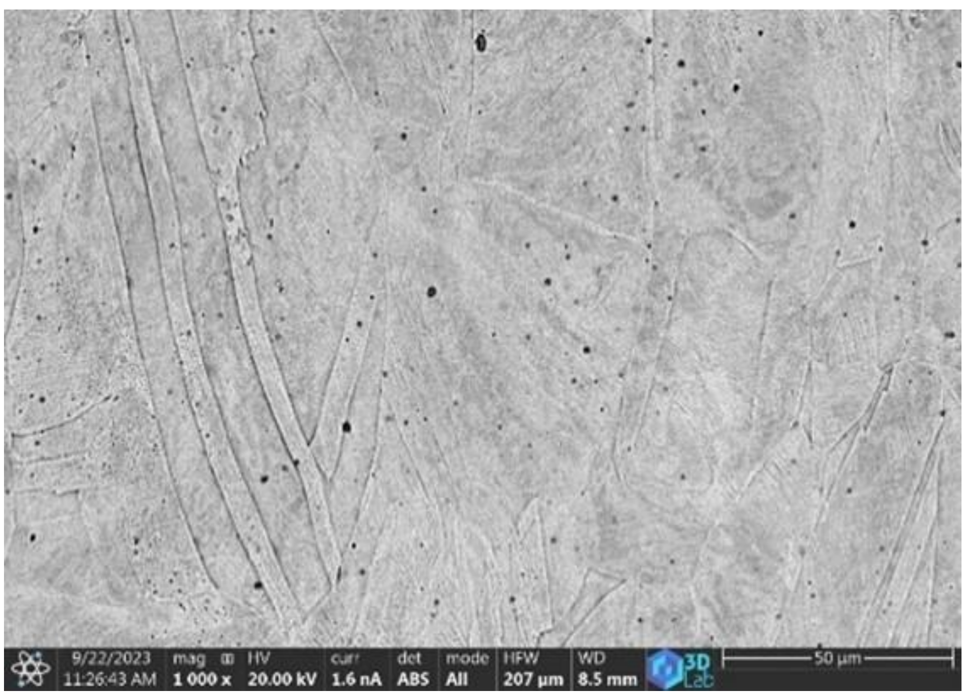

Figure 31. SEM image of the longitudinal section of the based MP159 substrate.

Figure 32 and Figure 33 show the SEM images of the heat-affected zone and the first deposited layer of samples 1 and 2, respectively. Despite the complexity of the structure, the transition between zones is continuous and defect-free.

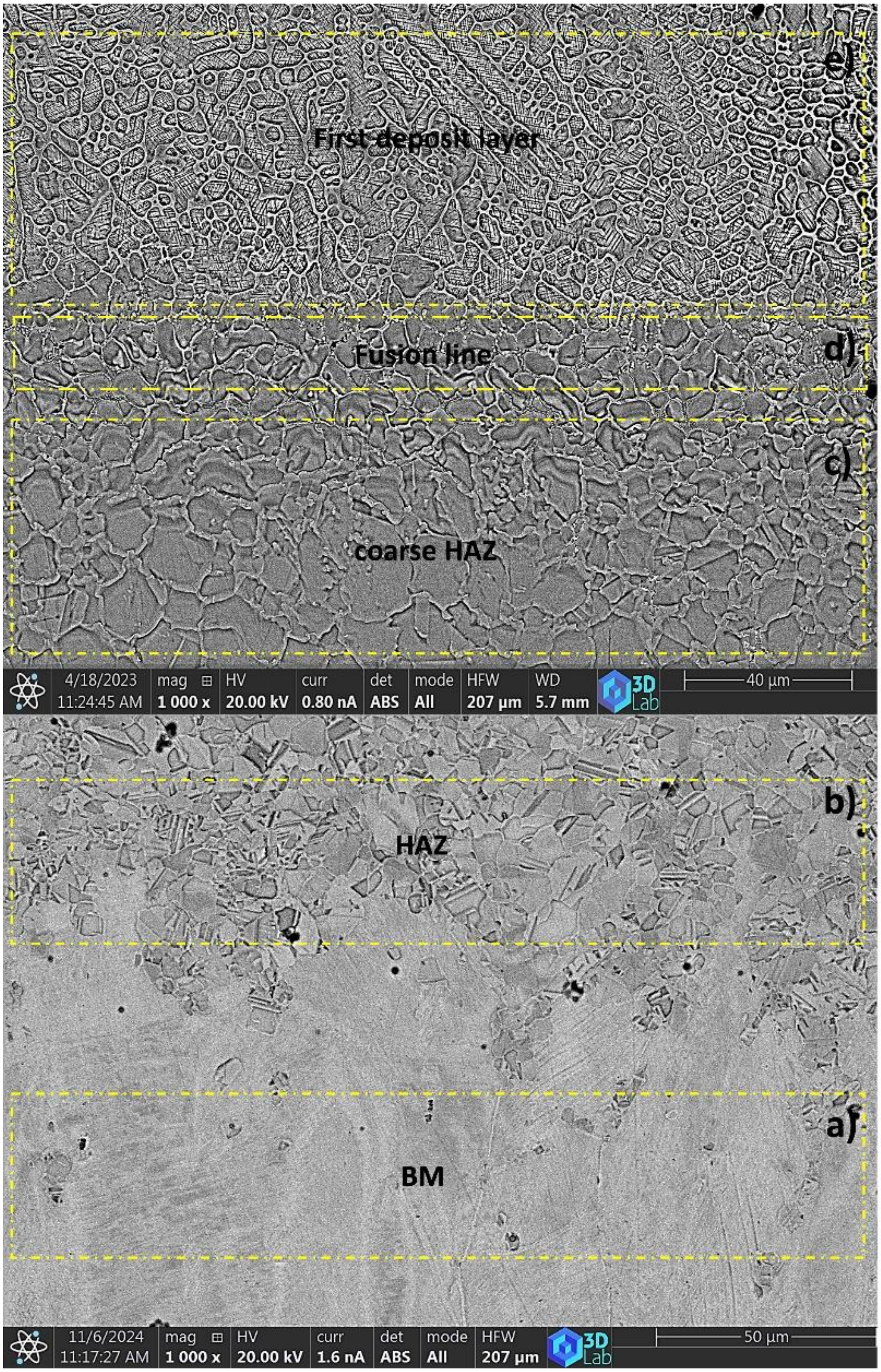

Figure 32. SEM images showing different structures in the substrate of Sample 1 after deposition: (a) Base material with elongated structure, (b) HAZ region with recrystallised structure, (c) Coarser HAZ with recrystallisation, (d) Fusion line between the substrate and deposit, (e) First deposited layer.

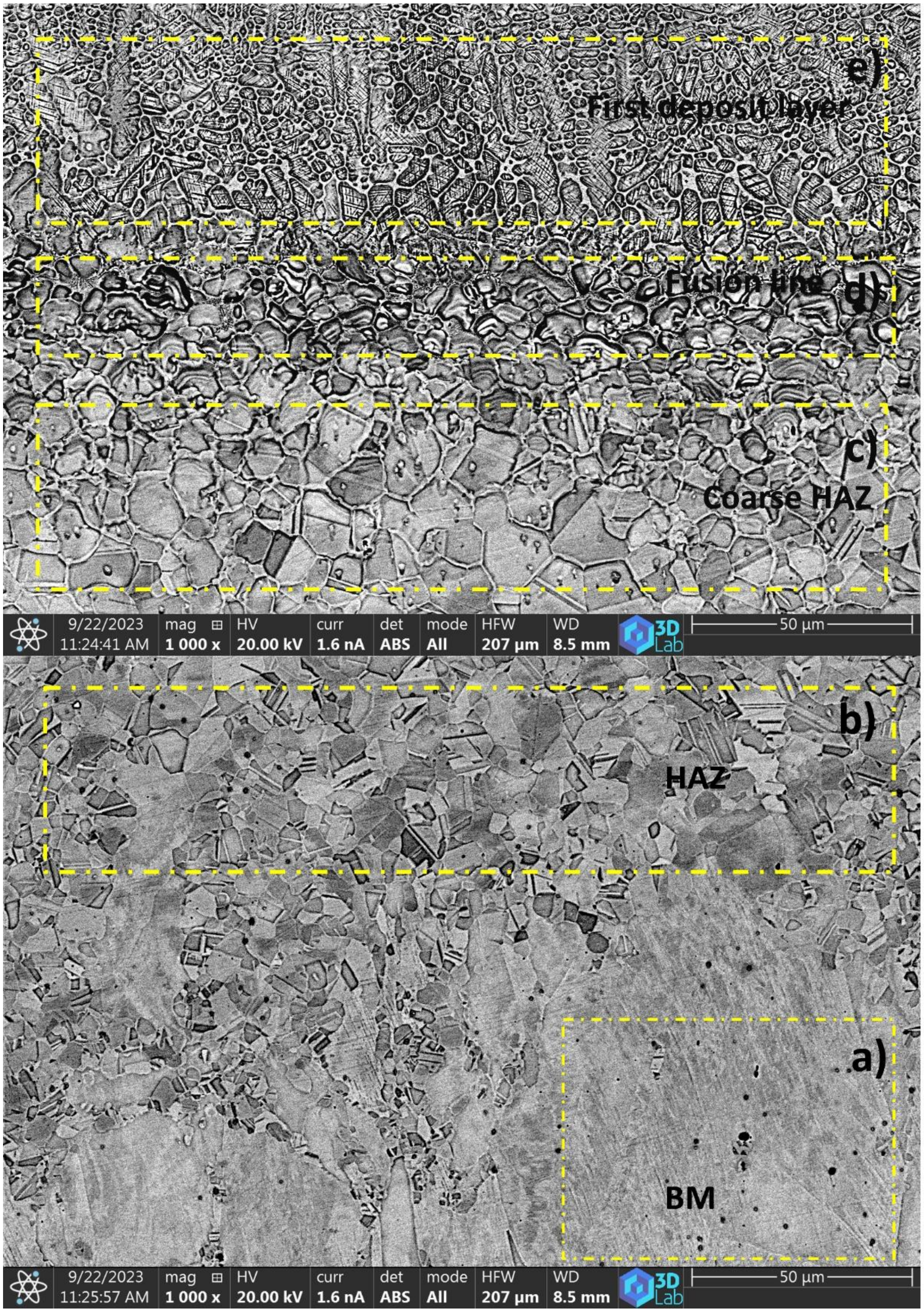

Figure 33. SEM images showing different structures in the substrate of Sample 2 after deposition: a) Base material with elongated structure, b) HAZ region with recrystallized structure, c) Coarser HAZ with recrystallization, d) Fusion line between the substrate and deposit, e) First deposited layer.

The Heat-Affected Zone in the substrate of both samples exhibited a well-defined recrystallisation structure, as shown in (b) part of Figure 32 (Sample 1) and Figure 33 (Sample 2), indicating the influence of tempering during LMDp process.

This recrystallisation is a direct result of the thermal cycling, heating, and cooling periods experienced by the substrate during the LMDp process. Such thermal exposure facilitates the formation of new grains, which replace deformed grains resulting from previous manufacturing operations or service-induced deformation. This observation aligns with prior studies on MP159 superalloy, which reported that static recrystallisation occurs when the alloy is exposed to temperatures above approximately 850–950 C° following prior deformation [90] [91]. The substrate temperatures reached during the LMD-p process, especially near the fusion boundary, are sufficient to activate this mechanism, confirming the thermally induced recrystallised structure observed in both samples.

In Sample 1, the HAZ is deeper than in Sample 2, as shown in Figure 34, despite the greater amount of material deposited in Sample 2. This discrepancy is due to the cooling applied during the deposition of Sample 2, which reduced heat input and limited thermal diffusion, resulting in a narrower HAZ. These effects are consistent with previous LMD and DED investigations showing that interlayer cooling effectively limits substrate temperature rise, minimises residual stress, and reduces HAZ thickness [92], [93].

Noticeable grain coarsening occurs in the HAZ beneath the initially deposited layer (see (c) part of Figure 32 and Figure 33. The recrystallised HAZ presents an average grain size of about 5 μm, but a marked increase to around 16 μm is observed directly below the first deposited layer. This significant coarsening, along with the associated softening of the material, is attributed to the tempering effect induced by the LMD process, which exposes the substrate material to heat during deposition. The observed grain coarsening in the HAZ beneath the first deposited layer (Figure 32c and Figure 33c) is consistent with the findings of J. Xiong et al., who reported similar coarsening behaviour in the HAZ and melt pool interface of Stellite 6 coatings on steel [94].

The (d) parts of Figure 32 (Sample 1) and Figure 33 (Sample 2) depict the interface between the substrate and the first deposited layer. A transition layer approximately 50 microns thick is observed between the coarse HAZ and the first layers in both samples, where the grain size decreases, and the structure is neither characteristic of the substrate nor the layer. Nevertheless, the grains maintain continuity, indicating a continuous transition.

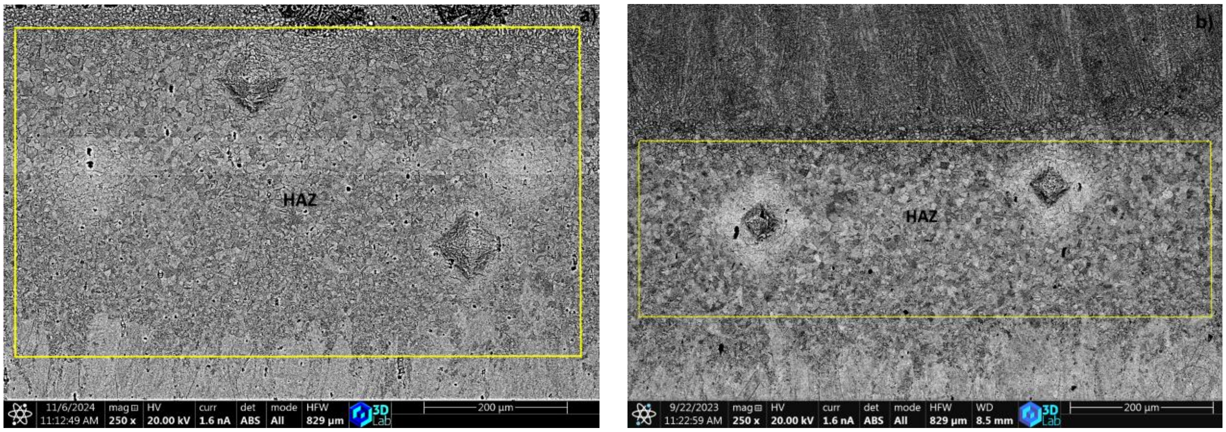

(a) (b)

Figure 34. Comparison of HAZ Depth Between Sample 1 and Sample 2: (a) The HAZ depth in Sample 1. (b) The HAZ depth in Sample 2. The comparison shows that the HAZ in Sample 1 is deeper than in Sample 2.

Figure 35 provides a high-magnification view of the transition layer between the substrates and the first deposited layer (fusion line), emphasizing its microstructural features. The image highlights strong bonding between the substrate and the deposited layer, with a mixed recrystallization structure and lamellar features visible at the grain boundaries. These characteristics are similar to those observed in the deposited layers, underscoring the integrity and continuity of the transition zone.This finding aligns with and is confirmed by Gholipour et al., who showed that laser-clad Stellite 6 coatings formed a metallurgical bond with the steel substrate, free of pores and cracks (clear continuity at the fusion line) and confirmed the lamellar structure at grain boundaries characteristic of Stellite 6. These observations indicate good bonding at the fusion line between Stellite 6 and the MP159 substrate [95].

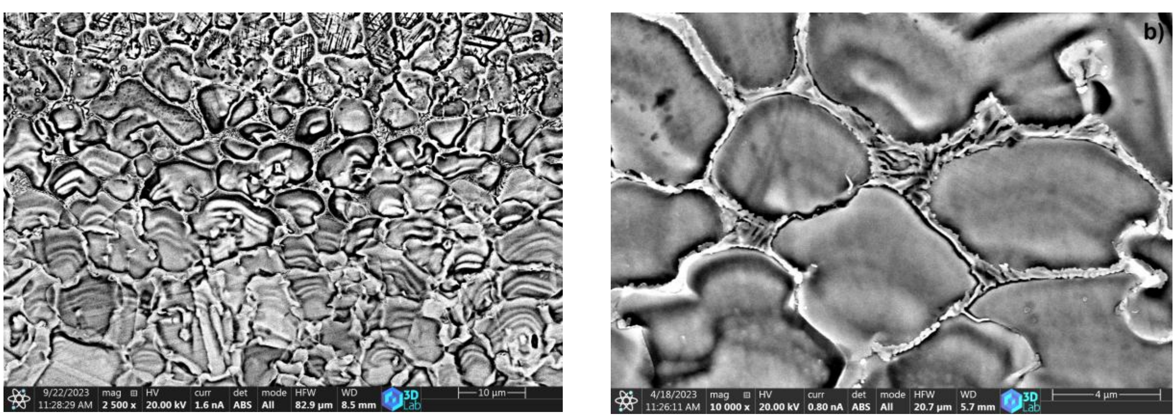

Figure 35. The interface between the substrate and the deposited layer shows strong bonding in both Sample 1 and Sample 2: a) Fusion line in the interface region of Sample 1, b) High-magnification (10,000x) image of the structure at the substrate/deposit interface in Sample 2.

In Figure 36, the EDS mapping analysis shows that the interface between the Stellite 6 deposited layer and the substrate exhibits a lamellar structure with a high concentration of titanium (Ti) and molybdenum (Mo). Since Ti and Mo are present in the substrate's chemical composition but not in Stellite 6, this observation strongly suggests that the interface structure is a result of the partial remelting of the substrate during the deposition process, followed by solidification.

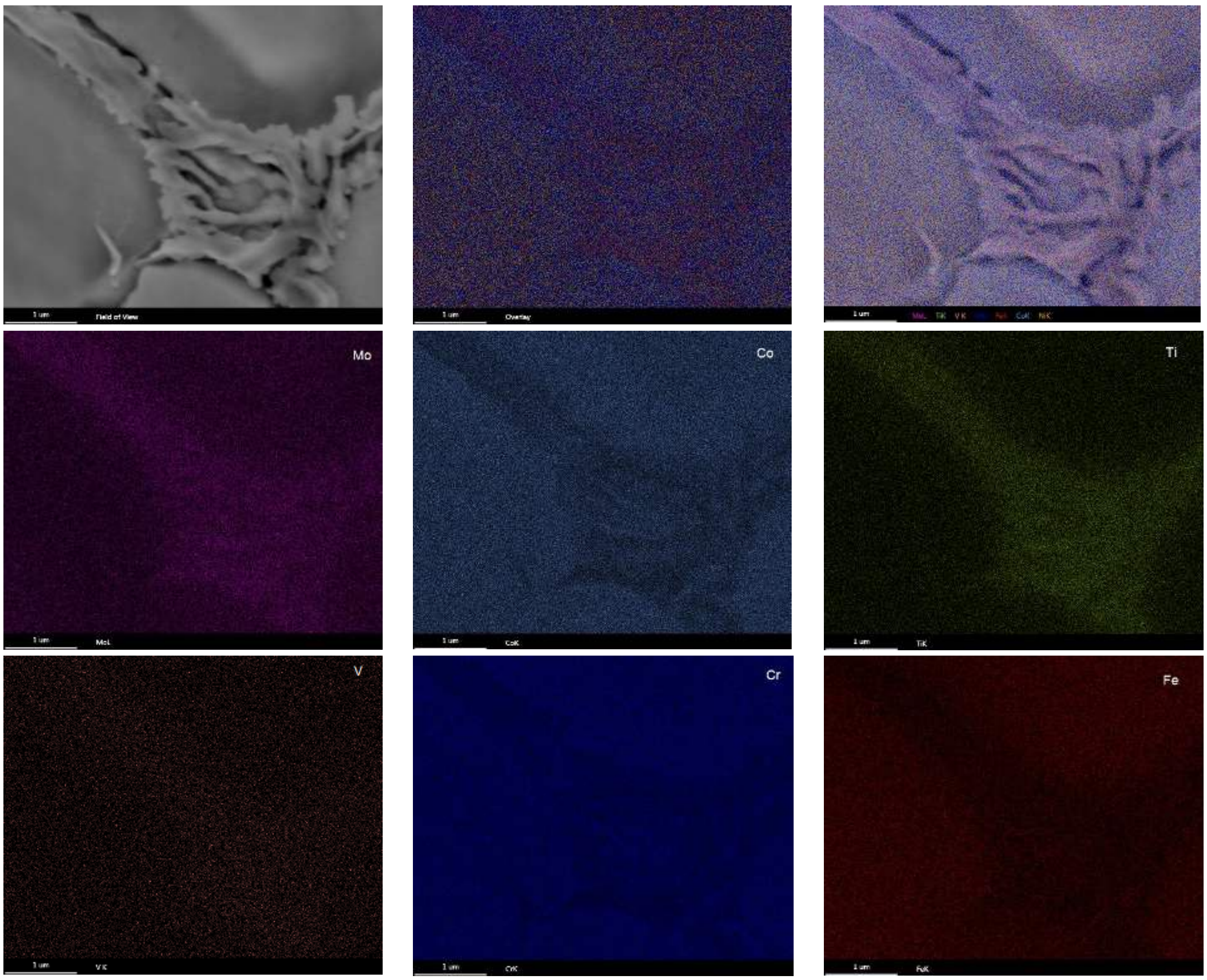

Figure 36. EDS mapping analysis results of the current lamellar structure at the interface of the substrate and deposition region (2 microns in size) show a high concentration of Ti (indicated in green) and Mo (indicated in purple).

Furthermore, the EDS mapping analysis in Figure 37 reveals a well-defined interface between the substrate and the deposition region. This interface is characterised by a mixed zone that indicates strong metallurgical bonding. The elemental distribution highlights differences between the substrate and the deposited layer, showing a gradient at the interface that points to intermixing during deposition. Notably, titanium diffusion, identified as bright blue particles, was observed migrating from the substrate into the deposited layer. This migration not only strengthens the bond but also enhances the mechanical integrity of the composite structure. This diffusion ensures robust adhesion and improves both load-bearing capacity and wear resistance.

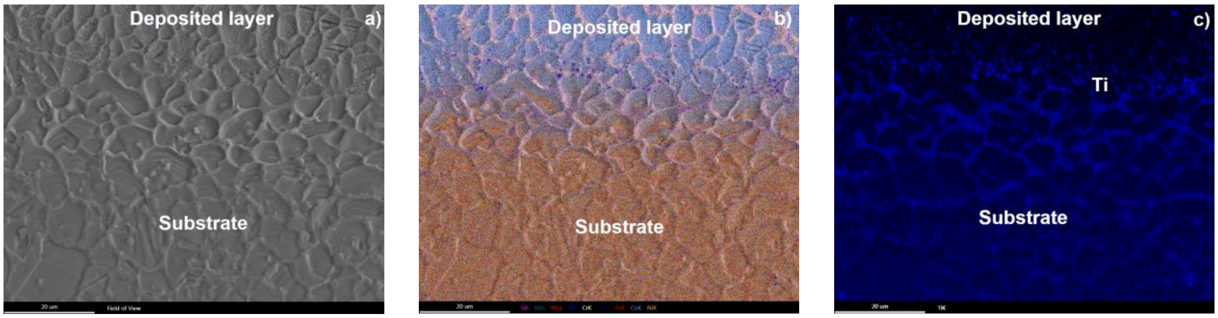

Figure 37. The EDS mapping analysis results are shown as follows: a) the interface between the substrate and the deposition region, b) the distribution of elements, highlighting the differences between the substrate and the deposited layer, where a mixed region at the interface is observed, and c) the diffusion of Ti (represented by bright blue particles) from the substrate into the deposition, indicating the strong bonding.

Figure 38 and Figure 39 show the SEM images of different microstructural features across the Stellite 6 deposition layers in Sample 1 and Sample 2, respectively. In both samples, the deposited layers reveal a typical dendritic structure, which is characteristic of the materials processed through the LMDp method. Notably, a fine dendritic structure is visible within the upper regions of the deposited layers. This is particularly evident in Figure 38a and Figure 39a. Such fine dendrites suggest that these regions experienced a higher cooling rate, facilitating the formation of smaller dendrites and resulting in a more uniform microstructure. This same γ-Co dendrite and lamellar eutectic morphology and its refinement with a higher cooling rate have been reported for laser-clad Stellite-6 [96].

Distinct differences can be observed between the two samples at the fusion line within the deposition interface region. In Sample 1, the microstructure reveals an indistinct interface, likely due to heat accumulation and partial remelting, resulting in blurred interfacial features, as shown in Figure 38e [97]. In contrast, Sample 2 displays a well-defined interdentritic space at the interface (Figure 39e), indicating better thermal control and effective cooling. This allowed for precise solidification and preserved structural clarity at the deposition boundary [98].This interpretation is in line with process-level studies showing that inter-layer cooling time is a strong lever on the thermal history in DED and improves interface quality by limiting remelting-driven mixing [99].

Additionally, a bright particle is present in this region. Beyond the interface, grain coarsening in the HAZ of the deposited layers is evident. The grain size in the middle region of the deposited layer measures approximately 8 microns (Figure 38d and Figure 39d), increasing to about 16 microns in the HAZ (see Figure 38f and Figure 39f); this coarsening is attributed to the slower cooling in this region.

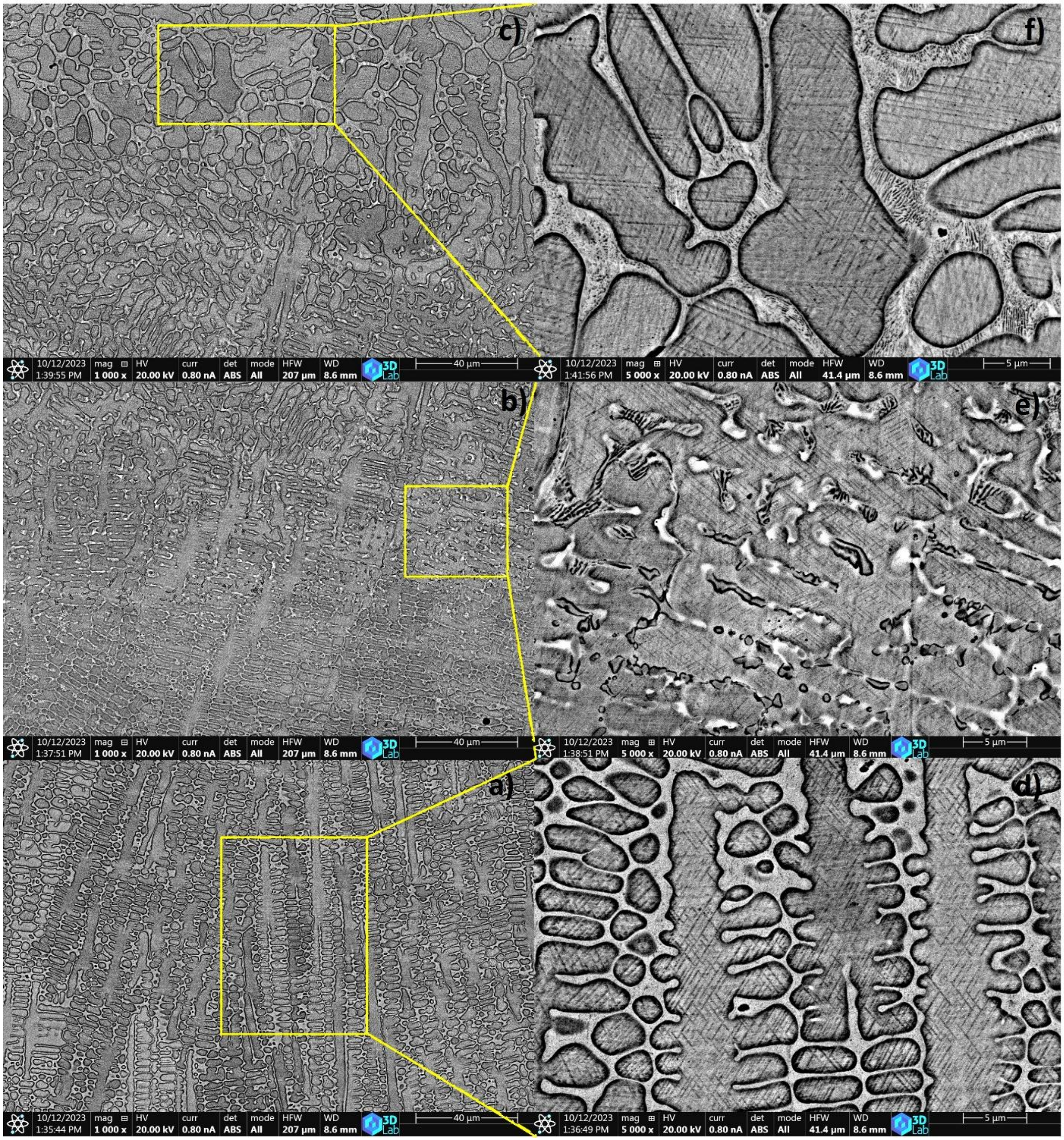

Figure 38. SEM images of different microstructural features across the Stellite 6 deposition layers in sample 1: a) the upper region of the deposition, b) the interface between the previous and next deposited layer, and c) the Middle region of the deposited layer (HAZ). Images d), e), and f) provide higher magnification views of regions a), b), and c), respectively.

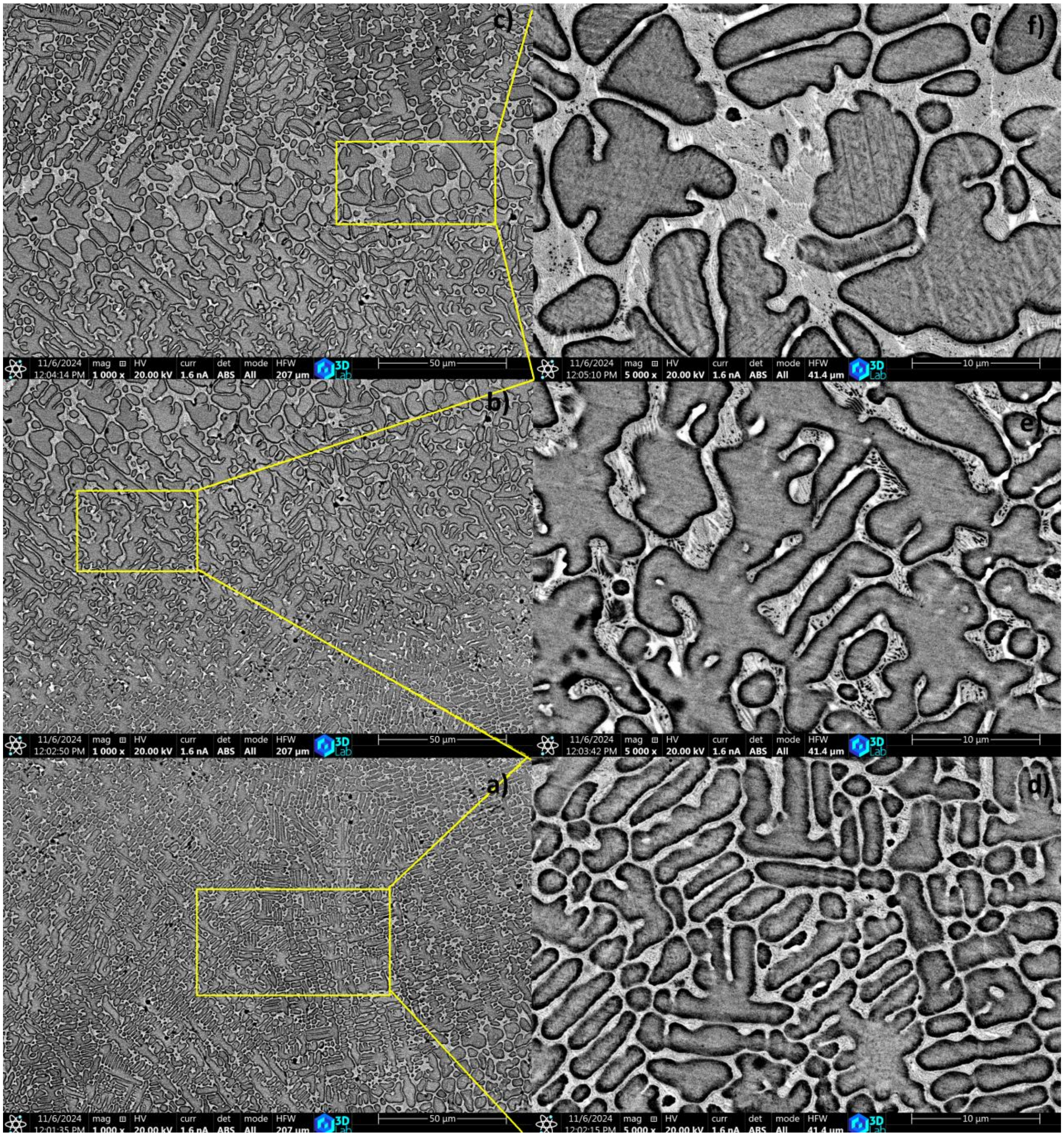

Figure 39. SEM images of different microstructural features across the Stellite 6 deposition layers in sample 2: a) the upper region of the deposition, b) the Interface between the previous and next deposited layer, and c) the Middle region of the deposited layer (HAZ). Images d), e), and f) provide higher magnification views of regions a), b), and c), respectively.

Figure 40 illustrates the difference in the Heat Affected Zone between Samples 1 and 2 in the deposited layer. Sample 1 exhibits a larger HAZ with a depth of approximately 80 microns, while Sample 2 shows a thinner HAZ, measuring around 30 microns. This disparity can be attributed to the cooling applied during the deposition process in Sample 2. The cooling system likely reduced the heat input and accelerated the cooling rate, thereby limiting the thermal diffusion and the extent of the HAZ. In contrast, Sample 1, without cooling, experienced prolonged thermal exposure, resulting in a deeper HAZ.

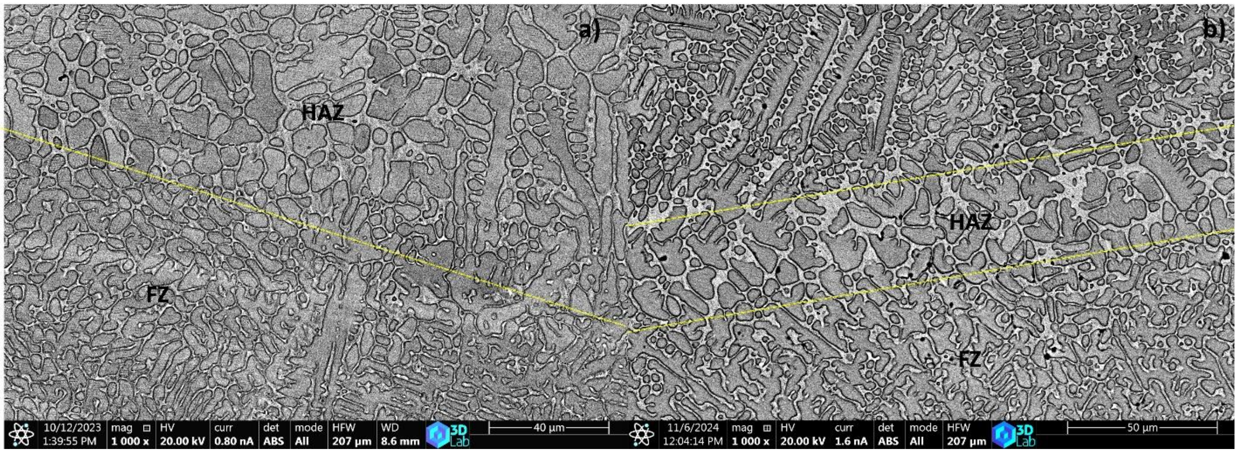

Figure 40. Comparison of the Heat Affected Zone (HAZ) in both samples: sample 1 shows a larger HAZ with a depth of up to 80 microns, and b) sample 2 has a thinner HAZ measuring about 30 microns.

In Figure 41 EDS mapping analysis of the Stellite 6 deposition shows a high Co concentration in the dendrite core and a high Cr concentration in the interdendritic regions, which is typical of the Stellite 6 alloy.

The EDS results (Figure 42) for the bright particles in the HAZ show a high Co signal because the SEM-EDS interaction volume samples the surrounding γ-Co matrix; relative to the adjacent dendrite, the particle is enriched in Cr and W, identifying it as a Cr–W rich interdendritic carbide rather than a Co phase. Such Cr-W rich interdendritic carbides are well- established constituents of laser-clad Stellite-6, repeatedly reported across the literature [100] [101].

Figure 43 presents the Vickers microhardness across the deposited layers (Dep01–Dep06), the heat-affected zone, and the base metal for Sample 1 and Sample 2. The deposited Stellite-6 layers in both builds form a near-flat plateau of 500–550 HV. This hardness range is consistent with the standard microstructure of laser-processed Stellite-6 Co- rich γ matrix with interdendritic Cr-rich [102]. In both samples, there is a noticeable decrease in the hardness of the heat-affected of the substrate (300 HV). This reduction in hardness mainly results from recrystallisation softening.

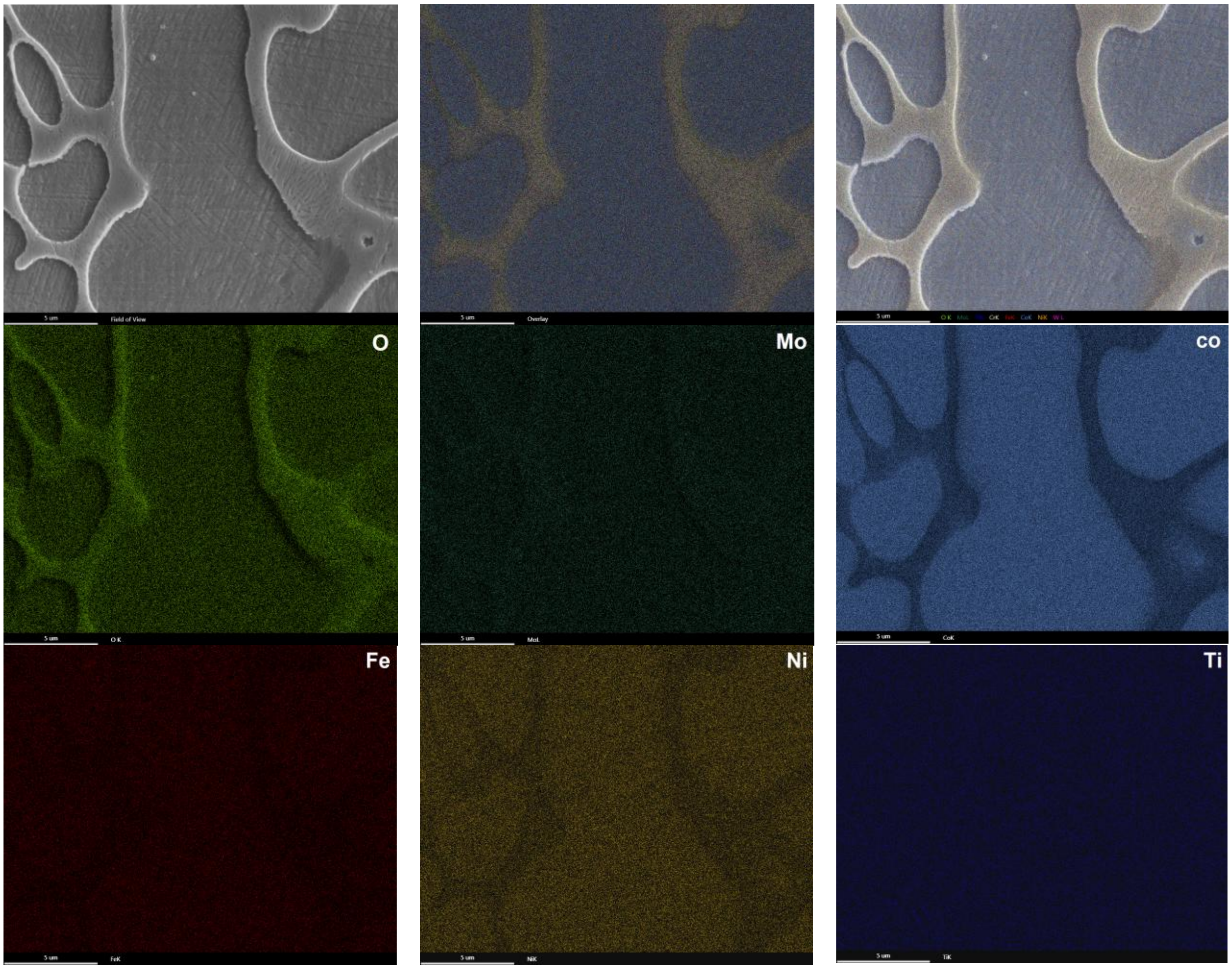

Figure 41. EDS mapping analysis of the stellite 6 deposition shows high Co concentration in the dendrite core and high Cr concentration in the interdendritic regions.

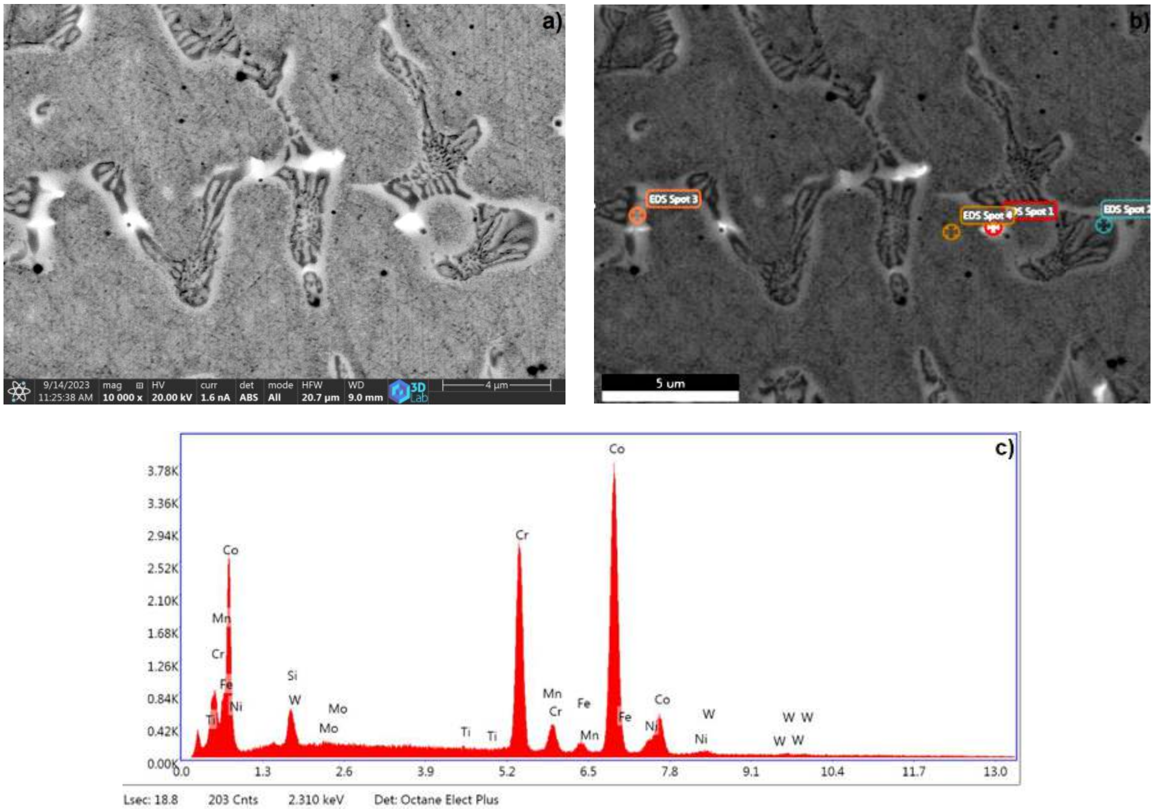

Figure 42. EDS results analysis in the HAZ of the deposited Stellite6 layer. a) the presence of the bright phase in the interdendritic space, b) the bright phases indicated as spot4, and c) the EDS diffractogram shows that bright phases have a high cobalt concentration.

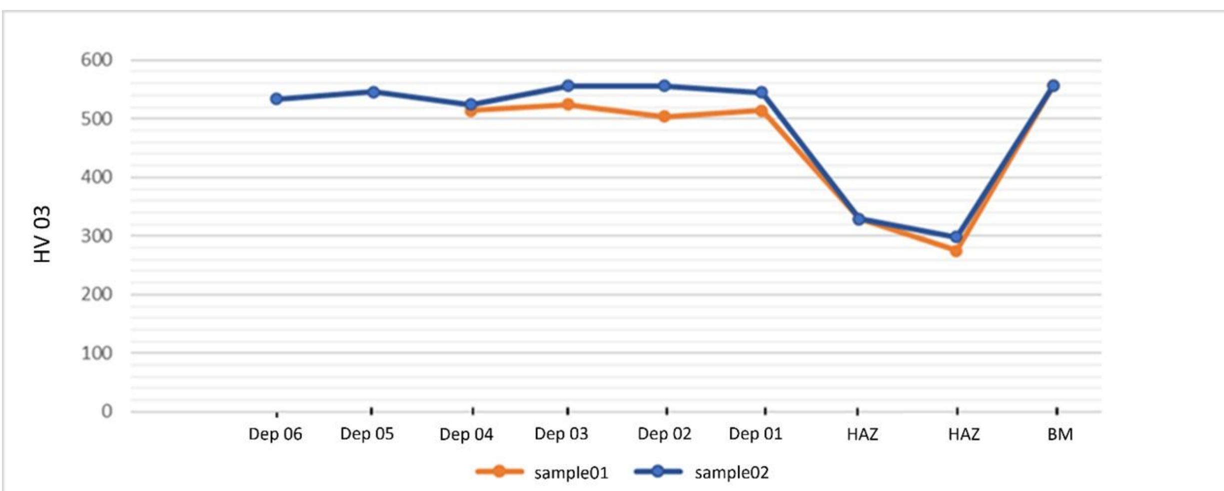

Figure 43. Microhardness results of samples 1 and 2 across the base material, HAZ, and deposited layers.

During laser deposition, the thermal exposure caused the elongated, deformation-twinned grains in the MP159 substrate to transform into strain-free, equiaxed grains, thereby eliminating the dislocations and twin strengthening. Prolonged exposure to elevated temperatures led to grain coarsening, reducing grain boundary density and further decreasing hardness. The small difference between Sample 1 and Sample 2 indicates that inter-layer cooling chiefly improved thermal stability and interface quality (as seen in Figure 38 and Figure 39) but did not materially shift the clad-zone hardness, which is governed primarily by composition and the rapid-solidification microstructure. Finally, the absolute hardness levels measured fit within the published range for Stellite-6 clads [103], [104]. The softening of the heat-affected zone can be considered an advantage in friction stir welding, as it plays a key role in enhancing tool performance and durability. Acting as a ductile buffer between the Stellite 6 layer and the MP159 substrate, the softened HAZ helps absorb and redistribute the high stresses caused by tool rotation and axial plunging. This is particularly useful in managing shear stresses due to differences in the Coefficient of Thermal Expansion (CTE) between the two materials. Rather than being a weakness, the softened HAZ improves tool reliability by relieving residual stress, accommodating thermal mismatches, and preventing crack initiation. It reduces the risk of failure modes such as delamination and fatigue while minimising localised wear. As a result, the tool gains improved structural integrity and a longer service life under demanding FSW conditions. This interpretation is consistent with the observations of Pisarski et al., who reported that strain localises within softened HAZ of overmatched welds in high-strength steels. Their work demonstrates that a moderately softened HAZ can accommodate deformation mismatch between dissimilar regions, thereby relieving local stresses [105].

4.3. Financial justification and environmental considerations of production and remanufacturing

The financial justification for using LMDp in remanufacturing is primarily driven by its cost-saving potential compared to the production of new tools. Numerous studies have demonstrated that LMDp remanufacturing can reduce costs by 30% to 60%, depending on the industry and application. For instance, the remanufacture of hot forging dies using LMDp has been shown to achieve cost savings of up to 50%, reducing downtime and extending tool life by restoring worn areas instead of producing entirely new tools [106]. Similarly, using Stellite 21 in die remanufacturing has cut costs by more than 50%, offering an economically viable alternative to traditional tool replacement [107]. Applying LMDp cladding reduces costs by around 40% compared to traditional repair or replacement methods. Table 6 presents the assumed and final calculated costs for remanufacturing a worn probe using LMDp. The results highlight the significant reduction in total expenses, supporting the economic viability of the process compared to replacement.

Table 6. The assumed costs and final calculated costs for remanufacturing a worn probe by LMDp.

cost Component	High-Cost Scenario (USD)	Moderate-Cost Scenario (USD)	Low-Cost Scenario (USD)
Pre-repair Machining	$5.00	$5.00	$5.00
Post-repair Machining	$33.3	$33.3	$33.3
LMD Process	$66.67	$33.33	$16.67
Operator Cost	$3.33	$3.33	$3.33
Consumable (Stellite 6)	$15.00	$15.00	$15.00
Heat Treatment	$14.00	$14.00	$14.00
Total Cost	$137.33	$103.99	$87.33
Savings (Compared to $198 New Tool)	$60.67	$94.01	$110.67
Percentage Savings	31%	47%	56%

Table 7 provides a detailed breakdown of the various cost components involved in the LMDp remanufacturing process. It outlines how each cost is calculated and its contribution to the overall expenses. The table includes costs such as machine operation (LMD process), operator involvement, material usage (Stellite 6 powder), and machining tasks performed before and after the repair.

Table 7. Detailed Cost Components and Calculations.

Cost Component	Calculation	Cost (USD)
LMD Process Cost	High Cost: $200/hour × (1/3 hour)	$66.67
	Moderate Cost: $100/hour × (1/3 hour)	$33.33
	Low Cost: $50/hour × (1/3 hour)	$16.67
Operator Cost	$100/hour × (1/3) × 10%	$3.33
Consumable Cost (Stellite 6)	Fixed Cost per Tool	$15.00
Pre-repair Machining	Fixed Cost for Removing Worn Areas	$5.00
Post-repair Machining	Fixed Cost to Restore Tool Geometry	$33.33

LMDp remanufacturing provides significant economic advantages and aligns with sustainability objectives by minimizing environmental impacts. The process reduces raw material usage by repairing worn tool sections instead of manufacturing new tools, cutting the demand for energy-intensive alloys like MP159, which require Vacuum Induction Melting (VIM) and Vacuum Arc Remelting (VAR). By focusing on selective repair, LMDp substantially reduces waste, conserving up to 90% of the original tool and aligning with circular economy principles. Additionally, it is energy-efficient, as it circumvents high-temperature smelting and alloy production, leading to lower energy consumption and greenhouse gas emissions. By extending tool life and conserving resources, LMDp not only reduces the frequency of tool production but also avoids environmental impacts associated with the logistics of acquiring new components, making it a compelling choice for industries aiming to enhance sustainability while achieving cost efficiencies.

4.4. Chapter-related claim

Claim No2. – On the remanufacturing of a worn cobalt-nickel-based (MP159) Stationary Shoulder Friction Stir Welding probe

Through in-depth microstructural examination and hardness measurements, I establish the following findings regarding the success of the repair process for an MP159-grade welding probe that failed after an average service life of SS-FSW welding of aluminium alloys. The dimensional restoration was performed using additive manufacturing techniques, specifically Laser Metal Deposition, with Stellite 6 powder:

(a) Laser Metal Deposition with Powder (LMDp) is a metallurgically sound method for rebuilding worn MP159 SS-FSW probes with Stellite 6, because the process produces a strong, defect-free deposit whose microstructure bonds reliably to the substrate.

This conclusion is supported by the following observations, which establish both the integrity of the bond and the role of the softened substrate zone beneath it. The Stellite 6 deposits form a strong metallurgical bond with the MP159 substrate, with defect-free layers, a well-developed dendritic microstructure, and consistent hardness throughout the deposited material. Together, these demonstrate that the rebuild is structurally sound rather than merely adhered. The process induces a softened heat-affected zone in the substrate through localised thermal exposure during deposition, but microstructural analysis shows that this region retains a sound metallurgical bond with the deposit and does not compromise the interface integrity. Rather than a defect, the gradual hardness transition across the softened HAZ acts as a ductile transition layer that relieves stress concentration at the interface and may itself enhance the durability of the remanufactured probe.

(b) Introducing a controlled cooling interval between deposited layers improves the quality and durability of the rebuilt probe, making it a key process parameter rather than an optional refinement.

This conclusion is supported by the following observations, which link the cooling interval to measurable improvements in the deposit and the substrate beneath it. Compared with continuous deposition, a 10-second cooling interval between layers significantly reduces the depth of the heat-affected zone in the substrate, minimises thermal distortion, and improves layer uniformity. By limiting the accumulated thermal load, controlled cooling directly constrains the extent of the softened HAZ and yields a more uniform deposit, establishing it as a decisive lever for both LMDp quality and tool durability.

(c) Remanufacturing MP159 SS-FSW probes by LMDp is economically and environmentally advantageous compared with producing new tools because it restores only the worn section rather than replacing the entire probe.

This conclusion is supported by the following observations, which quantify the economic savings and the environmental benefit of repair over replacement. Repairing the worn region alone achieves 31–56% lower production costs than manufacturing a new probe, with corresponding reductions in material and energy use. Environmentally, the approach preserves roughly 90% of the original material, cuts industrial waste and CO_2 emissions, and aligns with sustainable manufacturing principles.

Chapter 5: Experimental results: Physical simulation of thermal and mechanical transients on H13 tool steel during the plunge stage of friction stir welding

Characterising the performance limits and degradation modes of materials under severe thermo-mechanical conditions requires a systematic experimental approach that combines raw material validation, heat-treatment processing, and controlled physical simulation. During friction stir welding, the tool is exposed to complex, highly transient thermal and mechanical fields that are extremely difficult to isolate and measure directly in real time on an industrial welding machine. Therefore, to evaluate how specific variables independently drive structural degradation and failure, physical testing methods must be deployed to replicate industrial process environments inside a highly controlled laboratory setting.

This chapter establishes the complete experimental framework and procedural methodology utilised throughout this research. The baseline focus centres on establishing the chemical, metallurgical, and mechanical initial state of hot-work tool steels used as the standard reference tool material. Following composition verification, precise heat-treatment parameters are detailed to establish the baseline structural microstructures required to withstand elevated-temperature processing.

5.1. Experimental and testing methods

TWI Ltd supplied the industrial H13 steel friction stir welding tool used as the reference material for this investigation (see Figure 44). To ensure that the Gleeble simulations accurately represented the behaviour of the actual tool, the test specimens were machined from an H13 alloy with a composition closely matching that of the tool. The concentrations of the primary alloying elements for both materials are presented in Table 8, confirming that the specimens and tool fall within the same chemical range.

Before machining, the H13 material was subjected to the standard hardening heat treatment typical of FSW tool manufacturing. The heat treatment consisted of austenitisation at 1050 °C, quenching, and double tempering at 550–600 °C, producing a tempered martensitic microstructure with high thermal stability and resistance to softening at elevated temperatures. After heat treatment, cylindrical Gleeble specimens were machined to final dimensions of 10 mm diameter × 100 mm length, ensuring uniform current flow during resistance heating and stable gripping during mechanical testing.

To replicate the transient conditions experienced during the plunge stage of FSW, both thermal and mechanical simulations were conducted using a Gleeble 3000 thermo-mechanical simulator (see Figure 45).

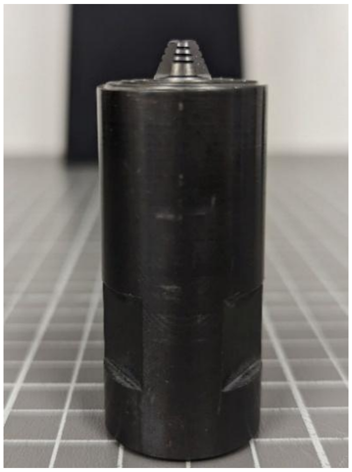

Figure 44. H13 steel FSW tool.

Table 8. Concentration of main alloying elements of FSW tool and Gleeble samples.

	Main alloying elements, wt%						
	C	**Si**	**Mo**	**V**	**Cr**	**Mn**	**Fe**
FSW tool	0.32-0.45	1.43	1.86	1.21	5.41	0.64	89.44
Gleeble sample	0.32-0.45	1.17	1.58	1.15	5.30	0.60	90.2

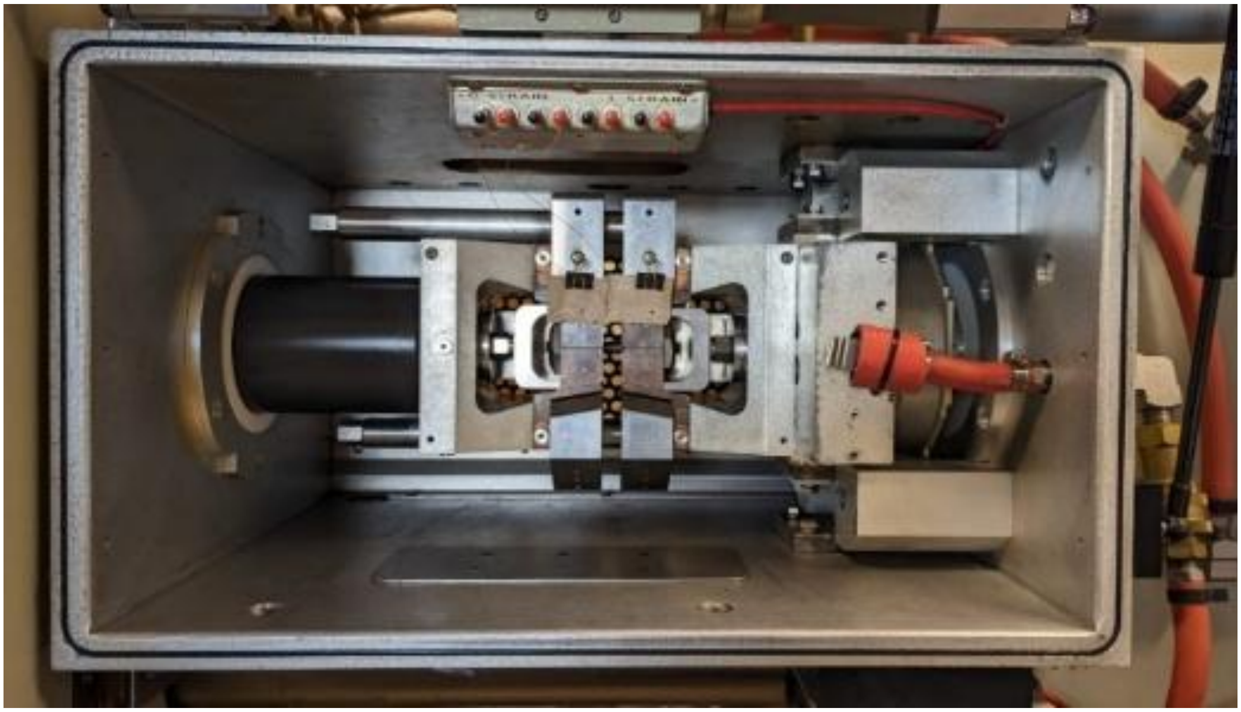

Figure 45. Testing chamber of the Gleeble physical simulator 300 machine.

5.1.1. Thermal Simulation Procedure

Thermal simulations were conducted to replicate the transient temperature history experienced by the tool during the plunge stage of FSW, characterised by a steep temperature increase from room temperature to above 600 °C within seconds, as illustrated by the temperature variation in the tool pin shown in Figure 46. This rapid thermal transition generates intense thermal transients that can impact tool performance and material behaviour. To simulate these conditions, two thermal cycling tests were performed using the Gleeble 300 thermo-mechanical simulator, with thermal parameters set to a temperature range of 100°C to 620°C, a heating rate of 500°C/s, and a cooling rate of 8°C/s.

The first simulation involved 40 thermal cycles, and the second extended to 80 cycles. The thermal profiles are shown in Figure 47-a) and Figure 47-b), respectively. The simulation sample was formed into a cylindrical piece with dimensions of 10 mm in diameter × 100 mm in length, as shown in Figure 48 .

Following the thermal cycling, the samples were subjected to room-temperature tensile testing to evaluate the mechanical degradation induced by thermal exposure using the Instron universal test machine.

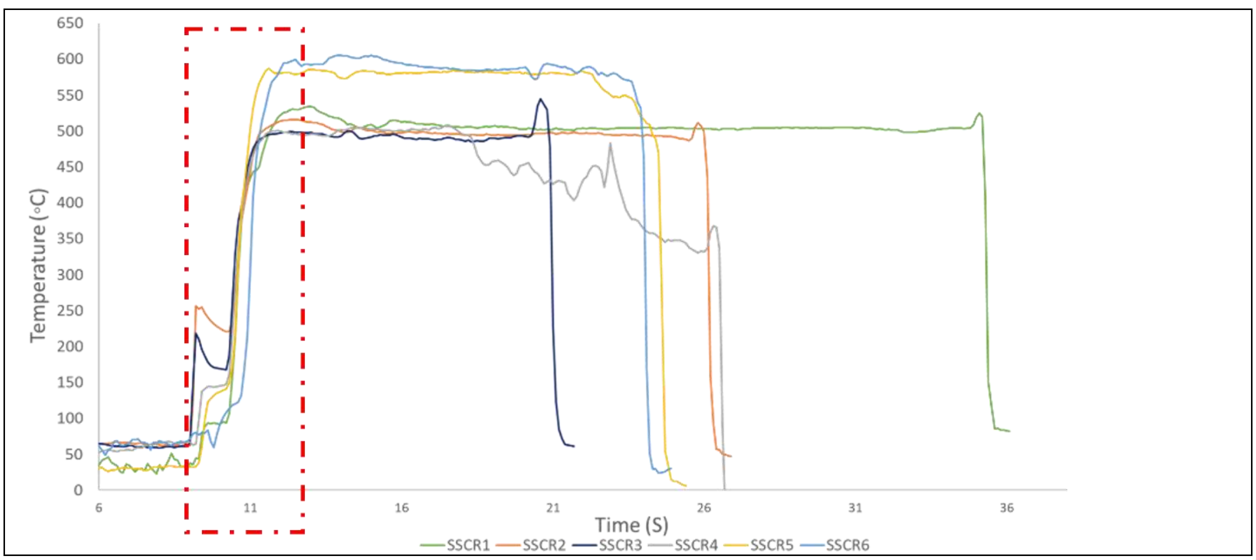

Figure 46. Temperature evolution at the tool pin during friction stir welding of aluminium, illustrating the rapid temperature rise during the plunge stage (highlighted region) followed by a transition to a steady-state thermal plateau during welding. SSCR1, SSCR2, SSCR3, SSCR4, SSCR5, and SSCR6 correspond to different recorded temperature profiles from separate FSW trials.

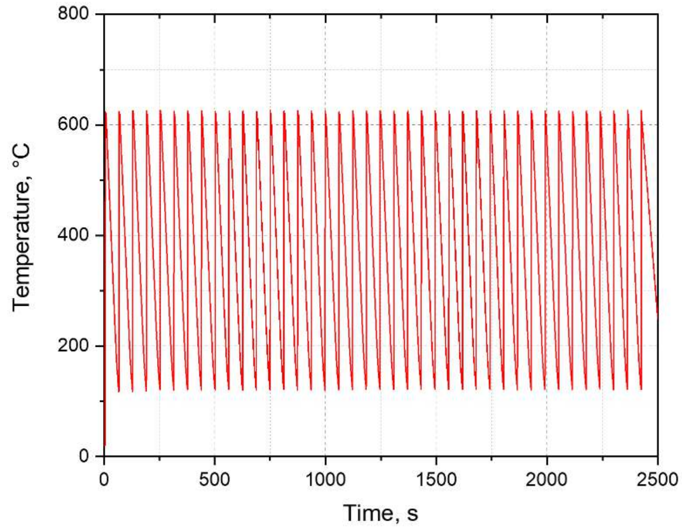

a)

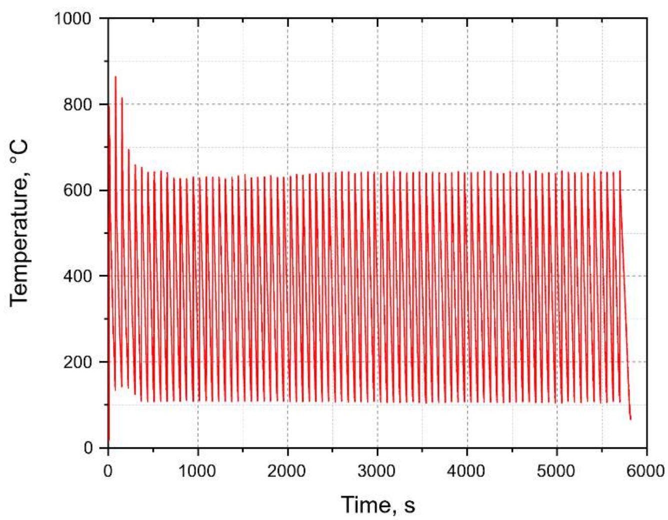

b)

Figure 47. Thermal simulation cycles: a) 40 repetitions, b) 80 repetitions.

Figure 48. Sample of the thermal simulation.

5.1.2. Mechanical Simulation Procedure

To simulate the mechanical transients occurring during the plunge phase, samples were heated to 620 °C, subjected to tensile testing at four strain rates (2.54, 25.4, 254, and 1016 s-1), and fractured using the Gleeble machine. These tests were designed to replicate the mechanical transient tool faces during initial penetration into the cold workpiece. The sample geometry for this test is presented in Figure 49 and fractured specimens after testing are shown in Figure 50 .

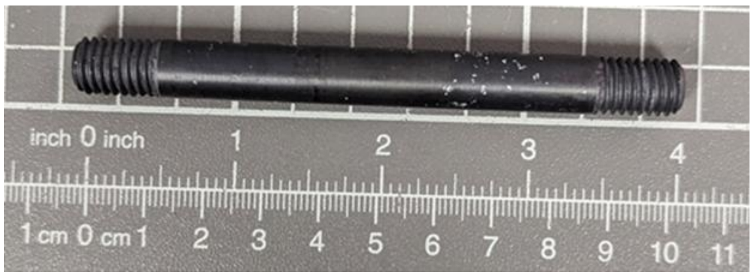

Figure 49. Sample of the mechanical simulation.

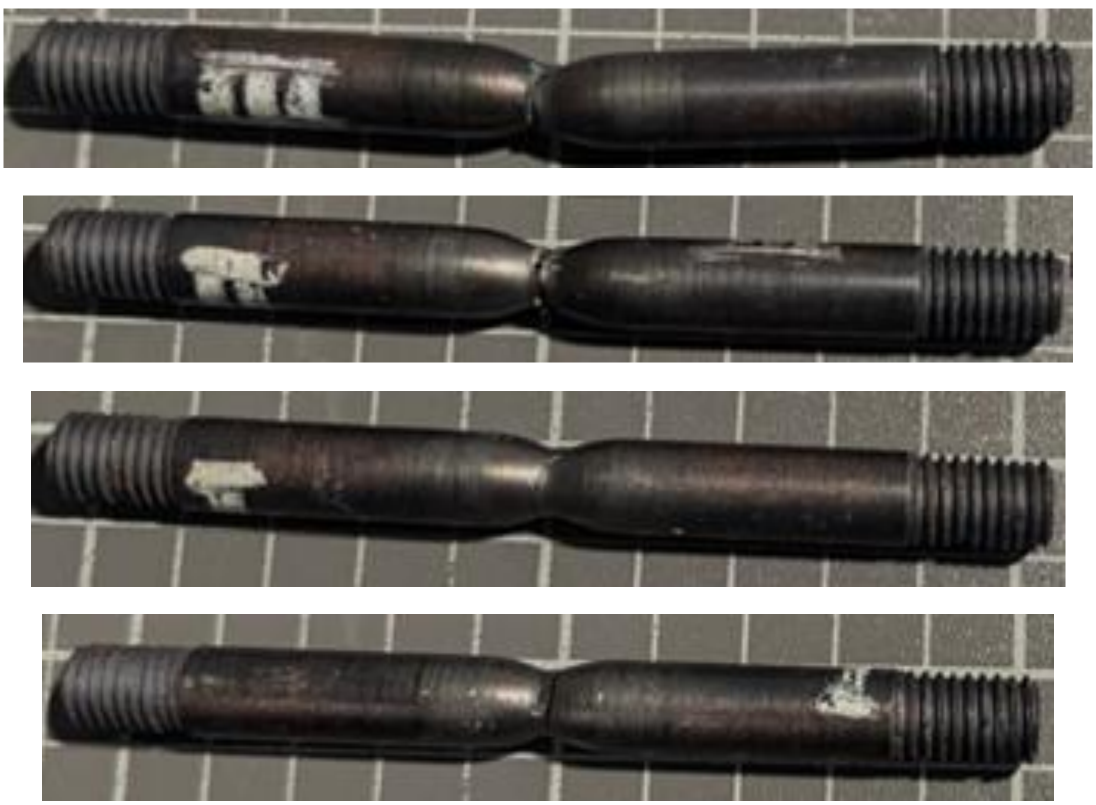

a)

b)

c)

d)

Figure 50. The mechanically simulated samples, tested at four different strain rates after failure in the Gleeble simulator: a) 2.54 s-1, b) 25.4 s-1, c) 254 s-1, d) 1016 s-1.

5.2. Results and discussion

The tensile test results presented in Figure 51 and Table 9 indicate no significant degradation in mechanical properties across the three thermally simulated samples. The initial sample (no thermal cycling), as well as those subjected to 40 and 80 thermal cycles, all exhibit similar ultimate tensile strengths (ranging from 1567 MPa to 1667 MPa) and tensile strains at break (between 15.3% and 16.1%). Although a slight reduction in elastic modulus is observed with increased thermal exposure, dropping from 310 GPa in the initial sample to 153 GPa after 80 cycles, the overall tensile behaviour remains consistent. These results indicate that, under the tested conditions, repeated thermal cycling up to 80 cycles does not drastically affect the room-temperature tensile performance of H13 steel. These results suggest that repeated thermal cycling, under the conditions tested, does not significantly degrade the room-temperature mechanical properties of H13 tool steel.

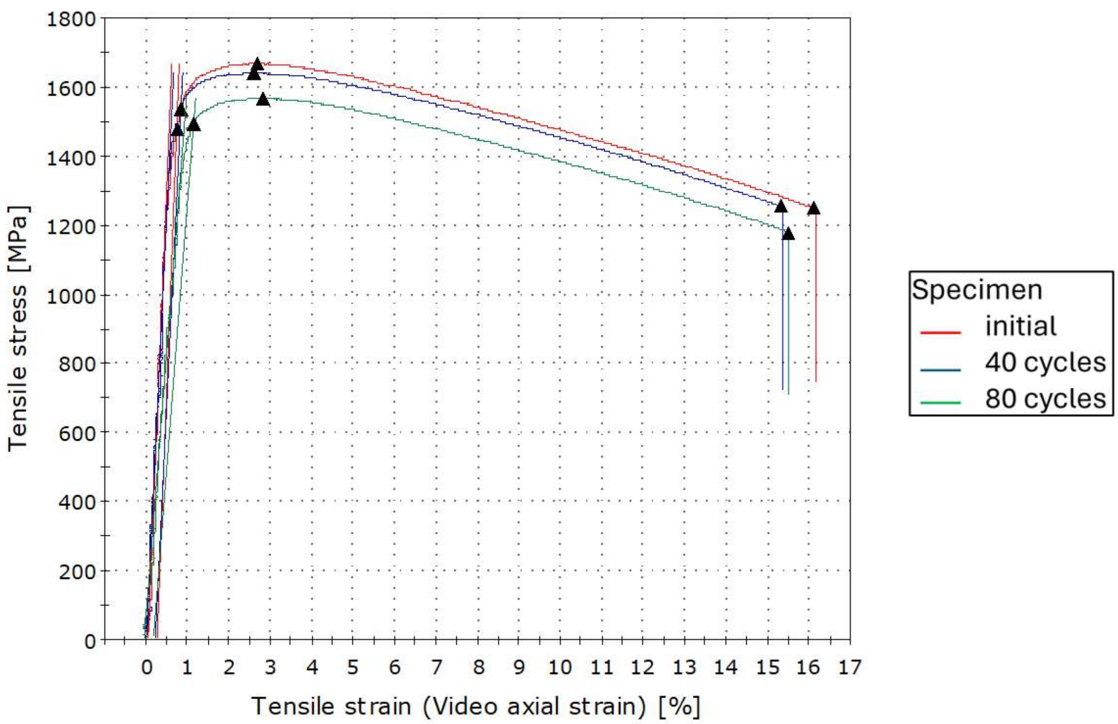

Figure 51. Tensile Stress–Strain Curves of Thermally Simulated Samples: initial, 40 cycles.80 cycles.

Table 9. Tensile Test Results of Thermally Simulated Samples at Room Temperature.

Number of thermal cycles	Gauge length [mm]	Diameter [mm]	Modulus [GPa]	Yield stress [MPa]	Tensile stress [MPa]	Tensile strain at Break [%]
0 (initial)	13.39	6.04	310	1475	1667	16.1
40	13.77	6.08	251	1538	1640	15.3
80	13.52	6.10	153	1492	1567	15.5

Figure 52 presents the macroscopic fracture surfaces of H13 steel samples after 40 and 80 thermal cycles, alongside the initial sample without any cycles. It reveals distinct zones that reflect different stages of fracture progression. Each sample clearly exhibits a central rapid fracture zone, where final separation occurred abruptly, surrounded by a crack propagation zone located toward the edge. The propagation zone is characterised by radial striations and surface texture variations, indicating progressive crack advancement under increasing local stress, likely associated with shear-dominated deformation. This outer region can also be interpreted as the transverse fracture zone, consistent with shear lip formation observed in ductile materials under combined axial and torsional loading. The spiral and curved patterns, particularly in the 40- and 80-cycle samples, suggest that fracture progression followed a helical path, a characteristic often associated with torsional overload rather than pure tension or fatigue.

Figure 53 provides high-magnification SEM images of the fracture surfaces, comparing both the centre and edge regions for each thermal condition. All surfaces exhibit a dimpled morphology, indicative of microvoid nucleation and coalescence, a characteristic of ductile fracture. Importantly, no significant differences in dimple size, shape, or density are observed between the samples, regardless of thermal cycling history. The only recurring difference is that the edge regions consistently show a slightly higher number of small surface cracks, as it is the zone of crack propagation. However, this difference does not suggest a transition in fracture mode or thermal degradation. This finding is consistent with previous thermal-fatigue studies on H13 steel, where noticeable cracking occurred only after several hundred thermal cycles between 25–750 °C, demonstrating the strong thermal resistance of H13 under thermal transients and fatigue cycling up to around 500 cycles [108].

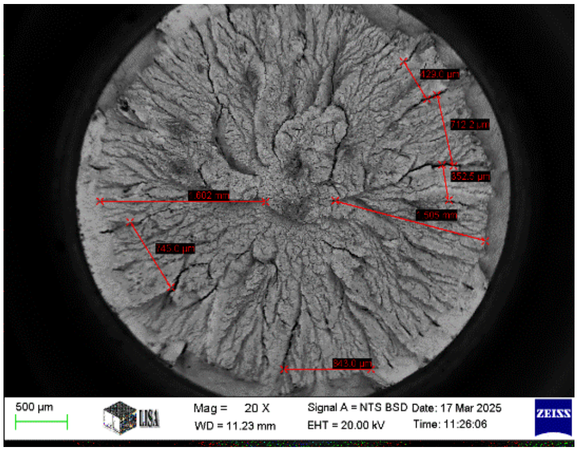

a)

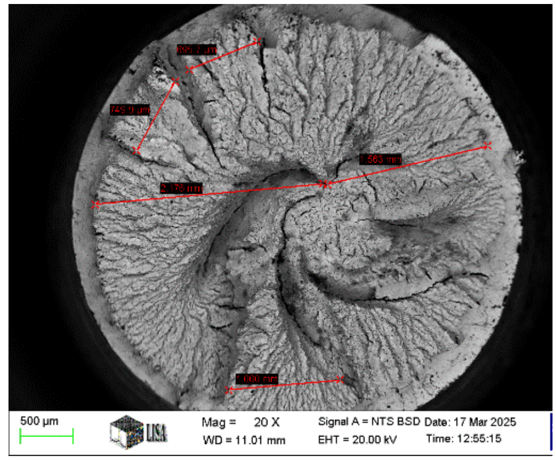

a) b)

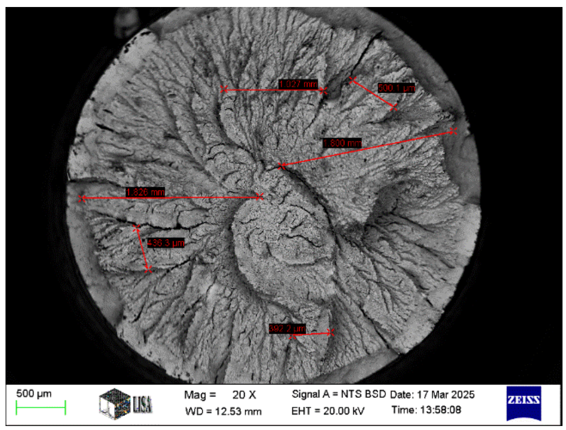

c)

Figure 52. Surface topography of Thermally Simulated Samples Under Different Thermal Cycling Conditions: (a) Initial sample without thermal cycling, (b) Sample after 40 thermal cycles, (c) Sample after 80 thermal cycles.

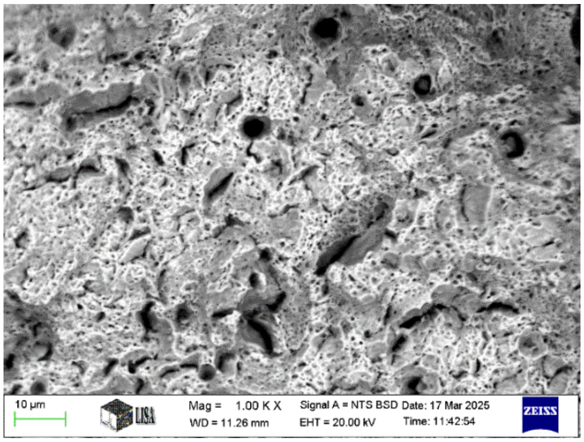

a)

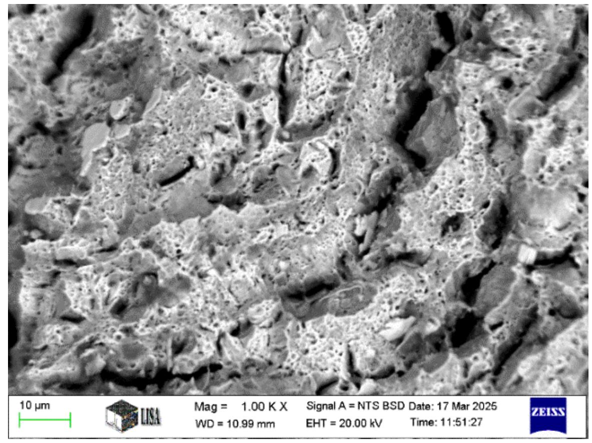

b)

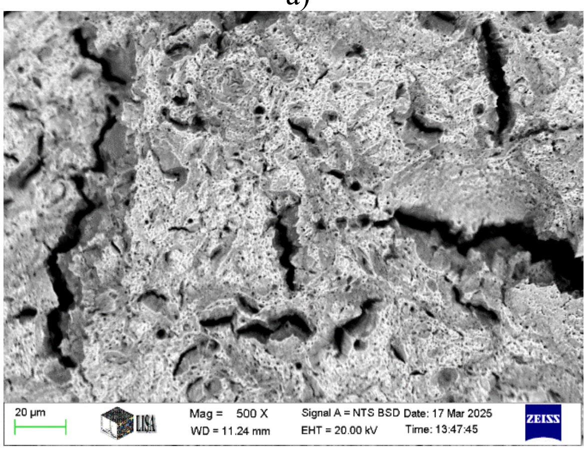

c)

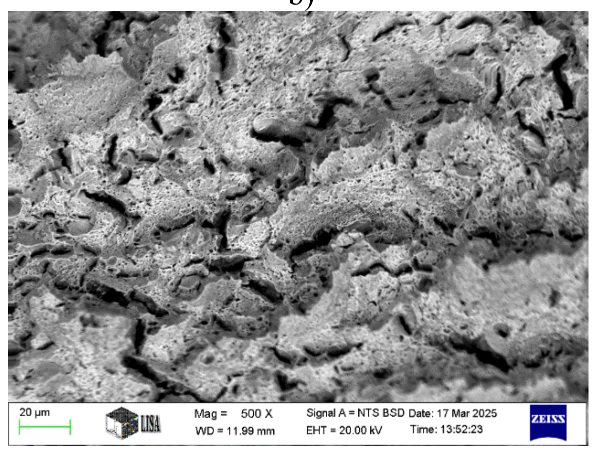

d)

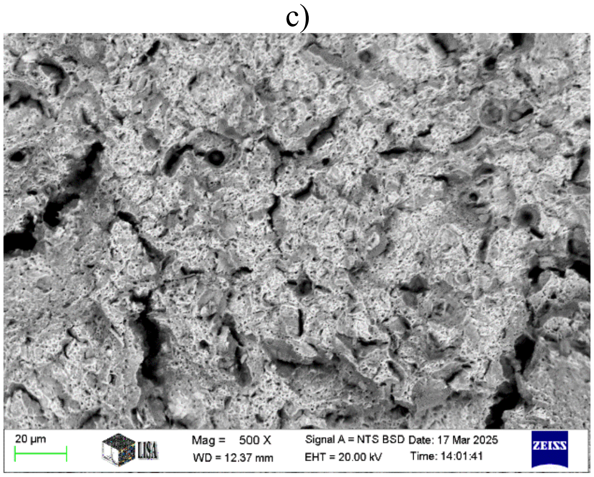

e)

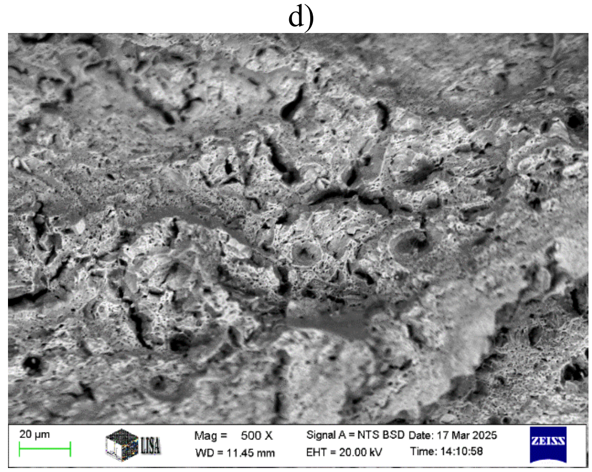

f)

Figure 53. SEM fractographs of thermally simulated samples under different thermal cycling conditions: (a–b) Initial sample without thermal cycling, (c–d) Sample after 40 thermal cycles, (e–f) Sample after 80 thermal cycles. Images (a, c, e) were taken from the centre of the fracture surface, while (b, d, f) were taken from the edge.

Figure 54 illustrates the tensile stress–strain response of H13 steel at 620 °C under strain rates of 2.54, 25.4, 254, and 1016 s^{-1}. Table 10 shows that the tensile stress (Rmax) increased from approximately 1040 MPa at 2.54 s^{1} to 1105 MPa at 254 s^{1}, accompanied by a rise in dissipated energy to nearly 490 J, demonstrating an apparent strain-rate hardening effect. When the strain rate was further increased to 1016 s^{-1}, Rmax declined slightly to 1082 MPa, and the absorbed energy decreased, indicating the onset of adiabatic thermal softening, where the heat generated by rapid plastic deformation cannot dissipate quickly and locally reduces the flow stress.

This trend confirms that H13 steel exhibits strain-rate sensitivity at elevated temperatures, a factor that can significantly influence tool performance and service life during the aggressive plunge stage of friction stir welding.

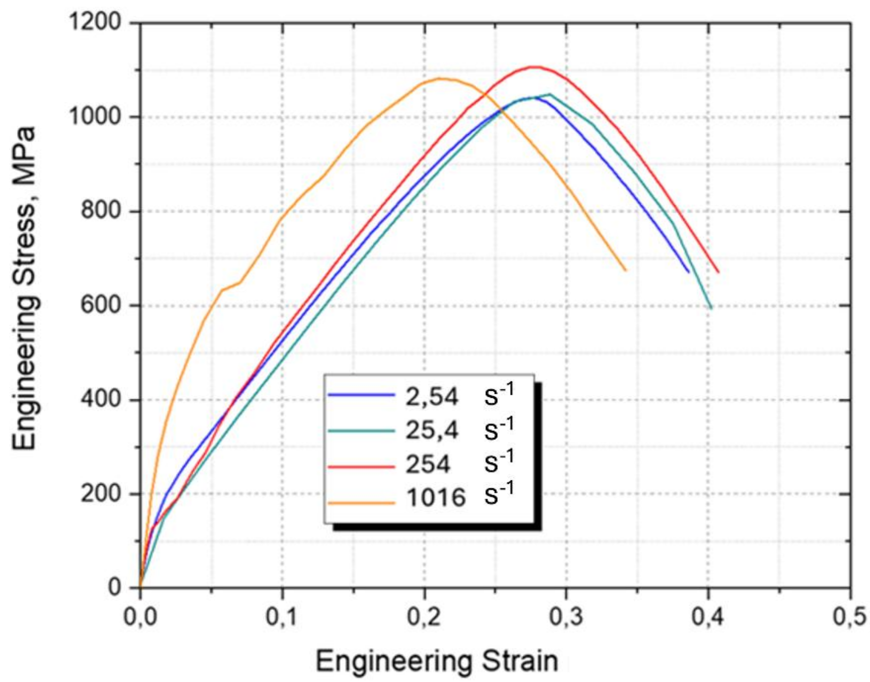

Figure 54. Tensile stress–strain curves of mechanically simulated samples tested at 620 °C under varying strain rates: 2.54, 25.4, 254, and 1016 s-1.

Table 10. Mechanical Test Results of Gleeble-Simulated Samples Under Varying Strain Rates at 620 °C.

	A, % (L_0=20mm)	Z, %	A_{Rmax}, %	R_{max}, MPa	Dissipated Energy, J
2.54 mm/s	18.2	51.4	27.5	1 041	440
25.4 mm/s	13.8	57.6	28.8	1 048	457
254 mm/s	20.6	58.1	28.1	1 106	490
1016 mm/s	21.8	59.4	21.0	1 082	453

Figure 55 presents the macroscopic fracture surfaces of H13 steel samples tested at 620 °C under strain rates of 2.54, 25.4, 254, and 1016 s^{-1}. All specimens fractured under uniaxial tensile loading and displayed the classic cup-and-cone morphology typical of ductile failure, with a central fibrous zone produced by microvoid coalescence surrounded by inclined shear lips formed along 45° planes where maximum shear stress develops. As the strain rate increased from 2.54 to 254 s^{-1}, the diameter of the central plastic deformation zone became progressively larger, indicating that moderate strain-rate hardening promoted more uniform and extensive plastic flow. At the highest strain rate of 1016 s^{-1}, the central zone significantly decreased in size, indicating that deformation became more localised and cracks propagated at an accelerated pace. The presence of shear lips confirms that the fracture mechanism remained ductile and shear-driven.

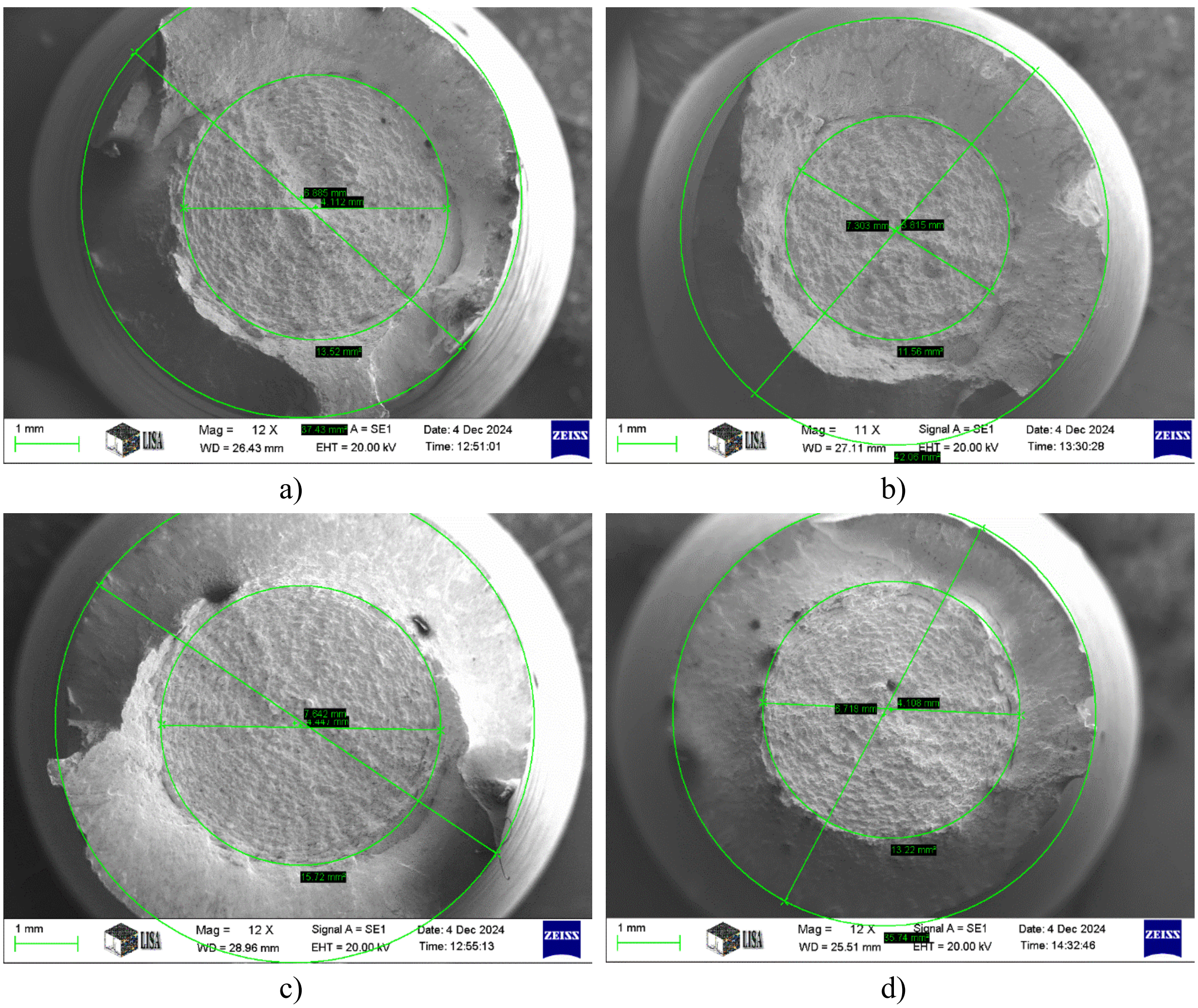

Figure 55. SEM Images of Fractured Surfaces of Mechanically Simulated Samples Under Different Strain Rates: a) 2.54 s-1,b) 25.4 s-1,c) 254 s-1,d) 1016 s-1.

Additionally, the observed changes in plastic-zone size with varying strain rates align with the mechanical findings (Figure 54 and Table 10). At the extreme loading of 1016 s^{-1}, adiabatic thermal softening becomes prominent enough to counteract any further strain-rate strengthening [109]. At this elevated rate, the rapid conversion of plastic work into heat leads to local self-heating, which decreases flow stress and concentrates deformation. This process ultimately limits further strength gains and accelerates crack propagation, ultimately leading to final failure.

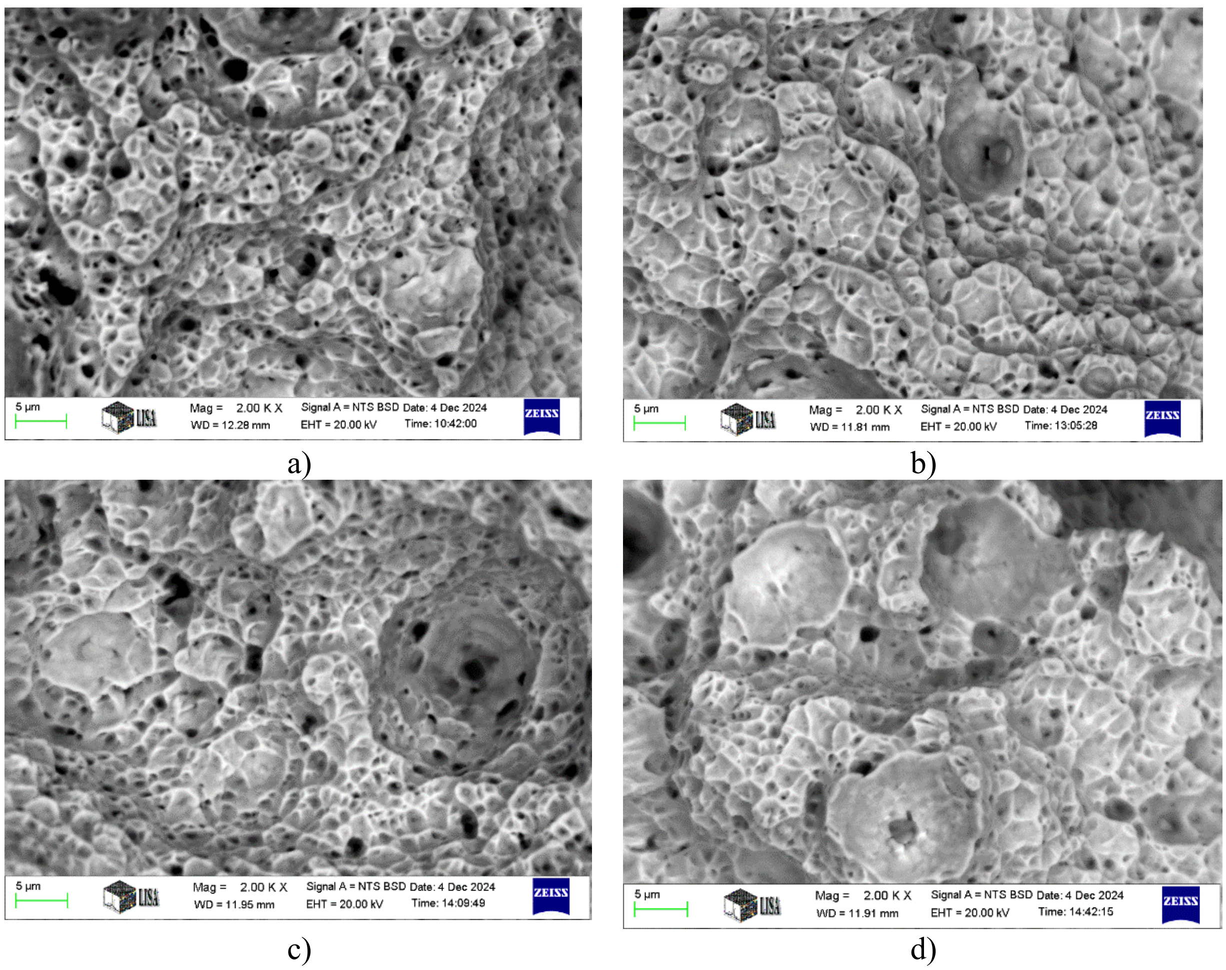

Figure 56. SEM Fractographs of Mechanically Simulated Samples Showing Ductile Fracture Features: a) 2.54 s-1,b) 25.4 s-1,c) 254 s-1,d) 1016 s-1.

Figure 56 shows SEM fractographs of H13 steel fractured at 620 °C under strain rates of 2.54, 25.4, 254, and 1016 s^{-1}. All samples display the classic dimpled morphology of ductile fracture, indicating that microvoid nucleation, growth, and coalescence remained the dominant failure mechanism across the full range of strain rates. Closer inspection and comparison with the macroscopic fracture surfaces (Figure 56) suggest only minor microstructural trends: a slight increase in average dimple size and depth from 2.54 to 254 s^{-1}, consistent with enhanced plastic flow from strain-rate hardening, followed by a modest refinement and less uniform dimple shape at 1016 s^{-1}. These microscopic observations are fully consistent with the mechanical results (Figure 54 and Table 10) and the macroscopic fracture features (Figure 55). Mechanical testing reveals that as the strain rate increases from low levels to approximately 254 s-1, H13 exhibits clear strain-rate hardening: plastic deformation remains uniform, the fracture surface develops large, deep dimples, and the maximum tensile stress increases. At the extreme strain rate of 1016 s^{-1}, however, deformation occurs so rapidly that most of the plastic work is converted to heat faster than it can be dissipated. This produces adiabatic thermal softening, where small regions within the steel experience a sharp temperature rise and a drop in flow stress. Strain localises in these softened regions, reducing the size of the central plastic zone and creating finer, irregular dimples on the fracture surface. Each plunge subjects the tool to such a single high-rate event, allowing these localised hot spots to initiate and grow microcracks with every cycle. Over successive welds, repeated microcrack nucleation and growth can outweigh the normal strengthening from higher strain rates, ultimately leading to early failure of the H13 tool, even though the alloy remains thermally stable under pure heating and cooling cycles.

5.3. Chapter-related claim

Claim No3.- On the Behaviour of H13 Tool Material under FSW-Induced Transients

To replicate the transient conditions experienced during the plunge stage of FSW, both thermal and mechanical simulations were conducted using a Gleeble 3000 thermo-mechanical simulator. Cylindrical samples were subjected to thermal transients with 40 and 80 cycles between 100 °C and 620 °C at a heating rate of 500 °C/s and a cooling rate of 8 °C/s. Tensile tests were conducted to investigate mechanical transient sensitivity at 600 °C with strain rates of 2.54, 25.5, 254, and 1016 mm/s. Through in-depth microstructural examination and mechanical properties, I establish the following findings regarding the plunge stage transient sensitivity:

Mechanical transients, rather than thermal cycles, are the dominant contributors to early tool damage during the aggressive plunge stage of FSW, because H13 tool steel remains thermally stable under rapid heating and cooling yet is markedly sensitive to strain rate at the temperatures reached in this stage.

This conclusion is supported by the following observations, which separate the negligible influence of thermal cycling from the clear influence of strain rate. Thermal cycling history has no measurable effect on the fracture surface: no significant differences in dimple size, shape, or density are observed between samples, and only 2% and 6% drops in tensile stress are observed, regardless of thermal history (40, 80 cycles). Strain rate, by contrast, governs the mechanical response at 620 °C. Tensile strength rises from 1040 MPa at 2.54 mm/s to

1105 MPa at 254 mm/s, indicating strain-rate hardening. At the extreme strain rate of 1016 s^{-1}, however, deformation occurs so rapidly that most of the plastic work is converted to heat faster than it can be dissipated. The tensile stress falls slightly to 1082 MPa as adiabatic thermal softening sets in.

Chapter 6: Relevance of the Research

Friction Stir Welding has become one of the most important advances in modern joining technology, valued across aerospace, automotive, shipbuilding, and rail industries for its ability to produce strong, defect-free joints without melting the base material. As technology continues to expand into more demanding applications, thicker sections, higher-strength alloys, and increasingly difficult material combinations have made the reliability and service life of the welding tool itself central concerns for industry. Tool failure is not merely a technical inconvenience; it translates directly into production downtime, increased manufacturing costs, and, in some cases, compromised weld quality, particularly when premium tool materials are required to withstand the severe thermal and mechanical conditions of the process.

Despite the widespread industrial use of FSW, tool degradation and failure are still frequently managed reactively rather than proactively. Tools are commonly used until they visibly fail or begin producing defective welds, at which point they are discarded, often without a clear understanding of the underlying mechanisms that led to their degradation. This lack of mechanistic insight limits the ability of manufacturers to anticipate failure, optimise maintenance schedules, or make informed decisions about tool material selection and process parameters. It also means that costly, high-performance tool materials are frequently replaced entirely, rather than repaired or reused, even when only a small region of the tool has actually failed.

Beyond its industrial relevance, this research also carries significant value from a materials science and metallurgical perspective. MP159 is a cobalt-based superalloy used in many demanding structural and aerospace applications, owing to its high strength, toughness, and stability under severe thermal and mechanical conditions. Given its use in such critical applications, developing a deeper understanding of how this alloy actually behaves, transforms, and degrades under real service conditions is of considerable value, not only for the specific tooling application studied here, but for the broader metallurgical understanding of cobalt-based superalloys more generally. Insights into its microstructural evolution, deformation behaviour, and failure mechanisms under genuine service loading can inform future research on this and metallurgically similar superalloy systems, extending well beyond the specific context of friction stir welding tooling.

This research is motivated by the practical need to address these challenges. By combining detailed failure analysis of real, in-service tools, the development of a viable repair strategy using additive manufacturing, and controlled physical simulation of the most severe loading conditions experienced during welding, this work aims to build a more complete and evidence-based understanding of how, why, and when FSW tools fail and what can be done about it. Such an understanding has direct industrial value: it supports more informed tool design and material selection, enables the possibility of repairing and reusing expensive tool materials rather than discarding them, and provides insight into the transient conditions that most contribute to early tool degradation, insight that is otherwise difficult to obtain from production welding trials alone.

Ultimately, as FSW continues to be adopted for increasingly demanding structural and industrial applications, a clearer, mechanistically grounded understanding of tool degradation becomes progressively more valuable both for industry seeking more reliable and cost-effective tooling solutions, and for the broader materials science community working to understand how advanced superalloys such as MP159 behave and degrade under real, service-representative conditions.

Chapter 7: Summary

I studied the FSW process from the tool's perspective, from the newer Co-base alloy MP159 to the established H13 'workhorse' steel. My contribution was characterising how MP159 wears, fails, and can be cost-effectively rebuilt, and identifying the main driver of early-stage H13 plunge damage.

The dissertation gives deep details on how Friction Stir Welding tools degrade, and how that degradation can be understood, repaired, and mitigated, through three linked investigations centred on a failed MP159 SSFSW probe and H13 tool steel: microstructural characterisation of an in-service failure, additive manufacturing-based repair of the failed component, and controlled physical simulation of the plunge stage using a Gleeble thermo-mechanical simulator.

Forensic examination of the worn MP159 probe traced its failure to a single, continuous physical process rather than a set of unrelated surface phenomena. Sustained frictional contact at the probe surface was found to drive dynamic recrystallisation whose intensity decays with depth, leaving behind a layered microstructure that mirrors the thermomechanical history experienced at each point beneath the wear surface. Hardness testing linked this recrystallised layer to a measurable loss of strength, and fractographic evidence from multiple failure sites showed that cracking consistently initiated and propagated along the boundaries of this softened layer. Read together, these observations reframe probe failure as a wear-driven microstructural transformation that actively creates its own fracture path, rather than a passive accumulation of surface damage.

Working from this understanding, the dissertation then evaluates whether such probes can be economically restored rather than discarded. Laser Metal Deposition with Powder, using Stellite 6 as the filler material, was shown to reconstruct the worn probe geometry while forming a sound metallurgical bond with the MP159 substrate. Process refinements, particularly the introduction of a brief pause between deposited layers, were found to limit heat input into the substrate and produce a more uniform, better-controlled build. Rather than weakening the tool, the softened zone this process leaves in the substrate was shown to behave as a compliant transition region that does not compromise the interface. Considered alongside a comparison of material and energy demands against manufacturing a new probe, this establishes repair as a technically sound and materially efficient alternative to replacement.

The final investigation isolates the plunge stage of FSW, identified in the literature as the most demanding phase of the process, and asks specifically what role thermal cycling versus rapid mechanical loading plays in early tool damage. Simulated thermal cycling representative of repeated plunges produced no measurable degradation in H13, whereas simulated mechanical loading at the strain rates characteristic of plunging revealed a distinct rate-dependent response: strengthening as loading rate increased, followed by a reversal at the highest rate tested, consistent with localised, deformation-generated heating outpacing the material's ability to dissipate it. This result narrows the search for the dominant driver of early H13 tool damage to the mechanical, rather than thermal, component of the plunge.

Considered together, these three studies connect a specific, physically grounded failure mechanism to a validated route for extending tool life, and to an isolated account of the loading condition most responsible for triggering that failure in the first place an integrated account of FSW tool degradation built from direct physical evidence rather than inference from macroscopic service life alone.

Chapter 8: Dissertation Scientific Claims

Claim No. 1. – On the failure mechanisms in MP 159 probe used in Stationary Shoulder Friction Stir Welding

Through in-depth microstructural examination and hardness measurement, I establish the following findings regarding the failure process of an MP159-grade welding probe. The probe was used in the SS-FSW welding of an aluminium alloy under normal operating conditions and failed after reaching its average service life:

The failure of the MP159 SS-FSW probe is not a set of independent surface phenomena but the outcome of a single causal sequence: frictional wear at the sliding interface drives depth-dependent dynamic recrystallisation of the near-surface material, forming a softened, structurally weakened layer whose intergranular cracking and delamination ultimately end the service life of the probe.

This conclusion is supported by the following observations, which together trace the failure from its thermomechanical origin to the terminal loss of material. The intensity of dynamic recrystallisation beneath the worn surface is set directly by the severity of local thermomechanical exposure. Because both temperature and strain rate peak at the sliding contact and decay with depth, the microstructure grades continuously from fully recrystallised at the interface to unaffected in the bulk: an extremely fine, twin-free layer at the surface, a partially transformed region beneath it, and the coarse, twinned parent alloy further still. Discontinuous dynamic recrystallisation nucleates preferentially at original grain and twin boundaries, a mechanism independently confirmed for MP159 under hot deformation. The microstructure, therefore, records the thermomechanical severity experienced at each depth during service. Where this recrystallisation is most complete, the alloy is measurably weakest, because the transformation destroys the dislocation and twin-boundary substructure responsible for the parent material's strength. This loss outweighs any Hall–Petch gain from the accompanying grain refinement. This softened, recrystallised layer is not a passive byproduct of service but the active origin of failure. Its abundance of fresh, immature grain boundaries offers little resistance to intergranular cracking, and the delamination that follows, not the preceding wear, deformation, or cracking, is what removes material and ends the service life. Every other form of surface damage, adhesive wear, plastic smearing, subsurface cracking, alters or weakens the surface but leaves it attached; only delamination detaches material from the probe. The evidence therefore converges on one conclusion: the probe fails not because its surface is worn, but because sustained wear and friction-induced recrystallisation strip the near-surface material of the internal structure needed to resist fracture, and it is this loss, expressed as delamination, that constitutes the true failure event.

Claim No2. – On the remanufacturing of a worn cobalt-nickel-based (MP159) Stationary Shoulder Friction Stir Welding probe

Through in-depth microstructural examination and hardness measurements, I establish the following findings regarding the success of the repair process for an MP159-grade welding probe that failed after an average service life of SS-FSW welding of aluminium alloys. The dimensional restoration was performed using additive manufacturing techniques, specifically Laser Metal Deposition, with Stellite 6 powder:

(a) Laser Metal Deposition with Powder is a metallurgically sound method for rebuilding worn MP159 SS-FSW probes with Stellite 6, because the process produces a strong, defect-free deposit whose microstructure bonds reliably to the substrate.

This conclusion is supported by the following observations, which establish both the integrity of the bond and the role of the softened substrate zone beneath it. The Stellite 6 deposits form a strong metallurgical bond with the MP159 substrate, with defect-free layers, a well-developed dendritic microstructure, and consistent hardness throughout the deposited material. Together, these demonstrate that the rebuild is structurally sound rather than merely adhered. The process induces a softened heat-affected zone in the substrate through localised thermal exposure during deposition, but microstructural analysis shows that this region retains a sound metallurgical bond with the deposit and does not compromise the interface integrity. Rather than a defect, the gradual hardness transition across the softened HAZ acts as a ductile transition layer that relieves stress concentration at the interface and may itself enhance the durability of the remanufactured probe.

(b) Introducing a controlled cooling interval between deposited layers improves the quality and durability of the rebuilt probe, making it a key process parameter rather than an optional refinement.

This conclusion is supported by the following observations, which link the cooling interval to measurable improvements in the deposit and the substrate beneath it. Compared with continuous deposition, a 10-second cooling interval between layers significantly reduces the depth of the heat-affected zone in the substrate, minimises thermal distortion, and improves layer uniformity. By limiting the accumulated thermal load, controlled cooling directly constrains the extent of the softened HAZ and yields a more uniform deposit, establishing it as a decisive lever for both LMDp quality and tool durability.

(c) Remanufacturing MP159 SS-FSW probes by LMDp is economically and environmentally advantageous compared with producing new tools because it restores only the worn section rather than replacing the entire probe.

This conclusion is supported by the following observations, which quantify the economic savings and the environmental benefit of repair over replacement. Repairing the worn region alone achieves 31–56% lower production costs than manufacturing a new probe, with corresponding reductions in material and energy use. Environmentally, the approach preserves roughly 90% of the original material, cuts industrial waste and CO_2 emissions, and aligns with sustainable manufacturing principles.

Claim No3.- On the Behaviour of H13 Tool Material under FSW-Induced Transients

To replicate the transient conditions experienced during the plunge stage of FSW, both thermal and mechanical simulations were conducted using a Gleeble 3000 thermo-mechanical simulator. Cylindrical samples were subjected to thermal transients with 40 and 80 cycles between 100 °C and 620 °C at a heating rate of 500 °C/s and a cooling rate of 8 °C/s. Tensile tests were conducted to investigate mechanical transient sensitivity at 600°C with strain rates of 2.54, 25.5, 254, and 1016 mm/s. Through in-depth microstructural examination and mechanical properties, I establish the following findings regarding the plunge stage transient sensitivity:

Mechanical transients, rather than thermal cycles, are the dominant contributors to early tool damage during the aggressive plunge stage of FSW, because H13 tool steel remains thermally stable under rapid heating and cooling yet is markedly sensitive to strain rate at the temperatures reached in this stage.

This conclusion is supported by the following observations, which separate the negligible influence of thermal cycling from the clear influence of strain rate. Thermal cycling history has no measurable effect on the fracture surface: no significant differences in dimple size, shape, or density are observed between samples, and only 2% and 6% drops in tensile stress are observed, regardless of thermal history (40, 80 cycles). Strain rate, by contrast, governs the mechanical response at 620 °C. Tensile strength rises from 1040 MPa at 2.54 mm/s to 1105 MPa at 254 mm/s, indicating strain-rate hardening. At the extreme strain rate of 1016 s^{-1}, however, deformation occurs so rapidly that most of the plastic work is converted to heat faster than it can be dissipated. The tensile stress falls slightly to 1082 MPa as adiabatic thermal softening sets in.

Chapter 9: List of Publications

Journal Articles

1. N. E. Djimaoui, D. Koncz-Horvath, Y. Adonyi, S.S. Sina, J. Everall, E. Hoyos, V. Mertinger, "Rebuilding of stationary shoulder friction stir welding MP159 probes by laser metal deposition using Stellite 6 powder," *Materials Today Communications*, vol. 50, Paper 114213, 17 p., 2026.
2. N. E. Djimaoui, Y. Adonyi, L. Kuzsella, E. Hoyos, Á. Győző Kovács, V. Mertinger, "Physical simulation of thermal and mechanical transients on H13 tool steel during the plunge stage of friction stir welding," *Materials Today Communications*, vol. 52, Paper 115059, 10 p., 2026.
3. N. E. Djimaoui, Z. Boumerzoug, "Laser and TIG welding of low carbon steel for LPG car tank industry," *Insights in Mining Science & Technology*, vol. 4, no. 1, Paper 555627, 6 p., 2023.
4. N. E. Djimaoui, V. Mertinger, Y. Adonyi, "An overview of possible FSW wear mechanisms," *Doktorandusz Almanach 2023*, pp. 295–300, 2023.

Conference Papers

5. N. E. Djimaoui, V. Mertinger, Y. Adonyi, "Overview about wear and plastic deformation of MP159 alloy," in *27th International Students Day of Metallurgy (ISDM 2024) Conference Proceedings*, 2024, pp. 34–40.
6. N. E. Djimaoui, Y. Adonyi, V. Mertinger, "Physical Simulations of the Tool Degradation in Friction Stir Welding," in M. Csüllög, T. Mankovits (eds.), *Book of Abstracts, 11th International Scientific Conference on Advances in Mechanical Engineering (ISCAME 2025)*, Bäch, Switzerland: Trans Tech Publications Ltd., 2025, p. 80.
7. N. E. Djimaoui, V. Mertinger, Y. Adonyi, J. De Backer, "Physical Simulations of the Tool Degradation in Friction Stir Welding," in P. J. Szabó, I. Kónya, G. Szakáts, T. Krasznai (eds.), *XIV. Országos Anyagtudományi Konferencia, Absztraktok*, Balatonalmádi, Hungary, 2023, p. 56.
8. N. E. Djimaoui, V. Mertinger, Y. Adonyi, "Failure characterization of tool in friction stir welding," in P. Hajdú (ed.), *XXVI. Tavaszi Szél Konferencia 2023, Absztrakt kötet*, Budapest, Hungary: Association of Hungarian PhD and DLA Students, 2023, p. 278.

Conference Presentations / Abstracts

9. N. E. Djimaoui, V. Mertinger, Y. Adonyi, "Characterization of FSW Tool Wear and Degradation," presented at *International Students' Day of Metallurgy (ISDM 2024)*, Freiberg, Germany, Apr. 10, 2024.

10. N. E. Djimaoui, V. Mertinger, Y. Adonyi, "Rebuilding of Friction Stir Welding tool using Additive Manufacturing," presented at *Tavaszi Szél Konferencia 2024*, 2024.

11. N. E. Djimaoui, V. Mertinger, Y. Adonyi, "Examinations of FSW tool degradation," presented at the *MTA MAB Anyagtudományi- és Technológiai Szakbizottság* event, Miskolc, Nov. 14, 2023.

12. N. E. Djimaoui, V. Mertinger, Y. Adonyi, "TIG welding of low carbon steel for LPG car tank industry," presented at *Hungarian Science Day*, Miskolc, Nov. 10, 2022.

Chapter 10: AI statement

During the preparation of the thesis, I did not use artificial intelligence services, except for grammatical and stylistic corrections.

Chapter 11: References

[1] R. S. Mishra, Z. Y. Ma, Friction stir welding and processing, Materials Science and Engineering: R: Reports 50 (2005) 1–78, https://doi.org/10.1016/j.mser.2005.07.001.

[2] K. Wayne Stephan |. Nicholas, David |. Thomas, Friction Stir Welding: Invention, Innovation and Application. [Online]. Available: https://www.twi-global.com/technical-knowledge/published-papers/friction-stir-welding-invention-innovations-and-applications-march-2001.aspx (accessed Sep. 19, 2025).

[3] A critical review of friction stir welding process | CASTMAN. [Online]. Available: https://castman.co.kr/a-critical-review-of-friction-stir-welding-process/ (accessed Sep. 19, 2025).

[4] D. Jacquin, G. Guillemot, A review of microstructural changes occurring during FSW in aluminium alloys and their modelling, Journal of Materials Processing Technology 288 (2021) 116706, https://doi.org/10.1016/j.jmatprotec.2020.116706.

[5] S. S. Baghel, P. K. Soni, An experimental study of friction stir welding parameters effect on joint properties of aluminium alloy and copper plate, Mater. Res. Express 10 (2023) 016502, https://doi.org/10.1088/2053-1591/acae54.

[6] G. Padmanaban, V. Balasubramanian, Selection of FSW tool pin profile, shoulder diameter and material for joining AZ31B magnesium alloy – An experimental approach, Materials & Design 30 (2009) 2647–2656, https://doi.org/10.1016/j.matdes.2008.10.021.

[7] Friction Stir Welding - Friction Stir Welding Process and Applications. Sunrise Metal - Aluminium Die Casting Expert. [Online]. Available: https://www.sunrise-metal.com/friction-stir-welding-process-and-applications/ (accessed Apr. 23, 2026).

[8] H. K. Mohanty, M. M. Mahapatra, P. Kumar, P. Biswas, N. R. Mandal, Effect of tool shoulder and pin probe profiles on friction stirred aluminum welds — a comparative study, J. Marine. Sci. Appl. 11 (2012) 200–207, https://doi.org/10.1007/s11804-012-1123-4.

[9] (PDF) Friction Stir Welding Developments. [Online]. Available: https://www.researchgate.net/publication/273060095_Friction_Stir_Welding_Developments (accessed Sep. 19, 2025).

[10] F. budi Darsono, S. T. Koin, K. Kriswanto, A. K. Thomas, R. D. Widodo, R. Rusiyanto, Effect of Pin Profile Tool on Friction Stir Welding Alumunium, E3S Web of Conf. 465 (2023) 01001, https://doi.org/10.1051/e3sconf/202346501001.

[11] J. S. Jesus, J. M. Costa, A. Loureiro, J. M. Ferreira, Assessment of friction stir welding aluminium T-joints, Journal of Materials Processing Technology 255 (2018) 387–399, https://doi.org/10.1016/j.jmatprotec.2017.12.036.

[12] Y. Zhao, S. Lin, L. Wu, F. Qu, The influence of pin geometry on bonding and mechanical properties in friction stir weld 2014 Al alloy, Materials Letters 59 (2005) 2948–2952, https://doi.org/10.1016/j.matlet.2005.04.048.

[13] N. Z. Khan, A. N. Siddiquee, Z. A. Khan, Friction Stir Welding: Dissimilar Aluminium Alloys, CRC Press, Boca Raton, 2017, https://doi.org/10.1201/9781315116815.

[14] Effect of Rotational Speed on Mechanical Properties of AA5083/AA6082 Friction Stir Welded T-Joints for Naval Applications. [Online]. Available: https://www.mdpi.com/2075-4701/14/12/1410 (accessed Sep. 21, 2025).

[15] A. H. Plaine, U. F. H. Suhuddin, N. G. Alcântara, J. F. dos Santos, Microstructure and mechanical behavior of friction spot welded AA6181-T4/Ti6Al4V dissimilar joints, Int J Adv Manuf Technol 92 (2017) 3703–3714, https://doi.org/10.1007/s00170-017-0439-2.

[16] Stream. [Online]. Available: https://watch.videodelivery.net/ec1cff13b61bea1fe076ca6a40ba5f14?poster=https%3A%2F%2Fvideodelivery.net%2Fec1cff13b61bea1fe076ca6a40ba5f14%2Fthumbnails%2Fthumbnail.jpg (accessed Sep. 21, 2025).

[17] A. K. R et al., Role of traversing speed and axial load on the properties of friction stir welded dissimilar AA6101-T6 AND AA1350 aluminium alloys, Journal of the Chinese Institute of Engineers 46 (2023) 81–85, https://doi.org/10.1080/02533839.2022.2141338.

[18] Influences of welding parameters on axial force and deformations of micro pinless friction stir welding | The International Journal of Advanced Manufacturing Technology. [Online]. Available: https://link.springer.com/article/10.1007/s00170-019-04739-2 (accessed Sep. 21, 2025).

[19] L. Long, G. Chen, S. Zhang, T. Liu, Q. Shi, Finite-element analysis of the tool tilt angle effect on the formation of friction stir welds, Journal of Manufacturing Processes 30 (2017) 562–569, https://doi.org/10.1016/j.jmapro.2017.10.023.

[20] P. Janaki Ramulu, R. Ganesh Narayanan, Influence of Shoulder Diameter, Plunge Depth, Welding Speed, Rotational Speed on the Tensile Behavior of Friction Stir Welded AA 6061-T6 Sheets, J. Test. Eval. 42 (2014) 601–613, https://doi.org/10.1520/JTE20120236.

[21] J. Teimurnezhad, H. Pashazadeh, A. Masumi, Effect of shoulder plunge depth on the weld morphology, macrograph and microstructure of copper FSW joints, Journal of Manufacturing Processes 22 (2016) 254–259, https://doi.org/10.1016/j.jmapro.2016.04.001.[22] S. Guerdoux, L. Fourment, A 3D numerical simulation of different phases of friction stir welding, Modelling Simul. Mater. Sci. Eng. 17 (2009) 075001, https://doi.org/10.1088/0965-0393/17/7/075001.

[23] V. Malik, N. K. Sanjeev, H. S. Hebbar, S. V. Kailas, Time Efficient Simulations of Plunge and Dwell Phase of FSW and its Significance in FSSW, Procedia Materials Science 5 (2014) 630–639, https://doi.org/10.1016/j.mspro.2014.07.309.

[24] L. Shi, C. S. Wu, Transient model of heat transfer and material flow at different stages of friction stir welding process, Journal of Manufacturing Processes 25 (2017) 323–339, https://doi.org/10.1016/j.jmapro.2016.11.008.

[25] R. Nandan, T. DebRoy, H. K. D. H. Bhadeshia, Recent advances in friction-stir welding – Process, weldment structure and properties, Progress in Materials Science 53 (2008) 980–1023, https://doi.org/10.1016/j.pmatsci.2008.05.001.

[26] D. M. Neto, P. Neto, Numerical modeling of friction stir welding process: a literature review, Int J Adv Manuf Technol 65 (2013) 115–126, https://doi.org/10.1007/s00170-012-4154-8.

[27] C. Zhang et al., Microstructure evolution of thermo-mechanically affected zone in dissimilar AA2024/7075 joint produced by friction stir welding, Vacuum 179 (2020) 109515, https://doi.org/10.1016/j.vacuum.2020.109515.

[28] P. Ferro, F. Bonollo, A Semianalytical Thermal Model for Fiction Stir Welding, Metallurgical and Materials Transactions A: Physical Metallurgy and Materials Science 41 (2009) 440–449, https://doi.org/10.1007/s11661-009-0104-y.

[29] S. Guerdoux, Numerical simulation of the friction stir welding process, PhD Thesis, École Nationale Supérieure des Mines de Paris, 2007. [Online]. Available: https://pastel.hal.science/tel-00271234 (accessed Sep. 26, 2025).

[30] S. Kilic, F. Ozturk, M. F. Demirdogen, A comprehensive literature review on friction stir welding: Process parameters, joint integrity, and mechanical properties, Journal of Engineering Research 13 (2025) 122–130, https://doi.org/10.1016/j.jer.2023.09.005.

[31] D. Dobraš, P. Tasić, I. Hajro, D. Hodzic, Energy efficient welding technology: FSW, 2013.

[32] D. Lohwasser, Z. Chen, Friction Stir Welding: From Basics to Applications, Elsevier, 2009.

[33] G. Wang, Y. Zhao, Y. Hao, Friction stir welding of high-strength aerospace aluminum alloy and application in rocket tank manufacturing, Journal of Materials Science & Technology 34 (2018) 73–91, https://doi.org/10.1016/j.jmst.2017.11.041.

[34] S. Patnaik, S. Chattopadhyaya, S. Shankar, Friction stir welding and its applications: An overview, AIP Conf. Proc. 2681 (2022) 020018, https://doi.org/10.1063/5.0116234.

[35] A. Silva-Magalhães, L. Cederqvist, J. De Backer, E. Håkansson, B. Ossiansson, G. Bolmsjö, A Friction Stir Welding case study using Temperature Controlled Robotics with a HPDC Cylinder Block and dissimilar materials joining, Journal of Manufacturing Processes 46 (2019) 177–184, https://doi.org/10.1016/j.jmapro.2019.08.012.

[36] Friction stir welding: Types, merits & demerits, applications, process variables & effect of tool pin profile - ScienceDirect. [Online]. Available: https://www.sciencedirect.com/science/article/pii/S2214785321077713 (accessed Sep. 27, 2025).

[37] Friction Stir Welding - TWI. [Online]. Available: https://www.twi-global.com/technical-knowledge/job-knowledge/friction-stir-welding-147 (accessed Sep. 27, 2025).

[38] Á. Meilinger, I. Török, The importance of friction stir welding tool.

[39] Friction stir welding: An overview on effect of tool variables, Materials Today: Proceedings 47 (2021) 7196–7202, https://doi.org/10.1016/j.matpr.2021.07.487.

[40] Experimental and Simulation Investigation on Fatigue Performance of H13 Steel Tools in Friction Stir Welding of Aluminum Alloys. [Online]. Available: https://www.mdpi.com/1996-1944/17/7/1535 (accessed Apr. 26, 2026).

[41] Review: Friction stir welding tools - R Rai, A De, H K D H Bhadeshia, T DebRoy, 2011. [Online]. Available: https://journals.sagepub.com/doi/full/10.1179/1362171811Y.0000000023 (accessed Apr. 26, 2026).

[42] Y. B. Tan et al., High-temperature tensile properties and strengthening mechanism of cryo-rolled MP159 superalloy strengthened by deformation nano-twins, Materials Characterization 209 (2024) 113692, https://doi.org/10.1016/j.matchar.2024.113692.

[43] J. S. Slaney, R. A. Nebiolo, Development of multiphase alloy MP159 using experimental statistics, Metallography 16 (1983) 137–160, https://doi.org/10.1016/0026-0800(83)90002-2.

[44] S.-Q. Lu, B.-Y. Huang, Y.-H. He, J.-C. Tang, Thermal stability of cold worked microstructure of MP159 alloy, Trans Nonferrous Met Soc China 12 (2002) 392–395.

[45] W. W. Zhang et al., Microstructure evolution and strengthening mechanisms of MP159 superalloy during room temperature rolling and cryorolling, Journal of Alloys and Compounds 908 (2022) 164667, https://doi.org/10.1016/j.jallcom.2022.164667.

[46] J. Gu, L. Guo, B. Gan, Z. Bi, M. Song, Microstructure and mechanical properties of an MP159 alloy processed by torsional deformation and subsequent annealing, Materials Science and Engineering: A 802 (2021) 140676, https://doi.org/10.1016/j.msea.2020.140676.

[47] Numerical residual strength prediction of stationary shoulder friction stir welding structures, Engineering Fracture Mechanics 230 (2020) 107010, https://doi.org/10.1016/j.engfracmech.2020.107010.

[48] Stationary shoulder FSW for joining high strength aluminum alloys, Journal of Materials Processing Technology 221 (2015) 187–196, https://doi.org/10.1016/j.jmatprotec.2015.02.015.

[49] M. J. Russell, C. Blignault, N. L. Horrex, C. S. Wiesner, Recent Developments in the Friction Stir Welding of Titanium Alloys, Weld World 52 (2008) 12–15, https://doi.org/10.1007/BF03266662.

[50] Mechanical behavior of FSW joint welded by a novel designed stationary shoulder tool, Journal of Materials Processing Technology 277 (2020) 116482, https://doi.org/10.1016/j.jmatprotec.2019.116482.

[51] Investigation of stationary shoulder friction stir welding of aluminum alloy 7075-T651, Journal of Materials Processing Technology 222 (2015) 391–398, https://doi.org/10.1016/j.jmatprotec.2015.03.036.

[52] Comparison of residual stress distributions in conventional and stationary shoulder high-strength aluminum alloy friction stir welds, Journal of Materials Processing Technology 242 (2017) 92–100, https://doi.org/10.1016/j.jmatprotec.2016.11.015.

[53] D. a. P. Prabhakar et al., A Review of Optimization and Measurement Techniques of the Friction Stir Welding (FSW) Process, Journal of Manufacturing and Materials Processing 7 (2023) 181, https://doi.org/10.3390/jmmp7050181.

[54] (1) (PDF) Friction Stir Welding Tool Life Assessment Through Fatigue Analysis. [Online]. Available: https://www.researchgate.net/publication/375901609_Friction_Stir_Welding_Tool_Life_Assessment_Through_Fatigue_Analysis (accessed Jun. 15, 2026).

[55] M. Akbari, M. Esfandiar, A. Abdollahzadeh, The role of force and torque in friction stir welding: A detailed review, Journal of Advanced Joining Processes 11 (2025) 100289, https://doi.org/10.1016/j.jajp.2025.100289.

[56] H. Atharifar, D. Lin, R. Kovacevic, Numerical and Experimental Investigations on the Loads Carried by the Tool During Friction Stir Welding, J. of Materi Eng and Perform 18 (2009) 339–350, https://doi.org/10.1007/s11665-008-9298-1.

[57] Force generation during friction stir welding of AA2024-T3, CIRP Annals 61 (2012) 9–12, https://doi.org/10.1016/j.cirp.2012.03.024.

[58] J. Das, G. A. Rao, S. K. Pabi, M. Sankaranarayana, T. K. Nandy, Thermo-mechanical processing, microstructure and tensile properties of a tungsten heavy alloy, Materials Science and Engineering: A 613 (2014) 48–59, https://doi.org/10.1016/j.msea.2014.06.072.

[59] J. Wang, J. Su, R. S. Mishra, R. Xu, J. A. Baumann, Tool wear mechanisms in friction stir welding of Ti–6Al–4V alloy, Wear 321 (2014) 25–32, https://doi.org/10.1016/j.wear.2014.09.010.

[60] S. R. Nathan, S. Malarvizhi, V. Balasubramanian, A. G. Rao, Failure analysis of tungsten based tool materials used in friction stir welding of high strength low alloy steels, Engineering Failure Analysis 66 (2016) 88–98, https://doi.org/10.1016/j.engfailanal.2016.04.018.

[61] Friction, Lubrication, and Wear Technology, ASM International, 2017, https://doi.org/10.31399/asm.hb.v18.9781627081924.

[62] R. Aghababaei, D. H. Warner, J.-F. Molinari, Critical length scale controls adhesive wear mechanisms, Nat Commun 7 (2016) 11816, https://doi.org/10.1038/ncomms11816.

[63] B. Podgornik, Adhesive Wear Failures, J Fail. Anal. and Preven. 22 (2022) 113–138, https://doi.org/10.1007/s11668-021-01322-4.

[64] A. Molinari, M. Nouari, Modeling of tool wear by diffusion in metal cutting, Wear 252 (2002) 135–149, https://doi.org/10.1016/S0043-1648(01)00858-4.

[65] N. Soda, Y. Kimura, A. Tanaka, Wear of some F.C.C. metals during unlubricated sliding part IV: Effects of atmospheric pressure on wear, Wear 43 (1977) 165–174, https://doi.org/10.1016/0043-1648(77)90111-9.

[66] N. P. Suh, An overview of the delamination theory of wear, Wear 44 (1977) 1–16, https://doi.org/10.1016/0043-1648(77)90081-3.

[67] F. F. Tao, A Study of Oxidation Phenomena in Corrosive Wear, ASLE TRANSACTIONS (1969), https://doi.org/10.1080/05698196908972251.

[68] K. V. Pool, C. K. H. Dharan, I. Finnie, Erosive wear of composite materials, Wear 107 (1986) 1–12, https://doi.org/10.1016/0043-1648(86)90043-8.

[69] R. Visintainer, V. Matoušek, L. Pullum, A. Sellgren, Erosive Wear, in: Slurry Transport Using Centrifugal Pumps, Springer International Publishing, Cham, 2023, pp. 399–443, https://doi.org/10.1007/978-3-031-25440-6_13.

[70] T. Yue, M. A. Wahab, A review on fretting wear mechanisms, models and numerical analyses, Computers, Materials & Continua 59 (2019) 405, https://doi.org/10.32604/cmc.2019.04253.

[71] G. W. Stachowiak, Wear: Materials, Mechanisms and Practice, John Wiley & Sons, 2006.

[72] A. Farias, G. F. Batalha, E. F. Prados, R. Magnabosco, S. Delijaicov, Tool wear evaluations in friction stir processing of commercial titanium Ti–6Al–4V, Wear 302 (2013) 1327–1333, https://doi.org/10.1016/j.wear.2012.10.025.

[73] S. Du, H. Liu, M. Jiang, L. Zhou, F. Gao, The performance of a Co-based alloy tool in the friction stir welding of TA5 alloy, Wear 488–489 (2022) 204180, https://doi.org/10.1016/j.wear.2021.204180.

[74] S. Hanke, G. V. B. Lemos, L. Bergmann, D. Martinazzi, J. F. dos Santos, T. R. Strohaecker, Degradation mechanisms of pcBN tool material during Friction Stir Welding of Ni-base alloy 625, Wear 376–377 (2017) 403–408, https://doi.org/10.1016/j.wear.2017.01.070.

[75] B. Vicharapu, H. Liu, Y. Morisada, H. Fujii, A. De, Degradation of nickel-bonded tungsten carbide tools in friction stir welding of high carbon steel, Int J Adv Manuf Technol 115 (2021) 1049–1061, https://doi.org/10.1007/s00170-021-07159-3.

[76] S. Yu. Tarasov, V. E. Rubtsov, E. A. Kolubaev, A proposed diffusion-controlled wear mechanism of alloy steel friction stir welding (FSW) tools used on an aluminum alloy, Wear 318 (2014) 130–134, https://doi.org/10.1016/j.wear.2014.06.014.

[77] L. Zuo, W. Shao, X. Zhang, D. Zuo, Investigation on tool wear in friction stir welding of SiCp/Al composites, Wear 498–499 (2022) 204331, https://doi.org/10.1016/j.wear.2022.204331.

[78] A. Bist, J. S. Saini, B. Sharma, A review of tool wear prediction during friction stir welding of aluminium matrix composite, Transactions of Nonferrous Metals Society of China 26 (2016) 2003–2018, https://doi.org/10.1016/S1003-6326(16)64318-2.

[79] S. Fritsche, F. Schindler, W. S. de Carvalho, S. T. Amancio-Filho, Wear mechanisms and failure analysis of a tool used in refill friction stir spot welding of AA6061-T6, Wear 560–561 (2025) 205610, https://doi.org/10.1016/j.wear.2024.205610.

[80] C. C. de Castro et al., Tool wear mechanisms and effects on refill friction stir spot welding of AA2198-T8 sheets, Journal of Materials Research and Technology 20 (2022) 857–866, https://doi.org/10.1016/j.jmrt.2022.07.092.

[81] P. Sahlot, K. Jha, G. K. Dey, A. Arora, Quantitative wear analysis of H13 steel tool during friction stir welding of Cu-0.8%Cr-0.1%Zr alloy, Wear 378–379 (2017) 82–89, https://doi.org/10.1016/j.wear.2017.02.009.

[82] Y. Wang et al., The pin tool wear identification with vibration signal of friction stir lap welding based on a new pin tool wear division model, Measurement 242 (2025) 116131, https://doi.org/10.1016/j.measurement.2024.116131.

[83] D. Das, S. Bag, S. Pal, A. Sharma, Material Defects in Friction Stir Welding through Thermo–Mechanical Simulation: Dissimilar Materials with Tool Wear Consideration, Materials 16 (2023) 301, https://doi.org/10.3390/ma16010301.

[84] P. Sahlot, A. Arora, Numerical model for prediction of tool wear and worn-out pin profile during friction stir welding, Wear 408–409 (2018) 96–107, https://doi.org/10.1016/j.wear.2018.05.007.

[85] H. Sarmadi, A. H. Kokabi, S. M. Seyed Reihani, Friction and wear performance of copper–graphite surface composites fabricated by friction stir processing (FSP), Wear 304 (2013) 1–12, https://doi.org/10.1016/j.wear.2013.04.023.

[86] M. K. Mahto, A. Kumar, S. K. Gupta, P. Kumar, M. Vashista, M. Z. Khan Yusufzai, Failure analysis of refractory tungsten carbide tool containing different cobalt percentages during friction stir cladding of copper on steel, Engineering Failure Analysis 187 (2026) 110592, https://doi.org/10.1016/j.engfailanal.2026.110592.

[87] S. Lu, B. Shang, Z. Luo, R. Wang, F. Zeng, The effect of the thermal exposure on microstructure of MP159 alloy, Journal of Materials Science 34 (1999) 5449–5456, https://doi.org/10.1023/A:1004791807509.

[88] Y. Cai, S. Xiang, Y. Tan, Insight into the Dynamic Recrystallization Behavior and Microstructure Evolution of MP159 Superalloy During Hot Deformation, Met. Mater. Int. 28 (2022) 2381–2394, https://doi.org/10.1007/s12540-021-01139-8.

[89] Cobalt-based powders for laser cladding | Höganäs. [Online]. Available: https://www.hoganas.com/en/powder-technologies/surface-coating/products/laser-cladding/co-based/ (accessed Jun. 15, 2026).

[90] S. Lu, B. Shang, Z. Luo, R. Wang, F. Zeng, The effect of the thermal exposure on microstructure of MP159 alloy, Journal of Materials Science 34 (1999) 5449–5456, https://doi.org/10.1023/A:1004791807509.

[91] Investigation on the Recrystallization Behaviour of Cold Deformed MP159 Alloy. [Online]. Available: https://www.jmst.org/EN/abstract/abstract15015.shtml (accessed Jun. 15, 2026).

[92] Effect of Interlayer Cooling Time, Constraint and Tool Path Strategy on Deformation of Large Components Made by Laser Metal Deposition with Wire. [Online]. Available: https://www.mdpi.com/2076-3417/9/23/5115 (accessed Jun. 15, 2026).

[93] E. R. Denlinger, J. C. Heigel, P. Michaleris, T. A. Palmer, Effect of inter-layer dwell time on distortion and residual stress in additive manufacturing of titanium and nickel alloys, Journal of Materials Processing Technology 215 (2015) 123–131, https://doi.org/10.1016/j.jmatprotec.2014.07.030.

[94] Microstructure Evolution and Failure Behavior of Stellite 6 Coating on Steel after Long-Time Service. [Online]. Available: https://www.mdpi.com/2079-6412/9/9/532 (accessed Jun. 15, 2026).

[95] A. Gholipour, M. Shamanian, F. Ashrafizadeh, Microstructure and wear behavior of stellite 6 cladding on 17-4 PH stainless steel, Journal of Alloys and Compounds 509 (2011) 4905–4909, https://doi.org/10.1016/j.jallcom.2010.09.216.

[96] R. Dharavathu, K. Shetty, G. Muvvala, A study on laser cladding of Stellite 6 by conventional and high-speed laser cladding process, Surface and Coatings Technology 515 (2025) 132623, https://doi.org/10.1016/j.surfcoat.2025.132623

[97] An Overview of Laser Metal Deposition for Cladding: Defect Formation Mechanisms, Defect Suppression Methods and Performance Improvements of Laser-Cladded Layers. [Online]. Available: https://www.mdpi.com/1996-1944/15/16/5522 (accessed Jun. 15, 2026).

[98] R. Halder et al., The Effect of Interlayer Delay on the Heat Accumulation, Microstructures, and Properties in Laser Hot Wire Directed Energy Deposition of Ti-6Al-4V Single-Wall, Materials 17 (2024) 3307, https://doi.org/10.3390/ma17133307.

[99] Effect of Interlayer Cooling Time, Constraint and Tool Path Strategy on Deformation of Large Components Made by Laser Metal Deposition with Wire. [Online]. Available: https://www.mdpi.com/2076-3417/9/23/5115 (accessed Jun. 15, 2026).

[100] Coaxial laser cladding of cobalt-base alloy StelliteTM 6 on gray cast iron/investigations on friction, wear versus commercial brake pad, and corrosion characteristics - Maximilian Kiehl, Adriano Scheid, Karin Graf, Benedikt Ernst, Ulrich Tetzlaff, 2023. [Online]. Available: https://journals.sagepub.com/doi/abs/10.1177/09544070221145512 (accessed Jun. 15, 2026).

[101] Effect of Ta on the microstructure and hardness of Stellite 6 coating deposited by low power pulse laser treatments - ScienceDirect. [Online]. Available: https://www.sciencedirect.com/science/article/pii/S0257897212010389 (accessed Jun. 15, 2026).

[102] X. Liu et al., Studies on high power laser cladding Stellite 6 alloy coatings: Metallurgical quality and mechanical performances, Surface and Coatings Technology 481 (2024) 130647, https://doi.org/10.1016/j.surfcoat.2024.130647.

[103] Deposition of Stellite 6 alloy on steel substrates using wire and arc additive manufacturing | The International Journal of Advanced Manufacturing Technology | Springer Nature Link. [Online]. Available: https://link.springer.com/article/10.1007/s00170-020-06116-w (accessed Jun. 15, 2026).

[104] M. Safari, M. Moradi, J. Joudaki, A. M. Babaei, Experimental investigation of laser cladding of H13 hot work steel by Stellite 6 powder, Sādhanā 47 (2022) 144, https://doi.org/10.1007/s12046-022-01909-z.

[105] H. G. Pisarski, R. E. Dolby, The Significance of Softened HAZs in High Strength Structural Steels, Weld World 47 (2003) 32–40, https://doi.org/10.1007/BF03266387.

[106] G. Payne, A. Ahmad, S. Fitzpatrick, P. Xirouchakis, W. Ion, M. Wilson, Remanufacturing H13 steel moulds and dies using laser metal deposition, in: 14th International Conference on Manufacturing Research, 2016, pp. 93–98, https://doi.org/10.3233/978-1-61499-668-2-93.[107] A. Appleby, A. Reimer, Manufacturing impact assessment for remanufacture of a forging die, International Conference on Remanufacturing 2023, Jun. 2023.

[108] D. Mellouli, N. Haddar, A. Köster, H. F. Ayedi, Hardness effect on thermal fatigue damage of hot-working tool steel, Engineering Failure Analysis 45 (2014) 85–95, https://doi.org/10.1016/j.engfailanal.2014.06.007.

[109] A Review on the Adiabatic Shear Banding Mechanism in Metals and Alloys Considering Microstructural Characteristics, Morphology and Fracture. [Online]. Available: https://www.mdpi.com/2075-4701/13/12/1988 (accessed Jun. 15, 2026).